Photothermal Effects of Pulsed Laser Irradiation of Biological Tissue

by

Andrew D. Yablon

S.M., Massachusetts Institute of Technology (1993)
S.B., Massachusetts Institute of Technology (1992)

SUBMITTED TO THE DEPARTMENT OF MECHANICAL ENGINEERING IN PARTIAL FULFILLMENT OF THE REQUIREMENTS FOR THE DEGREE OF

DOCTOR OF PHILOSOPHY

at the

MASSACHUSETTS INSTITUTE OF TECHNOLOGY

September, 1997

Signature of Author:_____
Department of Mechanical Engineering
July 22, 1997

Certified by:_____
B. B. Mikic
Professor, Department of Mechanical Engineering
Thesis Supervisor

Certified by:_____
N. S. Nishioka
Assistant Professor of Medicine, Harvard Medical School
Thesis Supervisor

Accepted by:_____
A. A. Sonin
Chairman, Departmental Committee on Graduate Students

Photothermal Effects of Pulsed Laser Irradiation of Biological Tissue

by

Andrew D. Yablon

Submitted to the Department of Mechanical Engineering on July 22, 1997 in
Partial Fulfillment of the Requirements for the Degree of Doctor of Philosophy

Abstract

The photothermal effects resulting from pulsed laser irradiation of biological tissue can be employed to extract the material properties of the target tissue as well as to study the dynamics of photothermal laser-tissue ablation. To measure such photothermal effects in a time-resolved manner, an interferometer capable of tracking the surface displacement of tissue with single nanometer spatial resolution and 4 nanosecond rise time was developed.

Using the interferometer and a theoretical model, we developed a novel spectroscopic technique, termed Interferometric Photothermal Spectroscopy (IPTS), which can estimate the effective absorption coefficient of a laser pulse in a tissue target. This new technique is important since it is epitaxial and involves minimal disturbance of the sample. Consequently it has potential use for *in vivo* measurements of effective absorption coefficients. To validate the technique, the absorption coefficient of Q-sw Er:YSGG laser radiation in pure water was measured using IPTS and the results agreed with values cited in the literature. IPTS was then employed to measure the effective absorption coefficient of 193 nm ArF excimer laser radiation to be $1.9 \pm .4 \times 10^4$ cm^{-1} for *in vitro* bovine corneal stroma.

We employed the interferometer to study pulsed laser driven heat and mass transfer. Data obtained from water samples exposed to intense Q-sw Er:YSGG laser radiation strongly suggests that at high irradiances, the rate of surface vaporization rivals and perhaps even exceeds the upper limit predicted by a free molecular flow kinetic theory model. Such high rates of interphase heat and mass transfer are expected to influence the ablation dynamics when the effective absorption depth is extremely small ($<\sim 3$ μm). High surface vaporization rates can result in the evolution of a subsurface temperature maximum where explosive nucleation and bubble growth can occur. A better understanding of these phenomena could yield predictive models for photothermal laser ablation which would be superior to empirical models in the literature in that they could be used to develop new clinical laser ablation procedures as well as to optimize current clinical laser ablation parameters.

Thesis Committee:

B. B. Mikic, Professor of Mechanical Engineering, MIT.

N. S. Nishioka, Assistant Professor of Medicine, MGH, Harvard Medical School.

J. H. Lienhard V, Professor of Mechanical Engineering, MIT.

S. Ezekiel, Professor of Electrical Engineering and of Aeronautics and Astronautics, MIT.

V. Venugopalan, Assistant Professor, Beckman Laser Institute, Univ. of California, Irvine.

Acknowledgments

Professor Mikic has served as a mentor to me over these years. This work would not have been possible without his constant advice and insight. I owe my knowledge of heat and mass transfer to his dedicated and inspired teaching.

Working on this project with Dr. Nishioka was a pleasure due to his unqualified support and his relaxed style. His expertise in medicine and biology was essential and made up for my own lack of knowledge and experience.

Vasan Venugopalan is a veteran in the field of laser-tissue interactions and provided constant guidance and perspective. His knowledge of the field is remarkable for both its depth and breadth. His work provided the foundations upon which this research stands and he has been a constant collaborator as this work has grown and matured.

A special acknowledgment to Barry Payne, my office mate for the three years it took to conduct this research. He provided me with a solid sounding board for ideas and constantly helped me solve the problems I encountered in everything from computer work to experimental design.

Professor Lienhard was always willing to meet and exchange ideas and insights. His guidance concerning interphase heat and mass transfer was critical to the completion of this work. I owe my knowledge of lasers and optics to Professor Ezekiel and his love of teaching. His class gave me the physical insight and basic knowledge I needed to do research in this field.

The Wellman Laboratories for Photomedicine proved to be a remarkably effective place for me to conduct this research, a place where doctors, engineers, and scientists can readily collaborate and learn from each other. The Wellman staff was most helpful and supportive in my research. Certain members stand out in my mind for their unusual contributions. Many thanks to Robert Webb for his advice and insight in the development of the instrumentation. In addition, I am deeply indebted to him for his skillful preparation of the glass films described in Chapter 3. Fran Rogomentich, Dom Bua, William Farinelli and Ken Greaves were a tremendous resource and helped me solve the numerous electronic, computer, and optical problems I encountered every step of the way. Shun Lee, Apostolos Doukas, Chris Lambert and Robert Redmond of the Wellman Labs displayed remarkable generosity and patience when indulging my desire to use their various experimental equipment. Many thanks to Tom Deutsch for helpful discussions and advice.

Special thanks to Jeremy Teichman for his help and patience in teaching me how to implement the numerical simulation described in Chapter 4.

Finally, my largest debt of gratitude is towards my wife and my family who continuously supported me through the course of my graduate studies and who made great personal sacrifices in helping me to produce this work.

To my wife

Table of Contents

List of Figures

List of Tables

Nomenclature

b - thickness of acoustically thin layer [m]

$\bar{c}$ - mean molecular velocity [m/s]

c_a - sonic velocity [m/s]

c_p - heat capacity [J/kgK]

D - characteristic penetration depth of radiation [m]

E - Youngs modulus of elasticity [N/m^2]

h_{fg} - vaporization energy [J/kg]

$j_{c\rightarrow v}$ - mass flux from condensed to vapor phase [molecules/m^{2}s]

$j_{v\rightarrow c}$ - mass flux from vapor to condensed phase [molecules/m^{2}s]

k - thermal conductivity [W/mK]

K_b - bulk modulus [N/m^2]

L - edge length of cube [m]

m - molecular mass [kg]

n - index of refraction [-]

n_v - number density of vapor molecules [molecules/m^3]

q_{max} - maximum interphase heat flux [W/m^2]

q'''_{laser} - volumetric heating by laser pulse [W/m^3]

$Q_{water\rightarrow saran}$ - Cumulative heat conducted from water to saran [J/m^2]

R - ideal gas constant [J/kgK]

t - time [s]

T - temperature [K]

T_0 - ambient temperature [K]

u_x, u_y, u_z - local displacements in x, y, and z directions respectively [m]

V - volume [m^3]

v_{cond} - conduction velocity [m/s]

v_{vap} - velocity of phase interface resulting from vaporization [m/s]

w - transverse laser beam diameter [m]

x - x coordinate [m]

y - y coordinate [m]

z - depth coordinate in irradiated target [m]

z_0 - depth coordinate in target before irradiation [m]

Z - acoustic impedance [kg/m^2s]

α - thermal diffusivity [m^2/s]

α_T - thermal expansion coefficient [K^{-1}]

Δz - surface displacement [m]

ε_{ij} - strain tensor [-]

ε_{zz} - normal strain in z direction [-]

ε_{recoil} - strain resulting from vaporization momentum [-]

ϕ_0 - incident laser fluence, also termed radiant exposure [J/m^2]

λ - wavelength [m]

λ_a - acoustic wavelength [m]

$\lambda_{thermal}$ - characteristic wavelength of thermal radiation [m]

μ_a - radiation absorption coefficient [1/m]

ν - Poisson's ratio [-]

ρ - density [kg/m^3]

ρ_0 - initial density of target material [kg/m^3]

σ - condensation coefficient [-]

σ_{ij} - strain tensor [N/m^2]

σ_{recoil} - stress resulting from vaporization recoil momentum [N/m^2]

Θ - temperature relative to ambient [K]

τ_p - laser pulse length [s]

Chapter 1
Introduction

1.1 Background and Motivation

This thesis is concerned with the thermal response of biological tissue to short pulsed (<1 ms) laser radiation. The therapeutic and diagnostic uses of short pulse laser irradiation of tissue is an important subset of the larger field of laser-tissue interactions. Short pulse laser systems are increasingly employed for purposes as diverse as ablation [55, 110], hyperthermia [111], optical diagnostics [31, 53, 114], drug delivery enhancement [15], and photodynamic therapy [22, 81]. In many cases, the thermal response of the tissue is a critical component of the medical procedure. The accurate measurement of the thermal transients which result from irradiation can be employed to understand the mechanisms mediating the laser-tissue interaction as well as to derive structural, optical, and thermophysical properties of the target tissue. The effects are termed photothermal since they result from the dynamic thermal field and associated phase changes within tissue that are caused by the laser pulse.

Despite extensive research, the mechanisms underlying short pulsed laser ablation of biological tissue remain unclear. For example, it is impossible to predict the minimum pulse energy required for tissue ablation (ablation threshold) for many common clinical laser systems. For certain clinical applications, such as ArF excimer laser irradiation of cornea, even the nature and spatial distribution of the pulsed laser energy deposition process remains obscure. Understanding the mechanism and the dynamics of laser-tissue ablation is essential for modeling and controlling these processes. Optimal therapeutic results depend on a proper

choice of laser parameters, which can only be determined with a proper understanding and modeling of the ablation event.

In general, the characteristics of laser-tissue ablation are determined empirically and this means that improved ablation characteristics can only be obtained by investigating all possible combinations of laser parameters. A better way would be to develop predictive models for laser-tissue ablation in order to determine which laser parameters will yield the best results for a given clinical procedure. With this knowledge efforts could be directed towards producing a laser with the desired characteristics.

Novel instrumentation is required in order to obtain precise measurements of the photothermal effects of pulsed laser ablation of tissue. Techniques such as stress wave detection [18, 56, 58, 95, 96], histology [103, 107], interferometry [3, 32, 33], and tissue mass removal assays [102, 104, 105] have been specialized for use in studying laser tissue interactions. There is an ongoing need for novel and improved techniques for monitoring photothermal laser-tissue interactions.

Finally, the photothermal effects resulting from pulsed laser ablation of tissue may be used to estimate various thermal and optical properties of tissue. These properties may not only be useful and informative in their own right, but also may be linked to the health or state of the tissue. Lasers are increasingly employed for what is termed minimally-invasive or optical diagnostics of tissue [31, 53, 114]. Advances in photonics and computation technology have made it possible to diagnose tissue pathology without traditional tissue resection biopsy and the associated time, cost, and risk.

1.2 Selected Medical Applications for Laser Irradiation of Tissue

Laser medical applications may be subdivided into two categories, *diagnostics* and *therapeutics*. Laser diagnostics provide information about the tissue or a particular laser-tissue interaction and it is worth noting that an important goal for diagnostics is to get the best

information while minimizing physiologic disruption. Laser diagnostics include fluorescence based detection of cancers [53], time and frequency domain photon migration [112, 114], pulsed photothermal radiometry (PPTR) [35, 43, 50], and optical measurements of blood oxygen saturation [40, 44, 69, 114]. Laser therapies are interventions intended to effect a positive clinical outcome. Examples of laser based therapies include photodynamic therapy [22, 81], tissue ablation [55, 110], and hyperthermia [111].

For therapeutic laser applications, the desired outcome is often determined by purely thermal or thermo-mechanical effects as opposed to photochemical reactions. An example of a thermally driven effect is the haemostasis (suppression of bleeding) resulting from thermal coagulation of blood and blood vessels during laser cutting of soft tissue. An example of a thermo-mechanically mediated therapeutic effect is the destruction of kidney stones by laser lithotripsy, whereby the thermal energy of a short laser pulse induces a cavitation bubble which shatters the stone upon collapse [75, 76]. In all of these applications, the proper choice of laser parameters is vital since these parameters modulate the thermo-mechanical effects and may lead to deleterious results such as unwanted tissue dissection or cell death [13, 108, 113]. The measurement of these thermo-mechanical transients in combination with theoretical modeling can be effectively used to identify key features of laser-tissue interactions. This approach has been shown to be successful for the study of pulsed laser ablation where the modeling of laser-induced thermo-mechanical effects has provided information regarding the mechanism and dynamics of laser ablation processes [4, 33, 95, 96].

1.2.1 Medical Laser Ablation

Laser tissue ablation is defined as the removal of tissue resulting from intense laser radiation and was one of the first medical applications considered for laser technology. It remains one of the most successful medical applications. Early on the advantages of laser tissue ablation were recognized: thermal effects resulting from laser heating could effectively coagulate blood vessels thus limiting bleeding. Under some conditions, the laser afforded the surgeon enhanced control and required no applied forces to cut tissue. Additionally, the proper choice

for laser parameters such as wavelength and pulse structure can selectively destroy certain tissues while leaving others unharmed [5].

Laser ablation can result from three distinct mechanisms: photothermal, photomechanical, and photochemical. In photothermal ablation, intense laser radiation leads to rapid tissue heating and a phase change which effects material removal. In photomechanical ablation, the tissue is heated so rapidly that the resulting dynamic stress field exceeds the ultimate tensile stress of the tissue and mechanical fracture results. In photochemical ablation, also termed ablative photodecomposition, the laser photons contain enough energy to directly destabilize and fracture the molecular bonds of the tissue. It is not always clear which of the three mechanisms are responsible for an ablation event, for example the mechanism for ArF laser ablation of cornea remains somewhat controversial [62, 88, 89]. In some situations, more than one of these mechanisms may be operative.

To understand and model the mechanisms and dynamics of laser ablation, sophisticated instrumentation for monitoring the process is required. Previous researchers have employed a wide range of techniques to analyze laser tissue ablation including mass loss measurements [102, 104, 105], high speed photography [15, 23, 34, 57, 59, 100, 106], Raman spectroscopy [27], probe beam deflection [27], radiometry [35, 43, 93, 98], stress transient detection [18, 88, 95, 96], interferometry [32, 33], and histology [103, 107]. Each of these methods have advantages and disadvantages but in general time-resolved techniques such as stress transient detection and interferometry provide much more detailed information about the ablation dynamics than other techniques such as mass loss measurements or histology.

Recent work suggests that the choice of laser wavelength and pulse duration determines which tissue constituents absorb the laser energy and this choice in turn determines the dynamics of the ablation. The tissue structural matrix is responsible for the tissue structural integrity so specifically targeting the structural matrix has been proposed as a method for minimizing the energy required for ablation and thus the resulting collateral damage [61].

Understanding and modeling laser ablation remains an important and fertile field of

research as new laser sources become available and new medical laser ablation procedures are developed. Recently, researchers have made efforts to develop predictive models for laser ablation in place of descriptive empirical models. Such predictive models are particularly useful since in the absence of experimental data, they can suggest which laser wavelength band or what laser pulse duration is most suitable for a medical ablation procedure.

1.2.2 Minimally-Invasive Diagnostics

The phrase "above all do no harm" from the Hippocratic oath captures the motivation and zeal with which physicians seek techniques for diagnosing pathologies without disturbing surrounding tissues. In recent years, a plethora of optical diagnostic techniques have been developed. The rapid diversification of optical diagnostic techniques results primarily from recent advances in photonics and computational technologies. These techniques generally exploit the ability to deliver radiation to and detect it from relatively remote locations deep inside the body such as the gut and coronary arteries, as well as from readily accessible sites such as the skin or oral cavity. For example, optical techniques can be employed to detect neoplasms, cancers, and the concentration of chemical species [31, 53].

Other minimally-invasive diagnostic techniques such as ultrasound and x-ray imaging have flourished as well in recent years, but optical techniques have certain advantages such as high bandwidth, high resolution, potential sensitivity to biochemistry, and a relative lack of side effects. Optical diagnostics may range from single point measurements to real-time three dimensional images of tissue [31]. One important issue for optical diagnostic techniques is the degree of contrast between pathological and non-pathological structures. For example, in the absence of any chemical stain, a thin slice of almost any tissue appears transparent when illuminated by visible light. Consequently it is nearly impossible to distinguish between pathological and normal tissue without a stain. However, many tissue substances have specific optical absorption and fluorescent properties which can be probed with monochromatic excitation and detection. These techniques can potentially be exploited to monitor not merely tissue structure but also its biochemical composition and physiological functions.

1.3 Photothermal Techniques For Spectroscopy and NDE

Measurement and modeling of the photothermal effects of short pulse laser irradiation can be employed to extract information about the properties of the target. Techniques such as photoacoustic spectroscopy (PAS) have been employed for many years to determine the absorption coefficient of pure substances and engineering materials [8, 77, 83, 91]. These photoacoustic techniques have also been employed to determine the optical properties of biological tissue samples with modest success [1, 11, 84, 85]. More ambitious efforts have been made to use the photothermal effects resulting from pulsed or modulated laser irradiation as a form of non-destructive evaluation (NDE) and even imaging [36, 52, 54, 77, 78].

Since most tissues are both heterogeneous and anisotropic their properties are difficult to model and are usually determined empirically. Further complications arise because the tissue properties are often strong functions of tissue hydration, coagulation, and local energy density, some or all of which may change during irradiation [12, 19, 20, 62, 64-66, 89, 101]. For example, the absorption coefficient of 193 nm radiation in cornea was found to depend strongly on hydration state and the method of sample preparation [19, 20, 62, 64, 68].

NDE techniques developed for engineering have a particular resonance with efforts in the medical community to develop new minimally-invasive diagnostic techniques to avoid resorting to traditional biopsy and subsequent histological and biochemical analysis. The photothermal effects resulting from short laser pulses may have the potential to form the basis for new clinical minimally-invasive diagnostic techniques. Pulsed photothermal radiometry (PPTR) is a specific minimally-invasive diagnostic technique which measures the temporal evolution of the radiative emission from the surface of a tissue sample in response to a short pulse of sub-ablative laser radiation. This measurement is then used to compute the thermal field below the surface and can be used to obtain spectroscopic or structural information [42, 43, 90, 98]. This technique has been applied to biological systems in an effort to detect the

location and size of subsurface blood vessels in skin [35, 50].

In general, to extract information about a tissue target from its photothermal response to pulsed laser irradiation, it is necessary to model the physics governing the process. When the goal of the measurement is a tissue material property, the equations governing the photothermal response cannot always be inverted directly to yield this value and hence sophisticated parameter estimation techniques are necessary [7, 30, 35, 60]. For example, PPTR is often times concerned with an inverse heat transfer problem. Given the temporal evolution of the temperature field on the boundary, the goal is to determine the initial temperature field in the interior.

1.4 Research Objectives

Based on the recent success of interferometric techniques to measure the surface displacement of laser irradiated tissue [3, 4, 32, 33], interferometry was chosen to measure the tissue photothermal response. Given the capability of this instrumentation and the state of knowledge in the field of laser tissue interactions, the specific research objectives for this work were organized as follows:

I. Improve interferometric instrumentation for the measurement of surface displacement resulting from short pulse laser irradiation

II. Develop a novel technique for estimating the effective absorption coefficient of a short laser pulse in tissue

III. Employ this technique to estimate the effective absorption depth of 193 nm laser radiation in cornea

IV. Study the effects of high rate interphase heat and mass transfer on laser ablation

In light of these goals, the structure of this thesis is as follows. The interferometric instrumentation is presented and discussed in Chapter 2. In Chapter 3, suitable models for the surface displacement of laser irradiated tissues are derived. Based on this modeling, a novel minimally-invasive diagnostic technique termed Interferometric Photothermal Spectroscopy

(IPTS) is developed. The results of a verification experiment are presented along with the results of a pilot study illustrating the power of this new technique. In Chapter 4, the influence of interphase heat and mass transfer on the thermo-mechanical response of water and tissue to short pulse laser irradiation is discussed along with implications for tissue ablation. Finally, in Chapter 5 conclusions drawn from this work and future directions for related research are presented and discussed.

Chapter 2
Interferometric Measurement of Surface Displacement

2.1 Introduction

Interferometry is an attractive technique for time-resolved measurements of photothermal and photomechanical effects resulting from pulsed laser irradiation of biological tissue since it has high sensitivity (~nm) and bandwidth (~100 MHz). In addition, an interferometer is inherently minimally-invasive since it measures time resolved displacements by analyzing the phase of reflected light. Interferometry has been extensively employed for sensitive displacement measurements for many decades and has already been employed by Albagli and co-workers to study medical laser ablation [3, 4, 32, 33].

Competing techniques for obtaining time-resolved information about the effects of pulsed laser irradiation include stress transient detection, transmission or reflection spectroscopy, fluorescence spectroscopy, Raman spectroscopy, and PPTR (pulsed photothermal radiometry). Only interferometry and stress transient detection directly measure the thermo-mechanical response of tissue to pulsed laser irradiation. For some laser-tissue interactions, as in the case of ArF excimer laser irradiation of cornea described later in this thesis, the absorption depth of the laser is so small that the resulting thermoelastic stress waves are too weak to be detected with existing stress transducers. In addition, both transmission spectroscopy and stress transient detection generally require thin tissue specimens *in vitro*. Fluorescence spectroscopy may require the use of a fluorescing dye, and in general such

techniques may not provide useful information about the thermal state of the tissue. The tissue volume heated by the pumping laser is often thinner than the length scale of the wavelength of its peak radiative emission (generally 7-10 μm), consequently the radiative emission is suppressed and PPTR cannot be employed. In some cases, interferometry may be the only viable option for monitoring the thermo-mechanical tissue response.

Interferometry has been employed to study the dynamics of mechanically confined laser-tissue ablation [3, 32]. The researchers in these pioneering studies demonstrated that interferometric measurements of tissue surface motion can be combined with suitable models to obtain useful information about the mechanical and optical properties of the tissue. In theory, a clinical interferometer could be built into an endoscope or even applied to the surface of exposed skin. Such a device could provide useful diagnostic information about the health of the tissue target when the target is exposed to a short sub-ablative laser pulse. In Chapter 3, interferometry will be employed to estimate the effective absorption coefficient of 193 nm laser radiation in cornea, an important parameter for understanding and modeling the clinical procedure known as photorefractive keratectomy (PRK). In Chapter 4, interferometry will be employed to explore the dynamics and implications of high rate interphase heat and mass transfer near the ablation threshold.

2.2 Time-Resolved Techniques for Monitoring the Thermo-Mechanical Effects of Pulsed Laser Irradiation

At this time, there are only two techniques for directly monitoring the thermo-mechanical effects of pulsed laser irradiation: stress transient detection and surface displacement measurement. The two techniques are relatively complementary as will be described in the sections below.

2.2.1 Stress Transient Detection

Stress transients result from a laser tissue interaction due to rapid heating of the tissue,

the recoil momentum resulting from tissue removal, or from plasma formation or other violent phase change phenomena [15, 83]. In general, the propagation of such stress transients is governed by wave mechanics and thus they are modified during propagation by diffraction, dispersion, and attenuation. Due to the nature of stress wave generation and propagation in tissue, it is very difficult to measure the stress transients induced in tissue without sectioning it; stress waves cannot readily be detected epitaxially. Several techniques for time-resolved detection of stress wave are available including hydrophones or piezoelectric devices. Piezoelectric devices are in general more sensitive and have a higher bandwidth than hydrophones. Accordingly they have been more successful for the quantitative study of laser induced stress transients.

In previous studies, a 9 μm polyvinylidene fluoride (PVDF) foil has been employed to characterize the dynamics of laser tissue ablation [18, 57, 95, 96]. This type of transducer has the advantages of high bandwidth (~70 MHz), planar stress wave detection, and, sensitivity (noise floor of ~10^5 Pa). Additionally, it may be readily coupled to the rear side of thin tissue specimens so that one dimensional stress transients may be clearly resolved.

2.2.2 Surface Displacement Measurement

Surface displacement measurement represents the complement to stress wave detection in a fundamental sense since stress transducers detect the state of stress while surface displacement instruments detect the state of strain (or displacement) in the sample. In theory, if the relationship between the stress, strain, and temperature (often termed the equation of state) of the irradiated target were understood, and the temperature field in the tissue was known, then a measurement of the state of stress could be used to determine the state of strain and *vice versa.*

Optical techniques are ideal for measuring surface displacement and interferometry provides the highest bandwidth and sensitivity available at this time. There are several excellent references which discuss the basic operating principles of interferometry consequently we will not discuss them in this thesis [9, 24, 28, 29]. Optical interferometric surface displacement detection has several advantages over PVDF stress wave detection as tabulated in Table 2.1.

Stress transducers integrate the signal over a large area to provide a single value for stress as a function of time, while interferometer probe beams can be focused down to small spot sizes (~15 μm) that monitor the motion of only a small surface region. Consequently, several different interferometer position traces may be combined to create a three-dimensional contour of the response of a target surface exposed to pulsed laser irradiation. In general, stress transducer rise times are limited to about 5 ns. In contrast to stress transducers, the interferometer rise time is limited only by the quality of the optical signal and the response time of the detection equipment so that single-nanosecond rise times are feasible.

The signal calibration curve of a stress transducer which relates stress to voltage is difficult to determine precisely and may vary during the course of experiments [94]. In contrast, the calibration between the phase in an interferometer and the relative path length difference between its two arms is generally known to a very high precision. Acoustic reflections limit the duration of a stress transducer measurement while interferometry suffers from no such impediment. However, interferometer probe beams may be blocked by ejected material during an ablative event, and changes in the tissue surface may compromise signal quality. Since stress transducers are most effective when used to monitor transients traversing thin samples, it is difficult to employ them *in vivo* while it is relatively easy to use an interferometer for *in vivo* monitoring.

Interferometer	**PVDF Stress Transducer**
• Measures strain (actually displacement) at front surface of target	• Measures stress at rear surface of target
• Monitors motion of single ~15 μm diameter spot	• Integrates stress measurement over entire surface area of transducer
• Negligible calibration uncertainty	• Suffers from calibration uncertainty
• ~4 ns rise time (potential for <500 ps)	• ~5 ns rise time
• Difficult to employ in vicinity of material ejection	• Readily employed to monitor ablative events
• Easy to employ *in vivo*	• Difficult to employ *in vivo*

Table 2.1: Comparison between interferometer and PVDF stress transducer

2.3 Interferometer Design

The experimental configuration employed for this thesis is shown in Figure 2.1 and consists of a tissue target, a modified Mach-Zehnder interferometer, and a pump laser source. A 2 mW polarized HeNe (helium-neon) laser beam (Melles Griot, Irvine, CA) with a wavelength of 632.8 nm is used as the probe beam. A high-speed ferroelectric liquid crystal shutter (Displaytech Inc., Boulder CO) with a 50 μs rise time was used in cases where significant temperature changes in the target might result from the focused HeNe probe beam (shown in Figure 2.1). A solution to the heat conduction equation showed that the shutter rise time is sufficiently fast to render any heating due to the HeNe probe beam negligible [45]* . For most of the data presented in the thesis, the effective absorption coefficient of the HeNe radiation was so low that heating was negligible even without the shutter system.

An acousto-optical modulator (IntraAction Corp., Bellwood, IL) is used to deflect a portion of the beam and impart a 110 MHz frequency shift to that portion. The undeflected and unshifted portion of the beam travels unimpeded through the polarized beamsplitter cube due to its polarization state and is confocally imaged onto the target surface by a 125 mm focal length lens (focused spot diameter ~100 μm). This portion of the beam could also be termed the sample arm since it interacts with the sample. The index of refraction mismatch between air and the water based target provide for sufficient reflected signal. When necessary, the beam is expanded before focusing by a 10x beam expander (Melles Griot). The beam expander increased the numerical aperture in order to capture more signal reflected from diffuse surfaces (such as porcine dermis). It also results in a smaller focused spot diameter (~15 μm) on the sample which can be useful when the irradiated zone of the target is small.

* The reader should note the presence of a typo in Eq. (32) of reference [45]. An extra number "2" appears under the radical sign in the denominator of the 2nd term in the equation.

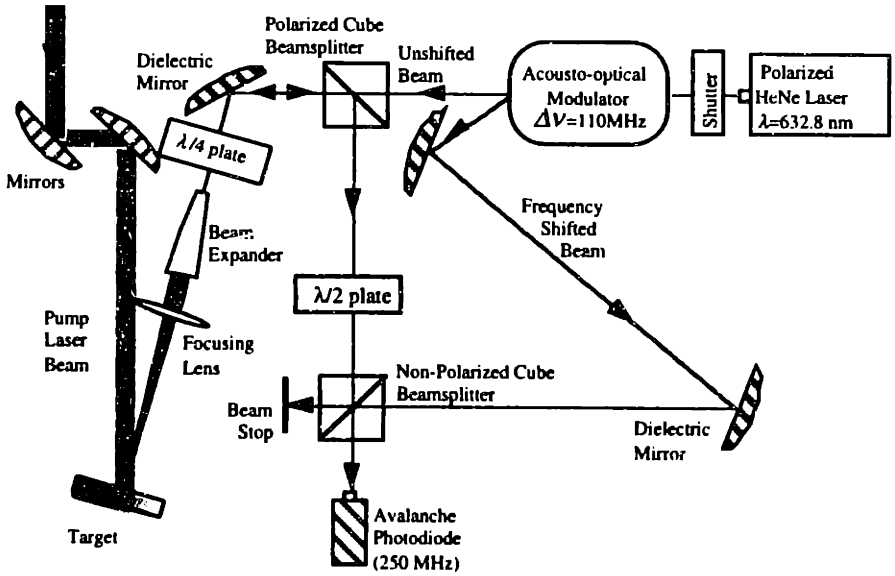

Figure 2.1: Interferometer schematic

The unshifted beam passes through the quarter wave plate twice; once on its way to the target surface and again on its way back from the target surface. This rotates the polarization of the beam by 90 degrees such that the beam is reflected rather than transmitted by the polarized beamsplitter cube on the second encounter. After reflection by the cube, the unshifted beam passes through a half wave plate that matches its polarization state with that of the frequency shifted beam. The unshifted beam may also be termed the reference arm since the interferometer essentially compares the phase of the sample arm to the phase of the reference arm. The sample arm optical path length is aligned to be nearly equal to the reference arm optical path in order to preserve temporal coherence between the laser beams in each arm. The two beams are mixed together at a non-polarized beamsplitter cube and the resulting signal is measured by a high speed (250 MHz) avalanche photodiode (EG&G, Quebec, Canada).

When the target remains stationary the APD detects interference fringes at the AOM modulation frequency of 110 MHz (Figure 2.2). Due to the Doppler effect, any target surface velocity in the direction of the probe beam results in a corresponding perturbation of the frequency of the fringes. In other words, the instantaneous position of the target surface is determined from the amount of phase shift incurred at the photodiode. The polarity of the phase

shift depends on the direction of the target displacement. Thus the target displacement can be determined by detecting the phase of the photodiode signal.

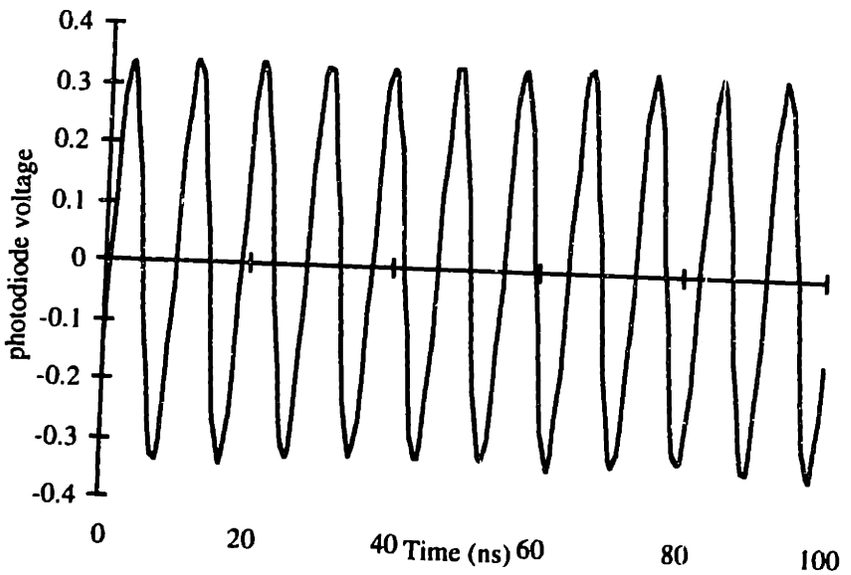

Figure 2.2: Interference fringes detected by avalanche photodiode

The signal measured by the photodiode is digitally sampled by a 500 MHz bandwidth oscilloscope (Tektronix, Wilsonville, OR) and processed on a personal computer (Apple Computer, Cupertino, CA). Refer to Figure 2.3 for a schematic of the algorithm used to create the displacement trace. The electrical signal driving the AOM is simultaneously acquired by the oscilloscope and serves as a phase reference signal. A program written in the LabVIEW environment (National Instruments, Austin, TX) is used to implement the algorithm depicted in Figure 2.3. To suppress noise, a band bass filter centered on the 110 MHz carrier is applied to the raw APD signal such that frequencies between 30 and 190 MHz are passed unaltered while frequencies outside this band are removed. The Hilbert transform is applied to both the filtered APD signal and the AOM driving signal to detect the phase of both as a function of time. The phase difference between the two signals is converted into displacement information. The constant of proportionality between the phase difference and the surface displacement is 50.36 nm/radian since a surface displacement of one wavelength (632.8 nm) corresponds to a

optical path length difference of two wavelengths (4π radians).

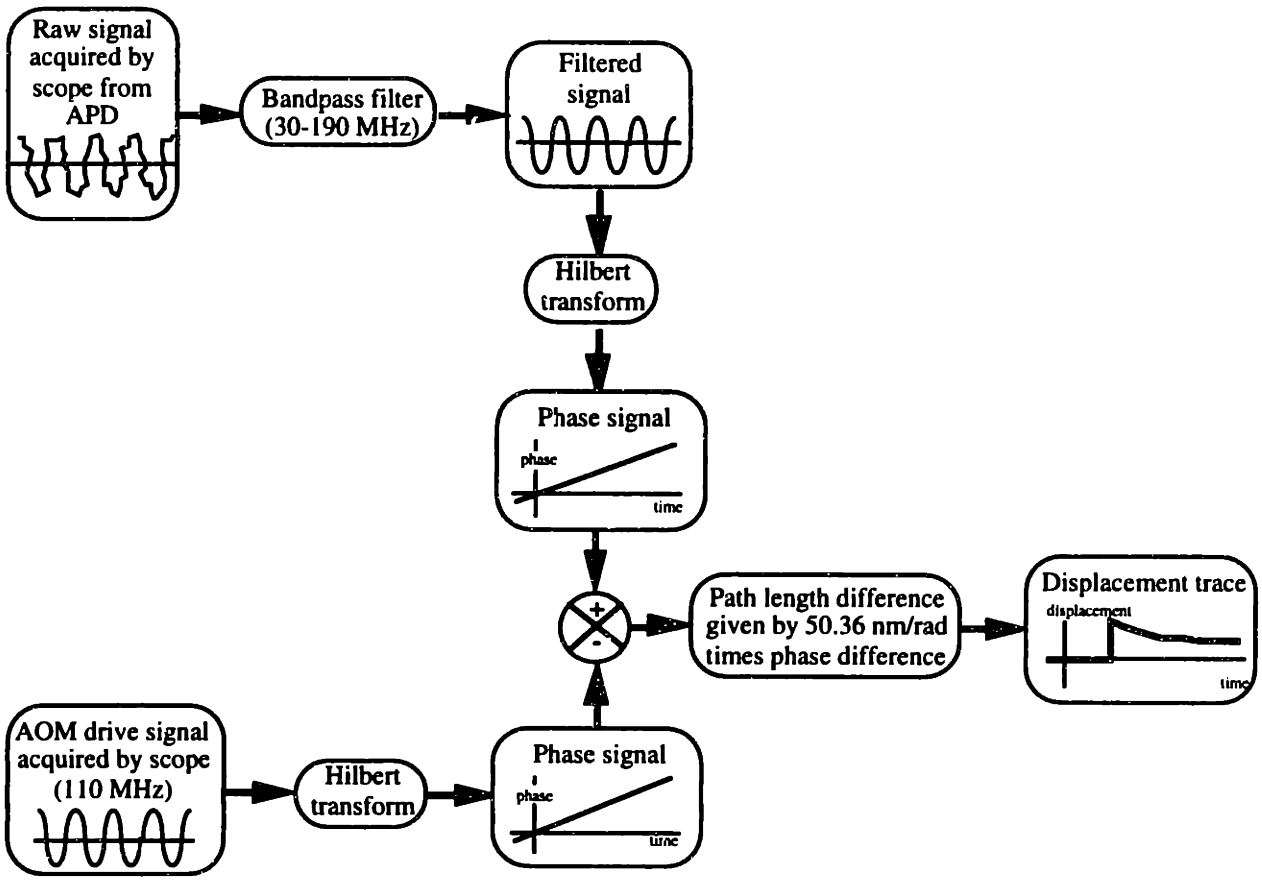

Figure 2.3: Schematic of algorithm employed to generate surface displacement traces

2.4 Interferometer Capabilities

Due to the high numerical aperture confocal imaging design, this interferometer can be used to monitor the motion of a diffuse surface in contrast to the instrument documented by Albagli et al [3, 79] which is restricted to specular tissue surfaces. However, diffuse surfaces return less of the incident HeNe beam into the collection optics than specularly reflecting targets, thus limiting spatial accuracy to several nanometers. The probe spot size employed here is several times smaller than Albagli et al (~15 μm versus ~50 μm) [3, 79] leading to a more localized measurement of surface displacement. This permits an assessment of the two-

dimensional surface displacement field with higher lateral resolution.

A sample displacement trace obtained for Q-switched (Q-sw) Er:YSGG laser irradiation of porcine dermis is presented in Figure 2.4. In general porcine dermis is not optically smooth and thus is a diffuse reflecting surface. Figure 2.4 clearly shows that nm scale accuracy is achievable with this interferometer system on such diffuse surfaces.

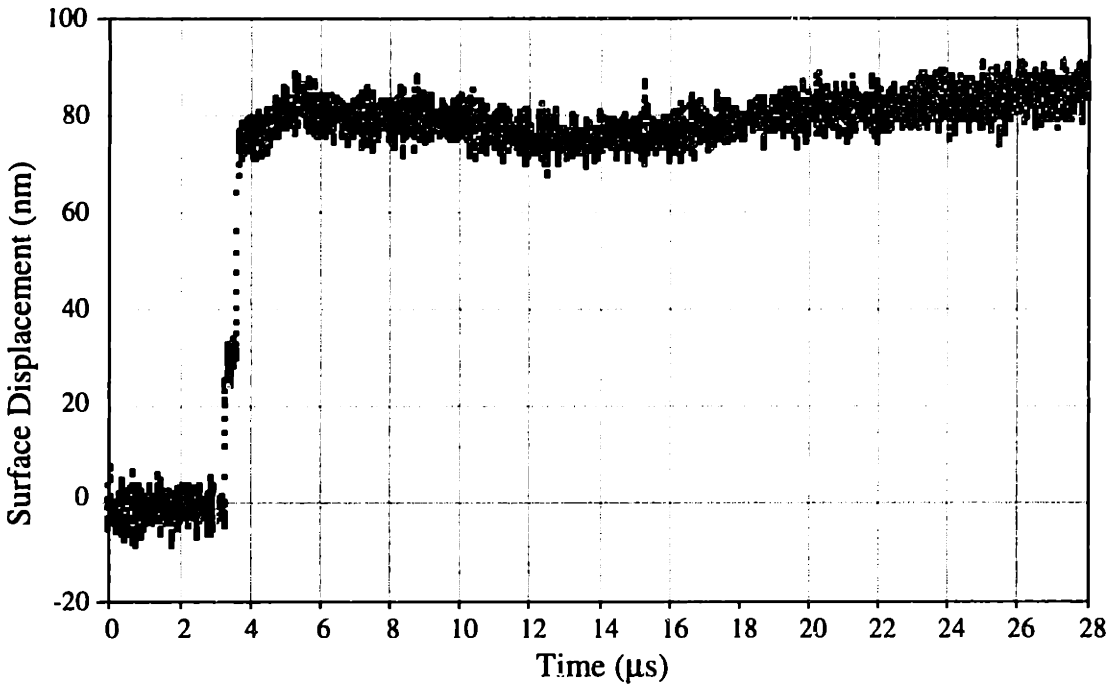

Figure 2.4: Surface displacement of porcine dermis exposed to 2.79 μm Q-sw Er:YSGG laser radiation

There is a trade off between the rise time of the instrument and the amount of noise present in the signal. The best compromise was found to occur when using a 30-190 MHz band pass filter on the raw APD signal which resulted in a 4 ns rise time. Even in the absence of any noise, the shortest possible rise time for the system described here is about 3 ns and is limited by the modulation frequency of the AOM (in this case 110 MHz). Higher modulation frequencies and higher detector bandwidths can theoretically yield shorter rise times (down to a single nanosecond) than those achieved by the system documented here.

For specularly reflecting targets, the best accuracy achieved to date with our interferometer is ±0.9 nm. This compares favorably with a theoretical accuracy of ±0.32 nm

which is limited by the analog to digital converter (A/D) in the oscilloscope. The nominal resolution of the A/D converter in the scope is 8 bits (256 levels of signal) but at high bandwidths the effective number of useful digitizer bits falls to about 7 and moreover the full digitizer scale is not usually employed. Thus in some cases, as few as 64 levels of signal are available for digitizing the raw signal output of the APD. This discretization of the analog APD signal results in a displacement uncertainty of ±0.32 nm. Consequently, even if all sources of noise and non-linearity were eliminated from the interferometer system, the accuracy could only improve by a factor of 3. Obviously, more sophisticated oscilloscopes can achieve higher resolution in their A/D converters at high bandwidths, and can thus yield even better precision.

As noted earlier, one significant disadvantage of interferometry is that material removed during ablation may interfere with the interferometer signal. If material is removed in very small fragments, for example through evaporation, the HeNe probe beam may successfully track surface motion. However, explosive ablation events, such as those occurring during pulsed CO_2 irradiation of tissue, will generally produce larger fragments of debris that will scatter the HeNe probe beam. To some extent, the size of ejected material fragments and their time of ejection could be inferred from their effect upon the interferometer probe beam.

One limitation of traditional interferometry is that only surface displacement of the tissue may be tracked. Our interferometer effectively incorporates a confocal microscope to image the target surface. This suggests that with some modifications, imaging an optical scatterer below the tissue surface should be possible. Thus the motion of an interior point as well as a point on the surface can be tracked. The signal would be weaker in such a case and spatial resolution is expected to suffer.

Figure 2.5 demonstrates the capability of the interferometer to function as an imaging tool. Several displacement traces were acquired at different positions on the surface of a gelatin sample during repeated Q-sw Er:YSGG laser pulses. The traces obtained for the different pulses were combined to yield a three dimensional surface map of the gelatin surface motion. Note that the individual displacement traces were obtained on a radial line and since the laser

pulse was known to be radially symmetric, the surface displacement was also assumed to be radially symmetric, so the plot was generated by spinning the position data about the laser's axis of symmetry. There is no reason why a map of the surface displacement could not be generated from a Cartesian grid of large number of traces.

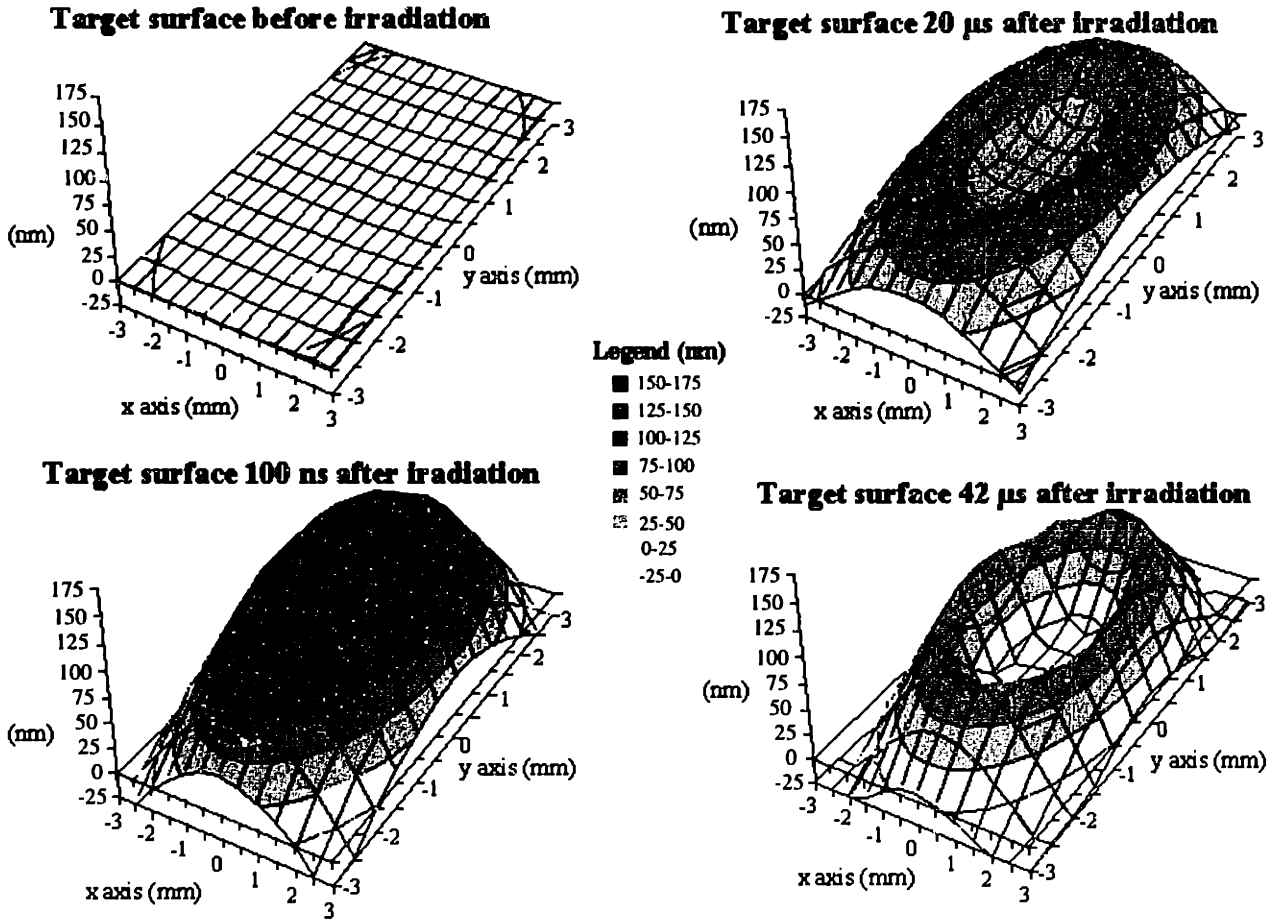

Figure 2.5: Three-dimensional time-resolved surface contours of a gelatin target exposed to a single near-threshold pulse from a Q-sw Er:YSGG laser at 2.79 μm

2.5 Conclusions and Future Directions in Instrumentation

Interferometry is an excellent technique for directly obtaining time-resolved information about the thermo-mechanical effects of pulsed laser irradiation of biological tissue. For this

thesis, a modified Mach-Zehnder interferometer capable of nanometer spatial accuracy and nanosecond temporal resolution was designed and built to study the photothermal effects of pulsed laser irradiation of biological tissue. This interferometer has the advantages of extremely high bandwidth, the ability to monitor both diffuse and specular surfaces, and epitaxial design.

Advances in photonics technology will permit even more accurate and higher bandwidth surface displacement measurement systems. It appears, however, that in many cases, the bandwidth and accuracy of the instrumentation is not the primary impediment towards a better understanding of laser irradiation of biological tissue. Rather, the interpretation of the displacement traces and suitable models for the tissue's response to pulsed laser irradiation represent the most important frontiers of research.

In the next chapter, we will describe a new technique for extracting useful information about the optical properties of biological tissue which employs this interferometer system. In theory, the interferometer system presented here could be implemented in optical fibers and passed through an endoscope or laparoscope in order to make similar measurements *in vivo* in a minimally-invasive manner. Future studies may show that the research tool presented here has a role as a clinical diagnostic tool.

Chapter 3
Interferometric Photothermal Spectroscopy (IPTS)

3.1 Introduction

In this chapter we demonstrate how the interferometer instrumentation described in Chapter 2 may be used in conjunction with an analytical model to estimate the absorption coefficient μ_a of a biological sample in a minimally-invasive manner. This technique is termed IPTS for Interferometric Photothermal Spectroscopy since it employs the interferometer to measure the surface displacement of a sample heated by a pump laser pulse (distinct from the interferometer probe laser). This technique is not meant to replace traditional techniques for measuring μ_a such as transmission spectroscopy, but rather to complement it and to permit measurements of μ_a that might otherwise be impossible.

Since the interferometer tracks the motion of a surface in an epitaxial manner, accessing the surface from one side only, the method may be readily employed on living tissue. There is no reason why the interferometer cannot be implemented using an optical fiber passed through an endoscope or laparoscope to make measurements of μ_a deep inside a living patient. Such measurements could be of diagnostic value as they could conceivably gauge the physiologic state of a tissue when probed at several wavelengths. Specific examples of tissue characteristics that could be related to a measurement of μ_a at a specific wavelength include the blood oxygen saturation or the concentration of a photoactive agent employed for PDT (photodynamic therapy).

IPTS may also prove to be useful for NDE (non-destructive evaluation) of thin films or laminates. The optical properties of thin film semiconductor coatings may be readily assessed with this technique. Alternatively, if the effective absorption coefficient of the material is well known, the same equipment and modeling employed for IPTS can be used to obtain the thermophysical properties of the material.

To describe the IPTS technique, it is useful to explain the meaning of thermal and mechanical energy confinement for laser irradiation of tissue. The laser irradiation is assumed to be one dimensional which means that the transverse dimension of the laser beam is much larger than the effective absorption depth. A laser pulse is termed thermally confined if the thermal energy deposited by the laser irradiation does not have time to diffuse away during the laser pulse. This is true when:

$$D >> \sqrt{\alpha \tau_p} \tag{3.1}$$

where D is the characteristic penetration depth of the laser heating, α is the thermal diffusivity of the irradiated material, and τ_p is the laser pulse duration. Note that D is the inverse of μ_a (so $D=1/\mu_a$). Both terms are employed to characterize the absorption behavior of a laser pulse in this work since the physical meaning of an equation can often be made more transparent by employing one form versus the other. In the case that scattering is not negligible relative to absorption, one can define an effective absorption coefficient (and an effective penetration depth) which incorporate the effects of scattering [10]. Since the IPTS technique relies upon absorption of the laser radiation, it measures these effective quantities.

An analogous situation exists for the mechanical energy resulting from the laser pulse. A laser pulse is termed mechanically confined if the mechanical energy manifested in the thermal stress field created by the laser irradiation does not have time to equilibrate during the laser pulse. This situation has also been termed *inertial confinement* in the literature because another way of describing it is that the inertia of the irradiated tissue prevents it from thermally expanding on the timescale of the laser pulse. Mathematically, a laser pulse is inertially confined when the following relation holds:

$$D >> c_a \tau_p \tag{3.2}$$

where c_1 is the acoustic wave velocity in the irradiated material. In tissue the acoustic wave velocity is larger than the velocity of thermal energy so that if a laser pulse is mechanically confined it is also thermally confined.

The thermal diffusion behavior of the irradiated target can be used to estimate μ_a by performing IPTS. To perform IPTS, a tissue target, a pump laser at the wavelength of interest, and an interferometer system like the one presented in the previous chapter is required. The pump laser pulse energy is required to be thermally confined but it may or may not be mechanically confined. The laser pulse will impart thermal energy to the tissue which will experience a degree of thermal expansion such that the tissue surface will move upwards. Subsequent thermal diffusion below the surface will lead to further surface motion provided that either the density of the material is non-linear with temperature or a certain amount of energy is permitted to escape through the target surface (which can occur if a transparent conducting material is placed above the target). This surface displacement due to thermal diffusion can be used to obtain information about D and hence μ_a. The IPTS procedure is depicted in Figure 3.1.

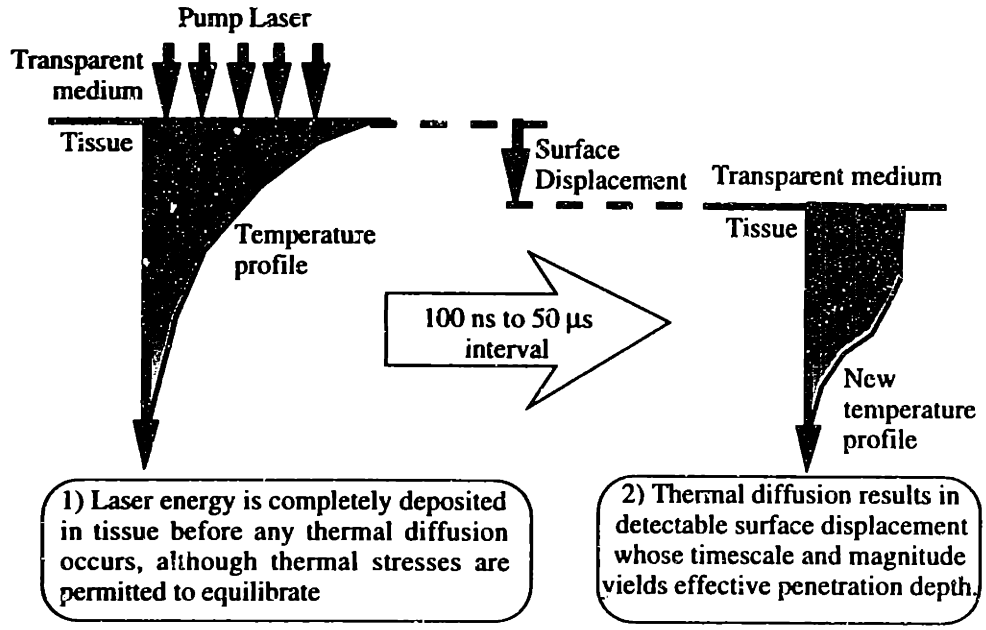

Figure 3.1: Schematic of IPTS

In practice, the range over which D can be measured by IPTS on a tissue target is limited. IPTS will only be effective when D>~100nm since for smaller penetration depths, the thermal relaxation is too weak to track (<1 nm). Moreover, as the heated volume gets thinner and thinner, Fourier's law ceases to be valid and microscale heat transfer must be considered. IPTS will only be effective for D<~10 μm, since for larger penetration depths, the thermal relaxation requires so much time that ambient acoustic surface waves on the sample will corrupt the signal.

Interferometric Photomechanical Spectroscopy (IPMS) is an analogous technique whereby an interferometer is used to measure the surface displacement of a target irradiated by a mechanically confined laser pulse. In this situation, the initial surface motion in response to the irradiation represents the equilibration of the thermal stresses. The timescale of this surface motion is governed by the acoustic wave velocity c_a, and the depth of penetration of the heating laser pulse D. A schematic diagram of IPMS is depicted in Figure 3.2. This method for deducing D and hence μ_a was first noted by Albagli and co-workers [2, 4, 33] although it was not termed IPMS, nor was it employed to measure an unknown μ_a.

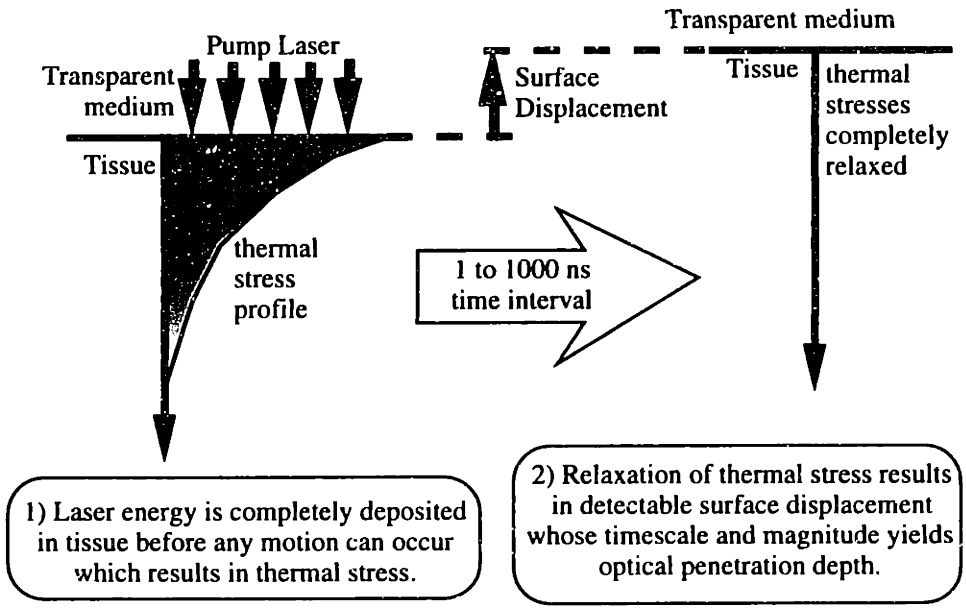

Figure 3.2: Schematic of IPMS

The range of D for which the IPMS technique can be used with a tissue target is about 10 μm to 10 mm. Since most tissues are primarily water and have similar acoustic wave velocities (~1500 m/s) and also because the rise time of an interferometer will in general be larger than a nanosecond, it is difficult to use IPMS to measure D for D<~10μm. Moreover, ambient acoustic surface waves on the target tissue surface will corrupt the interferometer signal when D is large enough to require a long duration interferometer trace. For this reason, 10 mm is viewed as a practical upper limit on D for IPMS.

The two techniques are rather complementary to each other in terms of when they are applicable as demonstrated in the parameter map of Figure 3.3 where the combinations of τ_p and D suitable for IPTS and IPMS are indicated. The decision of whether to perform IPTS or IPMS depends on the laser pulse parameters and the tissue properties. In addition, the effect of the pumping laser pulse on the tissue may be important. In some situations, IPTS may require enough thermal energy to thermally damage the tissue. In other situations, IPMS may cause damaging acoustic waves in the tissue. These issues must be carefully considered when employing these interferometric spectroscopic techniques.

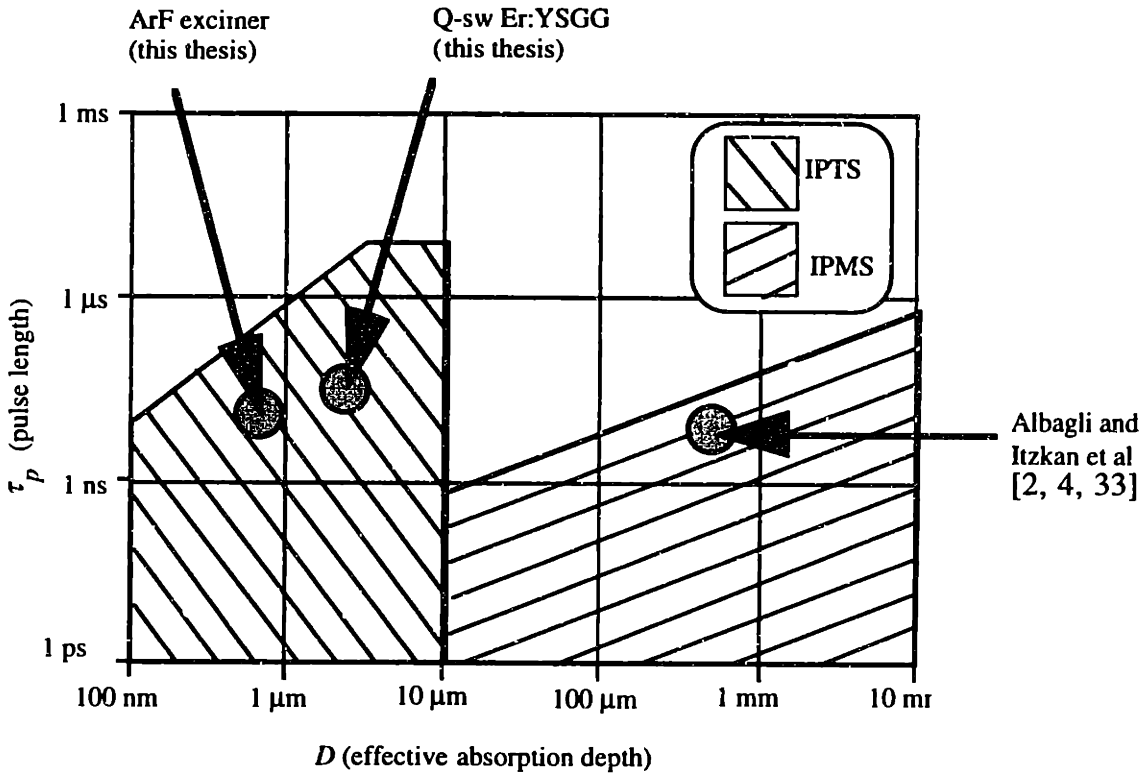

Figure 3.3: Parameter map illustrating the two regimes for IPTS and IPMS and loci of selected applications

In this thesis we will restrict our attention to a derivation and a demonstration of the IPTS technique on tissue phantoms and *in vitro* tissue samples. First we will present a formal derivation of the model employed to estimate μ_a from the interferometer displacement trace. Following this, the validity and effectiveness of the IPTS technique will be evaluated for a well controlled test situation: a sample of pure water, acting as a tissue phantom. Armed with a verification of the technique, IPTS will be used to estimate μ_a for 193 nm laser irradiation of bovine cornea. The effective absorption depth of 193 nm radiation is important for the understanding the dynamics of 193 nm cornea ablation which occurs during laser photorefractive keratectomy (PRK). PRK is a widely performed clinical procedure for surgical eyesight correction. In addition, it has proven to be very difficult to measure this absorption behavior by conventional means such as transmission spectroscopy so widely disparate values for μ_a have been quoted in the literature [19, 20, 62, 64, 68, 88, 89].

3.2 Modeling

In this section, a derivation of the thermal model employed for μ_a estimation will be presented. We shall begin with a derivation of the temperature field in the irradiated sample. Following this will be a discussion of how the thermal field influences the target surface displacement.

3.2.1 The Thermal Field

The target material (i.e. tissue) is termed material 1 and is modeled as a semi-infinite body with the coordinate z_0 as indicated in Figure 3.4. Coupled to it is another semi-infinite body (i.e. air, saran, or glass) termed material 2, largely transparent to the incident laser radiation.

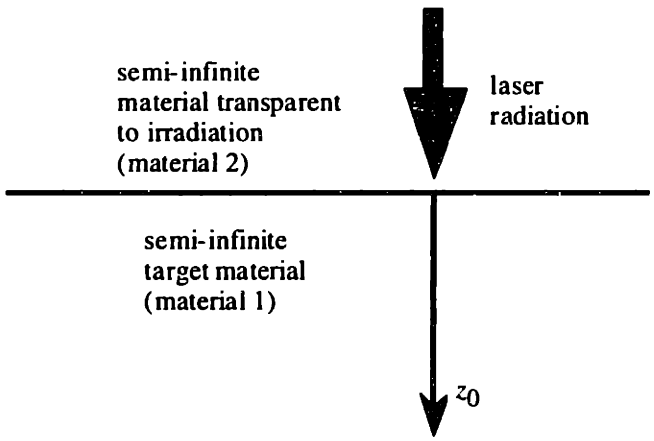

Figure 3.4: Diagram of geometry for derivation of thermal model

Initially the temperature and density of the target material are constant and defined as T_0 and ρ_0 respectively. A laser pulse of short duration heats the target material. For linear absorption, this heating profile is exponentially decaying in z_0 with a decay constant of D in length units or μ_a in inverse length units. The heating will be one dimensional (purely a function of z_0) providing $D<<w$ where w is the characteristic transverse width of the heating laser. Due to the

energy imparted by the laser pulse, the temperature field assumes a spatial and temporal dependence, denoted by $T(z_0,t)$. At this time, we ignore any energy absorption and resulting expansion in the upper semi-infinite body. Note that because the energy is fundamentally deposited on a mass basis rather than spatial basis, it is appropriate to use the original coordinate z_0 as the independent variable to describe T despite any dilatations of the target material that may have occurred.

In Appendix A we derive the following expression for the net thermal expansion of the target material assuming the thermal stresses have equilibrated, material 1 is incompressible (ν=0.5), and all of the expansion occurs in the z_0 direction due to the one dimensional heating:

$$\Delta z(t) = \int_0^{\infty} \left(\frac{\rho_0}{\rho\left[T(z_0,t)\right]} - 1 \right) dz_0 \tag{3.3}$$

where $\Delta z(t)$ is the net thermal expansion of the target material. Note that we have not established precisely where the net expansion occurs, for it may *not* be manifested as a displacement of the interface between the two materials. We shall address this issue below.

The temperature dependence of ρ is in general not known for tissue but is well characterized for water, the main constituent of soft tissue. In many cases, the water content of soft tissue is high enough that the thermophysical properties of pure water may be a sufficient approximation to those of tissue. Eq. (3.4) is a very accurate representation of the temperature dependence of the density of liquid water adapted from [109] where ρ_{water} is given in kg/m^3 and T is assumed to be in °C. It is valid for water from 0° C to 150° C at 1 atmosphere of pressure (between 100° C and 150° C the water is in a metastable state).

$$\rho_{water}(T) = \frac{999.8 + 16.95T - 7.987 \times 10^{-3}T^2 - 46.17 \times 10^{-6}T^3 + 105.6 \times 10^{-9}T^4 - 280.5 \times 10^{-12}T^5}{1 + 16.88 \times 10^{-3}T} \tag{3.4}$$

To evaluate Eq. (3.3) it is necessary to determine the temperature field as a function of

time and space in the heated target, $T(z_0,t)$. The temperature field in both semi-infinite bodies is governed by the heat conduction equation. Other energy transport modes such as convection and radiation are assumed to be negligible. Convection may be ignored in this model due to the very short timescales (<10μs), the very small length scale for D (<10μm), and the symmetry of the problem. Moreover, the structural matrix of tissue is likely to suppress any bulk flow. Radiation may be ignored since we assume that the spatial scale of the heating is less than the thermal emission wavelength ($D<<\lambda_{thermal}$) and so the heated target is in the "thin optical limit" where thermal emission is surpressed [86].

Material 1 has a temperature field T_1 and is assumed to have a constant thermal conductivity k_1 and a constant thermal diffusivity α_1. Likewise, material 2 has a temperature field T_2 and is assumed to have constant thermal conductivity k_2 and thermal diffusivity α_2. No heat source is assumed for this solution; rather the laser irradiation is modeled as an initial temperature distribution in the lower target material. This will yield a valid solution for $t>\tau_p$ providing the laser energy is thermally confined, i.e. $D<<\sqrt{\alpha_1 \tau_p}$, such that negligible conduction occurs during the laser pulse. The coordinate z_0 will now be denoted by z which reflects the fact that although there has been a dilatation of material 1, we assume that it does not significantly affect the evolution of the thermal field.

The problem may be formally posed in terms of the governing equations and their associated boundary conditions. To simplify the derivation, let θ be the temperature with respect to the ambient temperature T_0 so that $T=\theta+T_0$. Given the one dimensional nature of the problem the conduction equation for both materials may be written:

$$\frac{\partial \theta_1}{\partial t} = \alpha_1 \frac{\partial^2 \theta_1}{\partial z^2} \qquad \frac{\partial \theta_2}{\partial t} = \alpha_2 \frac{\partial^2 \theta_2}{\partial z^2} \tag{3.5}$$

The boundary conditions are:

$$\theta_1(z=0,t) = \theta_2(z=0,t) \quad k_1 \frac{\partial \theta_1(z=0,t)}{\partial z} = k_2 \frac{\partial \theta_2(z=0,t)}{\partial z} \quad \theta_1(z=\infty,t) = 0 \quad \theta_2(z=-\infty,t) = 0 \tag{3.6}$$

Finally, the initial condition is the energy exponentially deposited by the laser pulse in material 1.

$$\theta_1\Big|_{t=0} = \frac{\mu_a \phi_0}{\rho_{0,1} c_{p1}} e^{-\mu_a z} \tag{3.7}$$

where ϕ_0 is the fluence incident on the surface of material 1 and c_{p1} is the isobaric specific heat of material 1.

Eq. (3.5) may be solved with the boundary conditions of Eq. (3.6) and the initial conditions of Eq. (3.7) by the method of Laplace transforms to yield the solution for both regions.

$$\theta_1 = \frac{\mu_a \phi_0}{\rho_{0,1} c_{p1}} e^{\mu_a^2 \alpha_1 t} \left[e^{-\mu_a z} - \frac{e^{-\mu_a z}}{2} \operatorname{erfc}\left(\frac{z}{2\sqrt{\alpha_1 t}} - \mu_a \sqrt{\alpha_1 t} \right) + \frac{e^{\mu_a z}}{2} \operatorname{erfc}\left(\frac{z}{2\sqrt{\alpha_1 t}} + \mu_a \sqrt{\alpha_1 t} \right) \left(\frac{k_1 - \sqrt{\frac{\alpha_1}{\alpha_2}} k_2}{k_1 + \sqrt{\frac{\alpha_1}{\alpha_2}} k_2} \right) \right] \tag{3.8}$$

$$\theta_2 = \frac{k_1}{k_1 + \sqrt{\frac{\alpha_1}{\alpha_2}} k_2} \frac{\mu_a \phi_0}{\rho_{0,1} c_{p1}} \operatorname{erfc}\left(\frac{-z}{2\sqrt{\alpha_2 t}} + \mu_a \sqrt{\alpha_1 t} \right) e^{\left(\mu_a^2 \alpha_1 t - \mu_a z \sqrt{\frac{\alpha_1}{\alpha_2}} \right)} \tag{3.9}$$

Eq. (3.8) describes the temperature field in material 1 which determines ρ in Eq. (3.3) with the aid of Eq. (3.4) thus permitting Δz to be calculated. These solutions were verified with the aid of a finite element method (FEM) software package (MATLAB, The Mathworks, Natick, MA). Some sample temperature profiles obtained from Eqs. (3.8-9) are depicted in Figure 3.5.

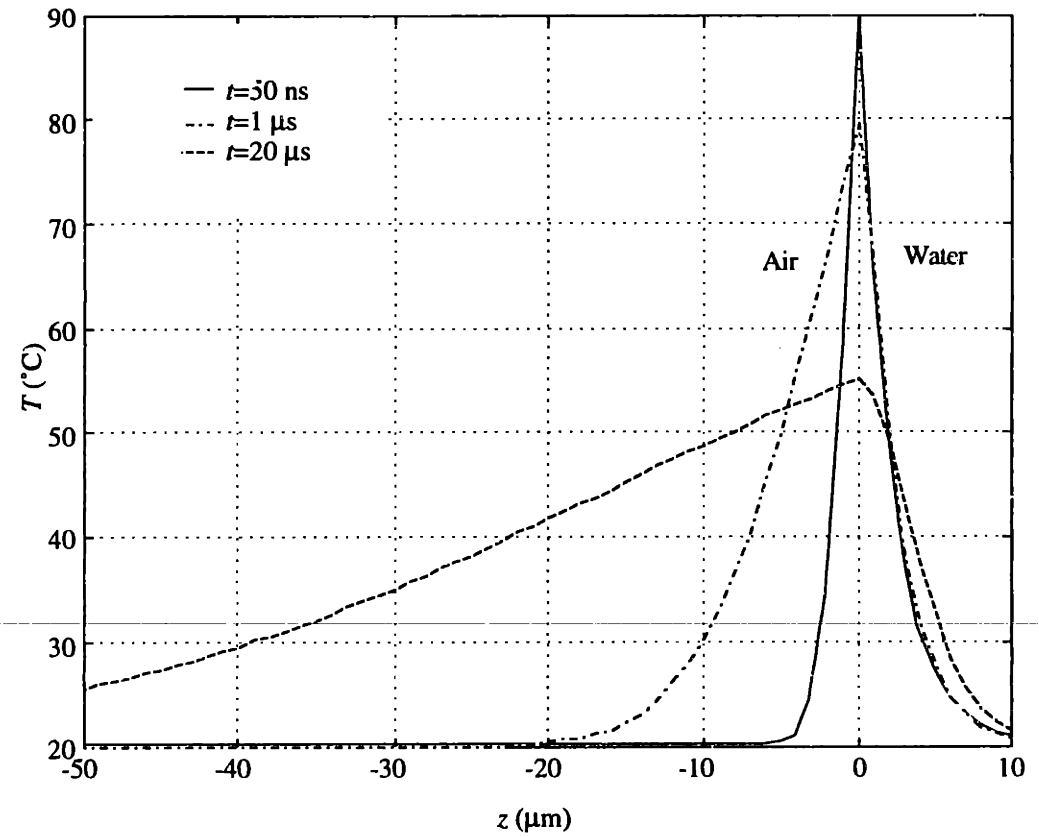

Figure 3.5: Eqs. (3.8-9) plotted for a 650 J/m^2 pulse energy with μ_a=460,900 1/m. Material 1 is water, material 2 is air, and ambient temperature is 20° C.

3.2.2 Surface Displacement

The interferometer is only capable of monitoring the displacement of an interface and proper modeling of this motion requires the consideration of some aspects of acoustic wave propagation. The relative values for the acoustic impedance, Z, of materials 1 and 2 will determine the displacement of the interface. The acoustic impedance of a substance is a material property given by

$$Z = \rho c_a \tag{3.10}$$

where c_a is the sonic velocity in the material. If $Z_1 >> Z_2$, the interface behaves like a traction free boundary and material 2 will offer negligible resistance to material 1 when it thermally expands [39]. Thus the entire thermal expansion predicted by Eq. (3.3) will be manifested as an upward displacement of the interface. This behavior occurs for water or tissue expanding

into air (Z_{water}=1.49 × 10^6 kg/m^2s, Z_{air}=393 kg/m^2s).

In certain situations, as we shall see in the next chapter, a barrier is required to suppress the vaporization of material 1 that results from its rapid heating. This impermeable barrier is chosen to be transparent to the incident laser pulse and also to be *acoustically thin* which implies that it will not impede the expansion of material 1. A layer is acoustically thin if it is much thinner than the acoustic wavelength in question, i.e. $b<\lambda_a/2$, where b is the thickness of the layer and λ_a is the acoustic wavelength of the event (in this case the thermal expansion). If the laser pulse is not mechanically confined ($D<c_a\tau_p$) the acoustic wavelength associated with the laser pulse is given by:

$$\lambda_a = \tau_p c_a \tag{3.11}$$

where c_a is the sonic velocity in the thin layer.

Another way of describing an acoustically thin layer is that the timescale of the acoustic event (τ_p in this case) is long enough to permit the acoustic signal to accomplish a round trip within the thin layer. Thus, the mechanical stress within the thin layer is allowed to equilibrate during the laser pulse and remains essentially uniform throughout its thickness. This situation is depicted in Figure 3.6.

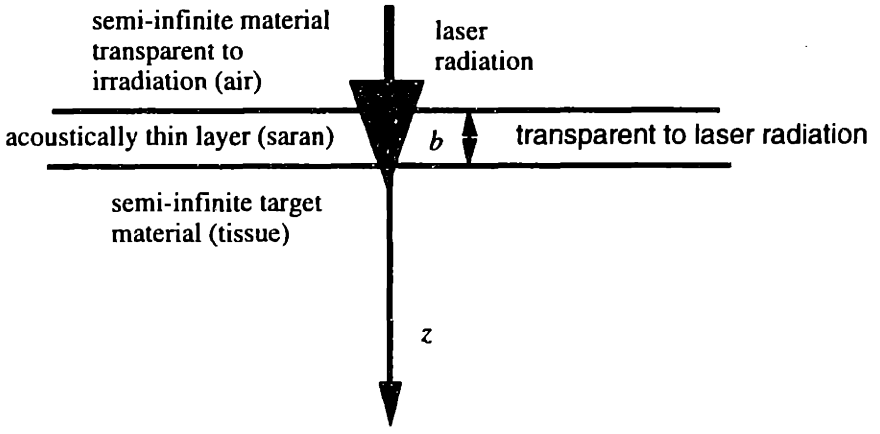

Figure 3.6: Illustration of an acoustically thin layer

If the acoustic impedance of the material above the acoustically thin layer is very small then both interfaces in Figure 3.6 will shift upward by the amount Δz predicted by Eq. (3.3) when the thermal stresses equilibrate (assuming that the thin layer does not undergo any laser heating or any thermal expansion). Consequently, one may measure Δz by measuring the displacement at either interface, and it is worth noting that the interface between air and the acoustically thin layer is usually the easiest interface to monitor due to the fact that it usually has the largest optical reflectivity. According to our convention, Δz is positive for upward surface displacement, consequently if the interface moves in the positive z direction (downward), Δz will be negative.

An acoustically thin layer used in the experiments described in this thesis to block vaporization of water during Q-sw Er:YSGG laser irradiation was a 12.7 μm thick sheet of saran polymer. In previous experiments we confirmed that the saran film absorbs a negligible amount of the 2.79 μm radiation. For this case, $\alpha_{water}=1.46\times10^{-7}$ m^2/s, b=12.7 μm, τ_p=50 ns, D~2.1 μm [17, 99], $c_{a,water}$~1500 m/s, $c_{a,saran}$~592 m/s (calculated based on secant modulus [16]). From these parameters it is easy to show that the laser pulse energy is not mechanically confined but is thermally confined within the water substrate. One can also show that $(\lambda_a/2)$~15 μm > b so indeed the saran membrane is acoustically thin and will not impede the expansion of the water.

For sufficiently short timescales immediately after the laser pulse ($t<<b^2/\alpha_{saran}$), the thin saran film will have the thermal characteristics of a semi-infinite body since the thermal energy imparted by the laser to the water substrate will not have had enough time to traverse the saran film. In that case, the thermal field in the pure water substrate will be described by Eq. (3.8) while the thermal field in the saran layer will be described by Eq. (3.9).

Figure 3.7 depicts $\Delta z(t)$ for Q-sw Er:YSGG laser irradiation of a water substrate covered with a 12.7 μm saran film at different radiant exposures and values of μ_a. The combinations of ϕ_0 and μ_a were chosen so that the initial surface displacement would be the same. The initial water surface temperatures predicted by the model were 106° C, 72° C, and

51° C for the 535 J/m^2, 650 J/m^2, and 756 J/m^2 traces respectively. It is readily apparent from the figure that given the same initial surface displacement, the temporal decay of Δz is sensitive to μ_a so that a careful measurement of the surface displacement can be used to estimate μ_a. This observation comes as no surprise since the time required for heat to diffuse out of a volume scales with the square of its thickness, consequently a relatively small variation in μ_a is expected to result in a relatively large variation in the relaxation time. Moreover one need not accurately measure the fluence imparted by the laser since the initial expansion may be used to estimate this quantity. Thus, this can serve as a fluence independent technique for estimating μ_a, providing the thermophysical properties of the system are known to sufficient accuracy.

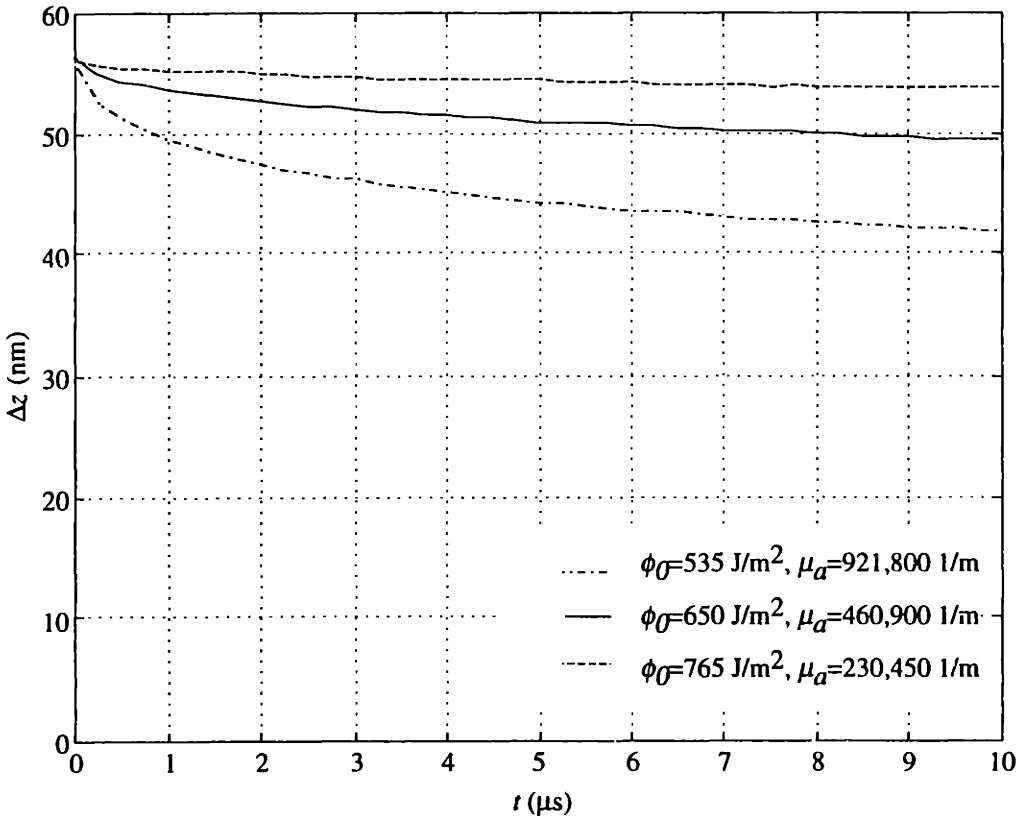

Figure 3.7: $\Delta z(t)$ calculated for Q-sw Er:YSGG laser irradiation of water covered by an acoustically thin saran film. Note the sensitivity to μ_a for a fixed initial Δz.

It is also important to recognize that Eqs. (3.3-4,8-9) are extremely non-linear so that it would appear to be impossible to invert these equations to yield a model that will explicitly

provide μ_a given a surface displacement trace measured by the interferometer. The alternative is to execute a non-linear parameter fitting algorithm, such as the Levenberg-Marquardt method, to estimate both the fluence, ϕ_0, and the effective absorption coefficient, μ_a, given a measured displacement trace.

If μ_a is well characterized, then the model derived here can be combined with measured displacement traces to measure other thermophysical properties appearing in the derivation. For example, if α_1, the thermal diffusivity of the target material, is desired, one can use a Levenberg-Marquardt fitting algorithm to find the value that yields a best fit between the model and the data.

3.3 Verification of Technique: Q-sw Er:YSGG Laser Irradiation of Water

3.3.1 Overview

To test the validity of the model presented in the previous section, the behavior of pure water irradiated by a 2.79 μm Q-sw Er:YSGG laser was investigated experimentally. The 2.79 μm wavelength Q-sw laser was deliberately chosen for several reasons. Firstly, the model requires that the target material must exhibit linear absorption of the heating laser energy (to create an exponentially decaying energy deposition profile). Previous investigators have documented the fact that pure water is a linear absorber of this wavelength providing the volumetric energy density imparted to the water is well below 3000 kJ/m^3 [99, 101]. Secondly, to employ the model the laser pulse must be thermally confined which is achieved for this laser system since τ_p~50 ns (FWHM) and D~2.1 μm>>88nm=$\sqrt{\alpha_{water}\tau_p}$.

For these experiments, an acoustically thin impermeable barrier was required to prevent sub-threshold vaporization of the water as discussed in the next chapter. Ordinary saran wrap was found to be a suitable barrier as it is highly impervious to water [16] and is acoustically thin. It is interesting to note that other workers have employed a plastic film to inhibit

evaporation from laser irradiated tissue samples, although these experiments involved continuous wave (cw) irradiation [93].

3.3.2 Experiment Design

Samples of pure, deionized, triple distilled water were prepared in 7 ml scintillation vials (Fisher Scientific) and were covered with saran film (Dow Brands). The saran film was heat sealed onto the water samples with a standard heat gun in order to ensure a wrinkle free, taut film. The saran was previously determined to absorb <5% of the incident 2.79 μm radiation by employing an energy meter to measure the fluence of a laser pulse both before and after traversing a single layer of the film. A Schwartz SEO 1-2-3 laser system with an Er:YSGG rod was Q-switched with a mechanical rotating rear cavity mirror. A diagram of the set up and geometry is presented in Figs. 3.8-9.

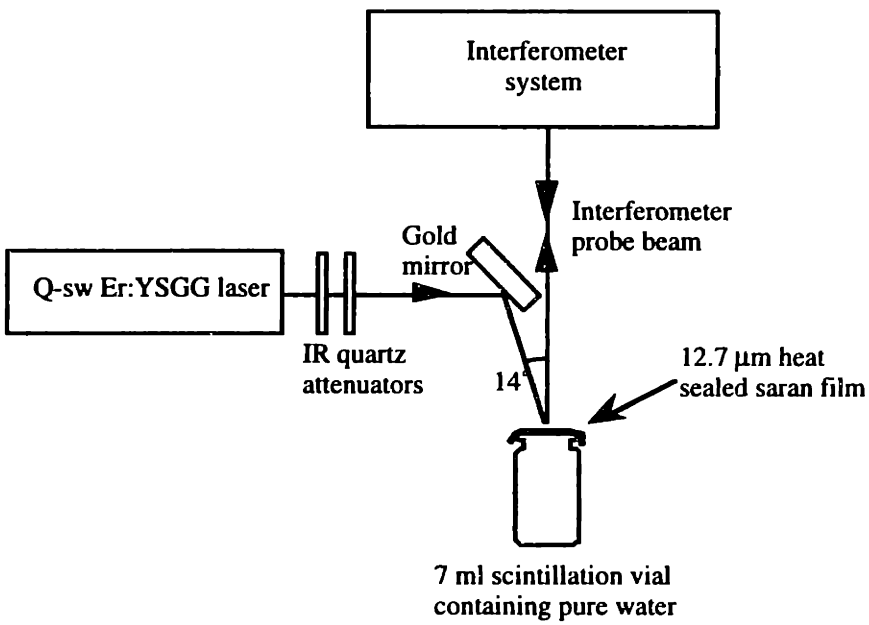

Figure 3.8: Schematic of experimental set up for Q-sw Er:YSGG irradiation of saran covered water samples

The interferometer probe beam was confocally imaged onto the saran-air interface with a 125 mm focal length lens at normal incidence. Since the HeNe beam entering the lens was collimated and 10 mm across, the focal spot was about 15 μm across. The depth of focus of the

focused HeNe beam was about 700 μm in total. The interferometer beam remained fixed during the experiment and due to the very short depth of focus, defined a fixed zone in space where data was acquired. The heating of the water by the HeNe probe beam was negligible due to the small absorption and scattering of water and saran film at 632.8 nm.

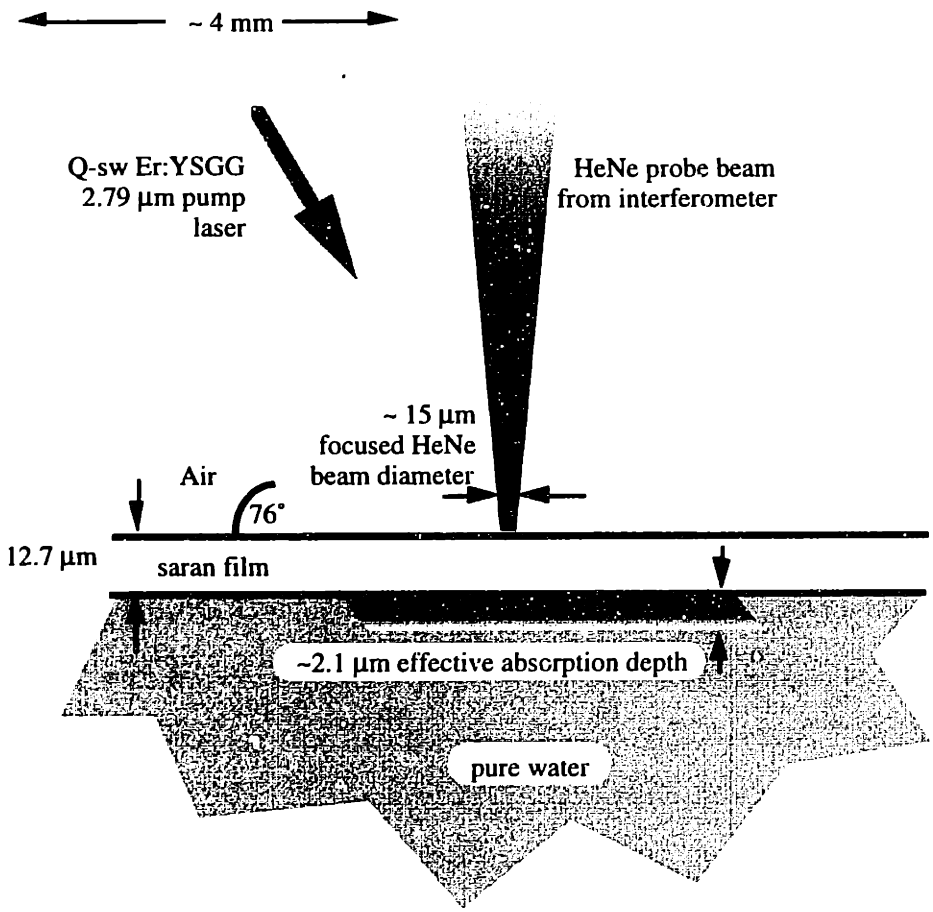

Figure 3.9: Expanded view of Er:YSGG irradiation of saran covered water samples

The Er:YSGG pump laser beam was inclined at a 14° angle (in the air above) to the HeNe probe beam in order to permit the HeNe probe to approach the saran-water system at normal incidence from the top side. The index of refraction of pure water at 2.79 μm is 1.315 [17] so within the pure water the laser radiation propagates at 10.6° to the vertical. Thus, the measured effective absorption depth of the 2.79 μm radiation was about 0.98 (given by cos(10.6°)) of its actual value. μ_a for 2.79 μm radiation in water is quoted as 460,900 1/m

(D=2.17 μm) in [17] and 516,000 1/m (D=1.94 μm) in [99].

The Er:YSGG laser system delivered 25 mJ pulses with a duration of 50 ns (FWHM) at a repetition rate of about 1 Hz with a transverse beam diameter of about 4 mm. The beam was aligned to be concentric with the interferometer probe beam on the saran film surface with the aid of gold mirrors. Unfortunately, the mechanical Q-switching mechanism employed in the Er:YSGG laser resulted in significant shot to shot variations in both spatial mode shape and pulse energy. Since a laser beam analyzer was not available, it was not possible to accurately measure the local laser fluence deposited in the region of the interferometer probe beam. This ambiguity was not seen to be a significant disadvantage since the model presented in the preceding section can be used to estimate μ_a in a fluence independent manner. Approximate variations in local fluence were accomplished by placing IR quartz attenuators in the path of the Er:YSGG laser.

3.3.3 Results

At the interferometer probe beam wavelength (632.8 nm) the index of refraction mismatch between the saran (n=1.6) and air (n=1) resulted in a reflectivity of 5.3% while the index mismatch between the saran film and the water (n=1.33) resulted in a reflectivity of 2%. Thus the interferometer signal was reflected primarily from the saran-air interface.

As the water substrate cools, it transferred its thermal energy to the saran. The saran thermally expands ($\alpha_{T,saran}$=1.9×10^{-4} K^{-1}), although to a lesser extent than the water, whose thermal expansion coefficient is strongly temperature dependent over the range 20° C - 100° C ($\alpha_{T,water}$=2.1-7.5×10^{-4} K^{-1}). Since the interferometer was actually measuring the displacement of the saran-air interface, this effect was accounted for when calculating the predicted $\Delta z(t)$. The thermal expansion of the saran, $\Delta z_{saran}(t)$, was added to $\Delta z(t)$ as given by Eq. (3.3). $\Delta z_{saran}(t)$ was given by

$$\Delta z_{saran}(t) = \alpha_{T,saran} \frac{Q_{water \rightarrow saran}(t)}{\rho_{saran} c_{p,saran}} \qquad \text{Eq. (3.12)}$$

where $Q_{water \rightarrow saran}(t)$ represents the total thermal energy conducted from the water to the saran

(the heating of the saran by the laser pulse was neglected due to the weak absorption of 2.79 μm radiation by saran). If the laser pulse is assumed to begin at time t=0 then $Q_{water \to saran}(t)$ is given by:

$$Q_{water \to saran}(t) = \int_0^t k_{water} \frac{\partial \theta_{water}(z=0,\tau)}{\partial z} d\tau \tag{3.13}$$

In general, $\Delta z_{saran}(t)$ amounted to less than 10% of the net surface displacement.

Three sample data traces are presented in Figure 3.10. As discussed above, the exact laser fluence for each trace was unknown. Notice that for increasing initial Δz, the amount of relaxation in Δz during the 10 μs trace increases. This can be explained by the non-linear thermal expansion of water (i.e. the thermal expansion coefficient of water increases with increasing temperature). For a fixed amount of energy conducted from the water into the saran film above it, a higher initial temperature field results in a larger downward surface displacement.

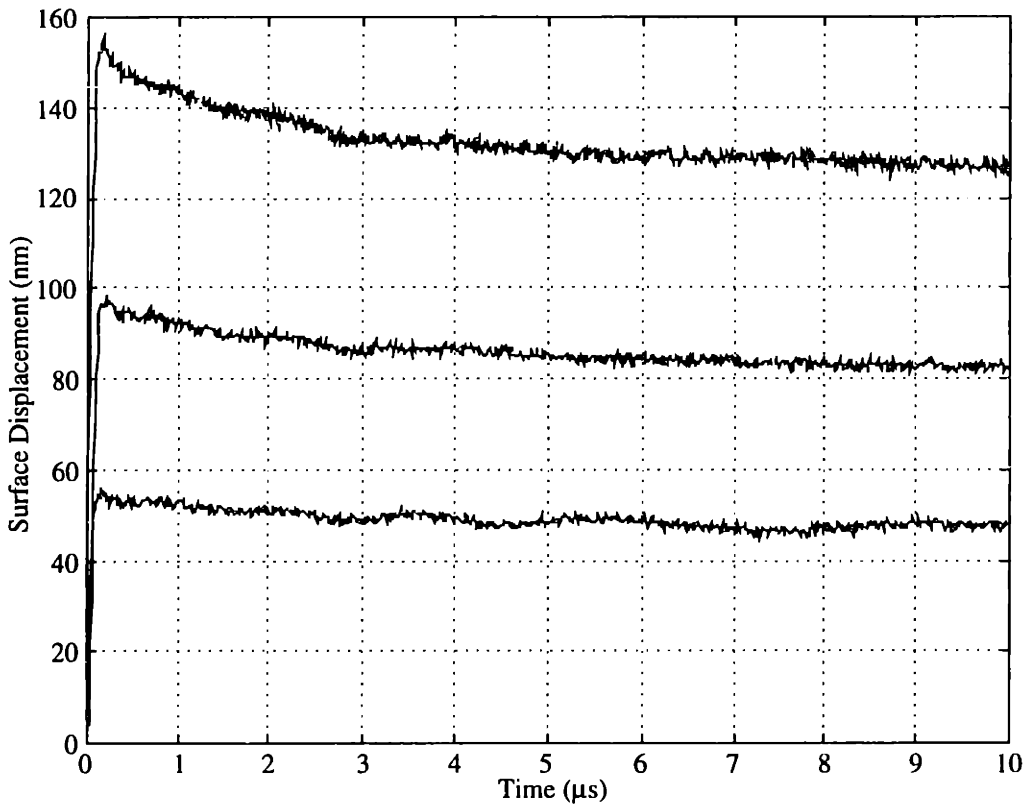

Figure 3.10: Sample interferometer traces obtained for Q-sw Er:YSGG laser irradiation of saran covered water

Note the presence of nanometer scale microsecond duration ripples in the traces. These ripples are presumably due to acoustic waves on the surface of the sample and may be a function of the smoothness of the laser transverse beam profile and the tautness of the saran film. It was observed that a gaussian transverse beam profile yielded small ripples (like the ones depicted here) while an irregular transverse beam profile yielded ripples large enough to obscure the displacement relaxation.

A Levenberg-Marquardt non-linear fitting algorithm (MATLAB, The Mathworks, Natick, MA) was employed to fit the model to fourteen data traces by determining the best value for μ_a and ϕ. This procedure was performed separately for each data trace and thus 14 sets of μ_a and ϕ were obtained. The chi-squared statistic was used to estimate the goodness-of-fit of the model for each trace and based on this, several data traces were rejected [67]. From the remaining values of μ_a, a single μ_a was computed based on the weighted average of the set of μ_a values. The weighting for each value was based on the goodness of fit between the model and the data. Specifically, the inverse of the residuals was employed to weight each μ_a value. In this way, μ_a was estimated to be 520,000 1/m with a weighted standard deviation of 50,000 1/m (or 9% of the mean value). If we assume that the estimated values for μ_a are normally distributed, then the 5%-95% confidence interval on μ_a is approximately 440,000-600,000 1/m. The expected range of μ_a based on published water spectra is 460,900-516,000 1/m [17, 99] and this range of values lies well within the 5%-95% confidence interval.

A sample data trace is directly compared with three traces predicted by the model for three different combinations of μ_a and ϕ_0 in Figure 3.11. For the sample data trace shown, the best fit parameter set was found to be ϕ_0=956 J/m^2 and μ_a=495,000 1/m. Note that fitting was performed for the range over which the surface ripples were smallest, from 1.5 μs to 9.5 μs after the laser pulse ended. For comparison purposes, note that at t=5 μs, the model predicted the saran-water interface temperatures to be 67° C, 73° C, and 79° C for the 1015 J/m^2, 956 J/m^2, and 923 J/m^2 traces respectively.

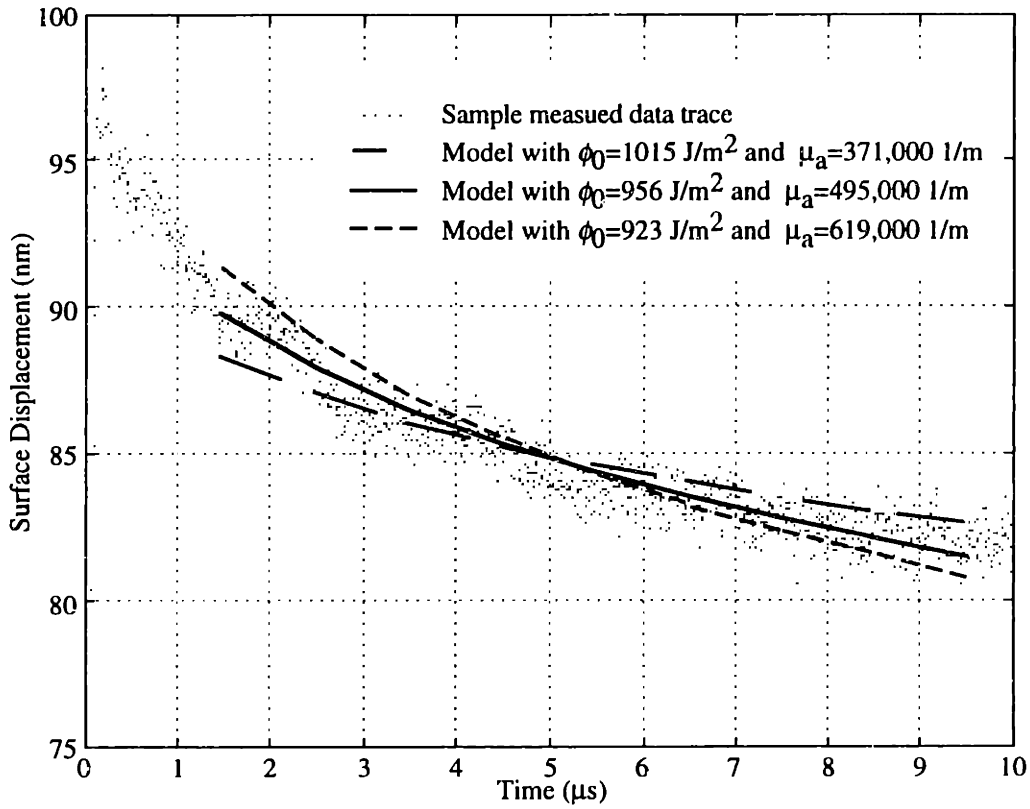

Figure 3.11: Comparison between measured surface displacement and predicted Δz for 3 different combinations of μ_a and ϕ_0. The best fit set of parameters for this measured data trace was found to be ϕ_0=956 J/m^2 and μ_a=495,000 1/m.

3.4 ArF Excimer Irradiation of Bovine Cornea

3.4.1 Overview

The goal for the pilot study was to measure the absorption coefficient, μ_a, of 193 nm radiation in cornea because the 193 nm wavelength ArF excimer pulsed laser is clinically used for surgical eyesight correction. The actual effective penetration depth of this radiation in cornea remains poorly understood as widely disparate values have been quoted in the literature [19, 20, 62, 64, 68, 88, 89]. This μ_a may in fact depend on corneal hydration state and on the local energy density so that the laser energy is not deposited according to an exponential temperature profile [19, 20, 64, 89]. Understanding this μ_a is critical for understanding and modeling the dynamics of ArF excimer corneal laser ablation.

The cornea is a transparent structure serving as the outer covering for the front of the eye. It is approximately 600 μm thick in humans and consists of several layers. The cornea provides most of the refractive power responsible for focusing an image on the retina. The middle layer of the cornea, the stroma, comprises the majority of its mass (>90%) and is responsible for its structural integrity. Since PRK is primarily concerned with ablation of the stroma, the goal of this experiment was to measure μ_a for corneal stroma. The stroma is approximately 78% water by mass and the balance proteins and other chemicals. Collagen is the main protein in the stroma, comprising about 15% of its mass. Fibers of collagen are organized into sheet-like lamellae, approximately 2 μm thick. Within the lamellae, the fibers all point in the same direction and the lamellae are stacked atop each other with fibers orientated at right angles to the fibers in the neighboring lamellae. This regular structure is thought to contribute to the transparent nature of the cornea [46, 72].

At 193 nm, μ_a for water is approximately 1 m^{-1} [89]. It is thought that the collagen in the corneal stroma serves as the primary absorber of the 193 nm radiation, although some authors have conjectured that the water becomes a strong absorber of the 193 nm radiation once it is heated by the absorbing collagen [89]. In addition, experiments have shown that the hydration state of the cornea has a significant impact on its absorption characteristics at 193 nm, and that the absorption has a time varying behavior [19, 20, 64].

The study was performed on bovine cornea *in vitro* in an effort to minimize the dangers and complexity of the experiment, although there is no fundamental reason why the experimental study presented here could not be performed on human cornea *in vivo*. There are some minor differences between the structure of bovine cornea and human cornea. However, these differences are not thought to affect the ablation dynamics of the stroma or its spectroscopy [62]. In the experiment reported here, calf eyes were employed here to avoid any of the blemishes sometimes found on mature bovine corneas and also to best mimic the geometry of human eyes.

As is the case for Er:YSGG irradiation of pure water, an acoustically thin barrier was

employed to ensure that vaporization of cornea tissue constituents during the measurement did not interfere with the estimation of μ_a. Moreover, the barrier helped guard against dehydration of the cornea. The 193 nm radiation produced by the ArF excimer laser is not transmitted by organic materials such as the saran employed for the Er:YSGG experiments. However pure silicon dioxide is a good transmitter of this UV wavelength. Borosilicate glass (type KG33, Kimble glass) was selected due to its high silicon dioxide content. Furthermore, borosilicate glasses are noted for their extremely low thermal expansion coefficients ($\alpha_{T,KG33}$=3.2×10^{-6} K^{-1} [38]) so that unlike the saran membrane employed for the Q-sw Er:YSGG experiments, the thermal expansion of the glass membrane was negligible. The glass was blown by a skilled glass blower into spheres which were shattered and the resulting 10 μm thick shards of glass were draped over the bovine cornea like a contact lens. Since the laser pulse energy was not mechanically confined (τ_p~20ns [FWHM] and $c_{a,KG33}$~5640 m/s [38]) and b=10 μm, one can show $b<<\tau_p c_{a,KG33}/2$, and we conclude that the glass membranes were indeed acoustically thin.

3.4.2 Experiment Design

A Lambda-Physik LPX300 series excimer laser was used with an ArF gas fill to produce 600 mJ pulses with a duration of 20 ns FWHM at a repetition rate of 1 Hz. An aperture was used to select the central 4 mm disk of the 10 by 25 mm raw rectangular beam output. The beam energy as controlled with UV quartz attenuator plates of various thickness. A pyroelectric detector (Molectron Detector, Portland, OR) was used to measure the energy in each pulse. This was calibrated against a broadband pulse energy meter (Molectron Detector). The experimental setup is depicted in Figure 3.12. As for the Er:YSGG experiments described earlier, the plane of focus for the interferometer HeNe beam served to define a fixed reference plane. The ArF beam was aligned to be concentric with the HeNe probe at the reference plane. The transverse beam profile was measured at this plane by stepping a pyroelectric detector (Molectron Detector) with a 1 mm diameter aperture through the beam. The beam analysis permitted an estimate of the local fluence for each laser pulse. In general, the shot to shot energy variation of the ArF laser was less than 3%.

The fluence measurement was adjusted for the expected reflection coefficient of 193 nm radiation incident at 14° incidence on an air-glass incidence. The fresnel reflectivity for both TE and TM reflection can readily be computed to be about 5% assuming the index of refraction for the glass is about 1.55 at 193 nm. The reflectivity of the glass-cornea interface can be shown to be negligible if the real part of the index of refraction for cornea is assumed to be 1.33 or higher (n_{water}=1.33 for visible light, Real(n_{cornea}) was measured to be 1.52 for 193 nm radiation [62]). Thus, the glass membrane was not expected to behave as a Fabry-Perot etalon with respect to the 193 nm radiation and thus multiple reflections within need not be considered.

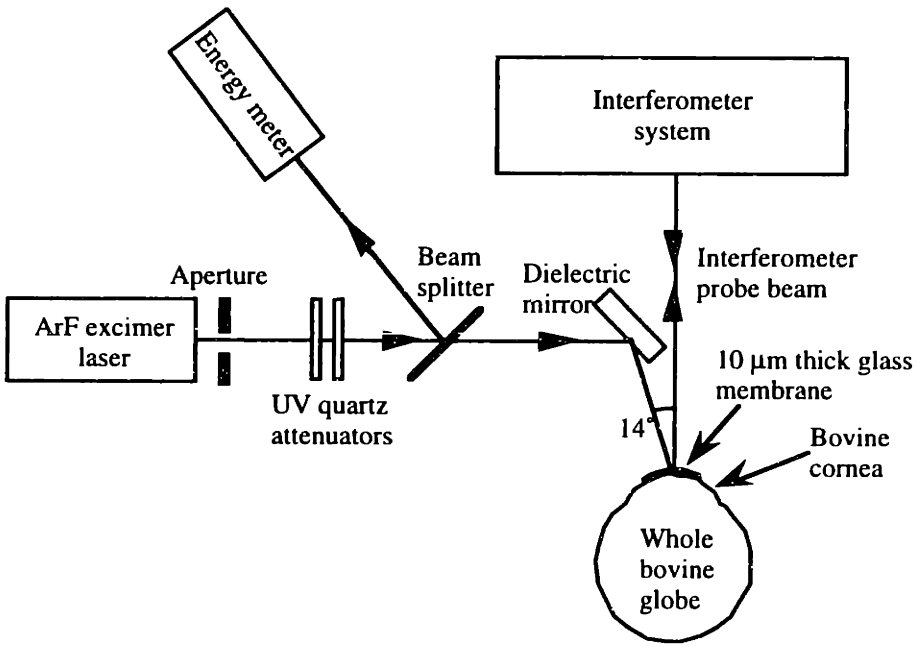

Figure 3.12: Schematic diagram of setup for ArF irradiation of bovine cornea

Whole bovine globes were obtained from a local slaughterhouse and used within 24 hours. The globes were maintained on ice and allowed to attain room temperature prior to the actual experiments. The epithelium covering the corneal stroma was removed by dragging a razor blade across the corneal surface and the exposed stroma was wiped dry with lens tissue. A membrane of glass with an appropriate curvature was draped over the exposed stroma. The glass membranes were about 10 μm thick as measured by a micrometer and were about 5 mm across. Figure 3.13 contains an expanded view of the experimental setup. The globes were

mounted in a 3-axis positioning mount that permitted the glass covered sections of cornea to be precisely positioned into the focal plane of the interferometer probe beam (and hence the irradiation of the ArF beam). The heating of the cornea and glass film by the HeNe probe laser beam was ignored due to the negligible absorption and scattering of glass and cornea at the 632.8 nm HeNe laser wavelength.

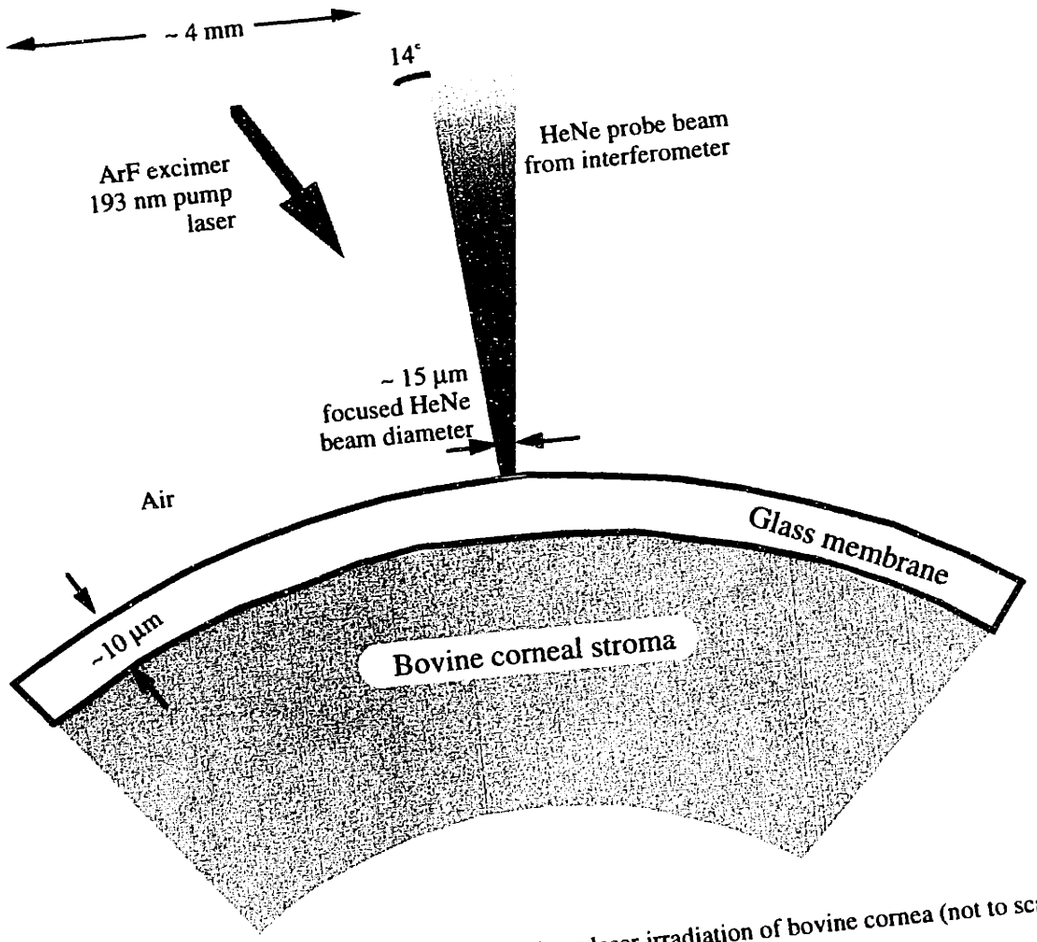

Figure 3.13: Expanded view of setup for ArF excimer laser irradiation of bovine cornea (not to scale)

Displacement traces were acquired for several eyes at a variety of fluence values. Many traces were acquired under the same conditions at the same site on the same cornea, but since no "incubation effect" has been documented for ArF irradiation of cornea [63], and since sub-ablative fluences were used, the effect of repetitive irradiation of the same stroma site was not

considered, nor was it observed. After the conclusion of experiments on an individual cornea, the glass membrane was peeled off the cornea. The corneal stroma under the glass membrane was slightly raised (by ~200 μm) relative to the uncovered corneal region. This was attributed to dehydration of the corneal stroma that was not covered by the glass membrane.

3.4.3 Results

Sample traces obtained by the interferometer for ArF excimer laser irradiation of glass membrane covered bovine corneal stroma are presented in Figure 3.14. In this figure, the time is measured with respect to the initiation of upward motion of the surface displacement.

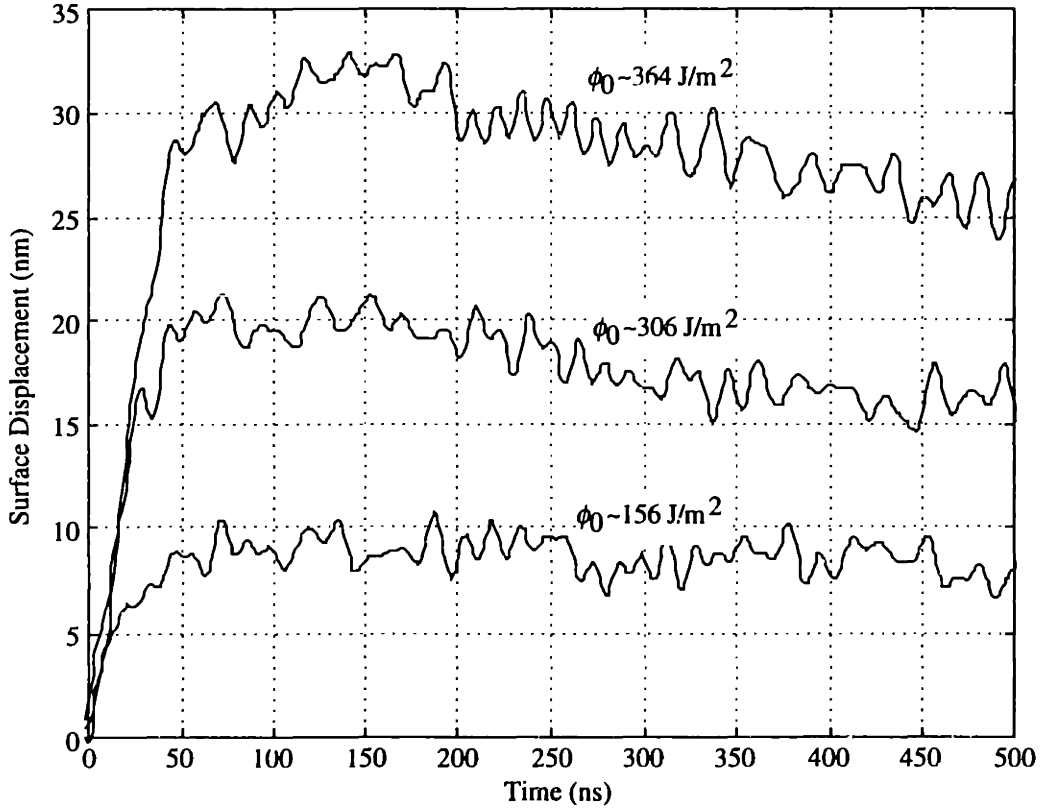

Figure 3.14: Typical traces obtained by interferometer for ArF excimer laser irradiation of glass membrane covered bovine corneal stroma

Note the extremely small vertical scale in Figure 3.14 and that the noise level is about ± 1 nm. Providing D <<30 μm (which seems assured given the range of published values for this parameter), the 20 ns FWHM ArF excimer laser pulse is not mechanically confined. The

rise time of the lower traces corresponds to the 20 ns FWHM duration of the ArF laser pulse and this is a consequence of the fact that the laser pulse energy is not mechanically confined so that thermal expansion occurs on the timescale of the laser pulse. As in Figure 3.10, the amount of downward surface relaxation increases with increasing fluence. This is not surprising since for a fixed amount of energy conducted from the heated corneal stroma into the glass membrane, more surface motion is expected to occur at higher temperatures due to the non-linear dependence of water density on temperature. The timescale for relaxation is much faster in these traces compared to those in Figure 3.10 and this is indicative of a more shallow penetration depth (higher μ_a).

The model can only be fit to the data over a finite time interval. The model assumes an instantaneous energy deposition and consequently is not expected to agree with the data during and immediately after the laser pulse (<150 ns). At times longer than 500 ns after the laser pulse, significant acoustic effects corrupted the data traces, and so only the first 500 ns of the data traces were suitable for μ_a estimation. This acoustic effect is not surprising since the corneal stroma is not really a semi-infinite body; it doesn't take much longer than 500 ns for an acoustic wave to travel from the front side of the cornea to the rear side (~600 μm), and return again to the front side if $c_{a,water}$ (~1500 m/s) is assumed.

Due to the lower signal to noise ratio in the traces, many traces obtained at the same fluence were averaged to generate a smoother single trace for a given fluence. The thermo-physical properties of corneal stroma are not well tabulated in the literature and most authors (see for example [6, 21, 82]) have assumed they are very similar to those of water due to the high water content of the stroma (78% by mass). For this reason, the properties of cornea were assumed to be equivalent to those of water for this study. A non-linear parameter fitting algorithm employing the Levenberg-Marquardt method (MATLAB, The Mathworks, Natick MA) was then employed to determine the best fit values for ϕ_0 and μ_a. ϕ_0 was used as a fitting parameter despite the fact that it was explicitly measured during the experiment since the fit between model and data is extremely sensitive to ϕ_0 and in practice it is nearly impossible to

measure it to better than 5% accuracy due to the difficulty in accurately measuring the laser beam transverse profile. Only the traces obtained at the highest fluences (> 300 J/m^2) were used for the estimation of μ_a since traces at lower fluences (<300 J/m^2) are much less sensitive to μ_a due to the weaker non-linearities in the dependence of water density on temperature.

The non-linear fitting procedure yielded the value μ_a=19,400 cm^{-1} (D=515 nm). The chi-squared statistic was employed to demonstrate the goodness-of-fit between the model and the data [67]. To obtain a confidence interval on the estimate of μ_a, a Monte Carlo technique for generating synthetic data sets with the same statistical characteristics as the actual data set was employed [67]. This technique assumed that the individual data points were normally distributed around the "true" value with a characteristic error. The resulting 5%-95% confidence interval for μ_a was 1,600,000-2,300,000 1/m (D=435-633 nm).

The averaged data trace used for the μ_a estimation is presented in Figure 3.15 along with predicted traces for a few combinations of μ_a and ϕ_0. The values for μ_a depicted in the plot include 270,000 1/m cited in [68], a recently measured value of 3,990,000 1/m cited in [62], and the best fit value found in this study. The values from the literature clearly do not fit the data as well as 1,940,000 1/m. For comparison purposes, the cornea-glass interface temperatures predicted by the model at t=350 ns were 34° C, 75° C and 96° C for traces with μ_a equal to 270,000 1/m, 1,940,000 1/m, and 3,990,000 1/m respectively.

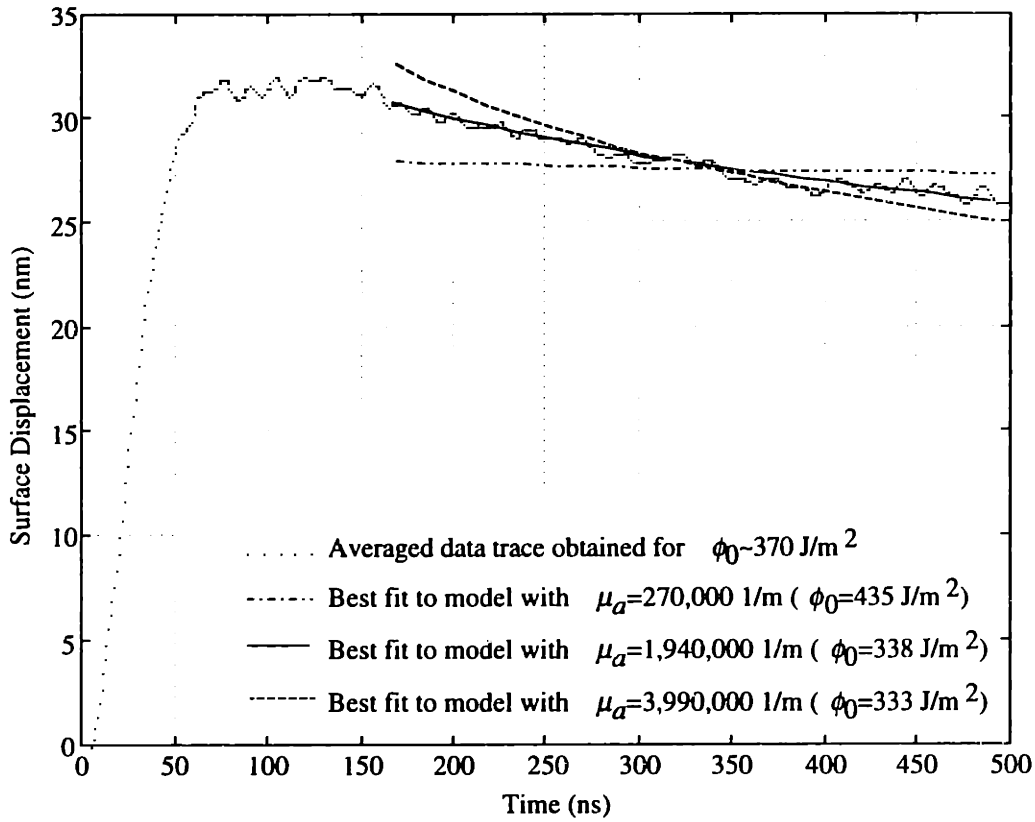

Figure 3.15: Comparison between averaged data trace and best fit to model for three values of μ_a

To analyze the data at early times (<150 ns), the governing equations were implemented numerically using a finite element method (FEM) partial differential equation solver (MATLAB, The Mathworks). An analytical function was fit to the ArF excimer laser pulse temporal profile measured by a single nanosecond rise time detector (Molectron Detector) and was used for the FEM solution. The FEM solution was not used with the Levenberg-Marquardt fitting algorithm as it required far too much time for computation. In Figure 3.16 the FEM solution using the best fit parameters for μ_a and ϕ_0 is compared to the measured data. A significant discrepancy is apparent at times earlier than 100 ns after the start of the laser pulse. In contrast to the data, the best fit model reaches its maximum surface displacement at the conclusion of the laser pulse, 50 ns after it began. The measured data trace lags behind, and achieves its maximum surface displacement at around 100 ns after the start of the laser pulse. The maximum temperature occurring in the FEM solution's predicted temperature field is 121° C at z=126 nm and t=52 ns. The presence of tissue water in a metastable state should not disturb the reader since this

situation persists for only a few tens of nanoseconds and moreover Eq. (3.4) is valid up to 150° C.

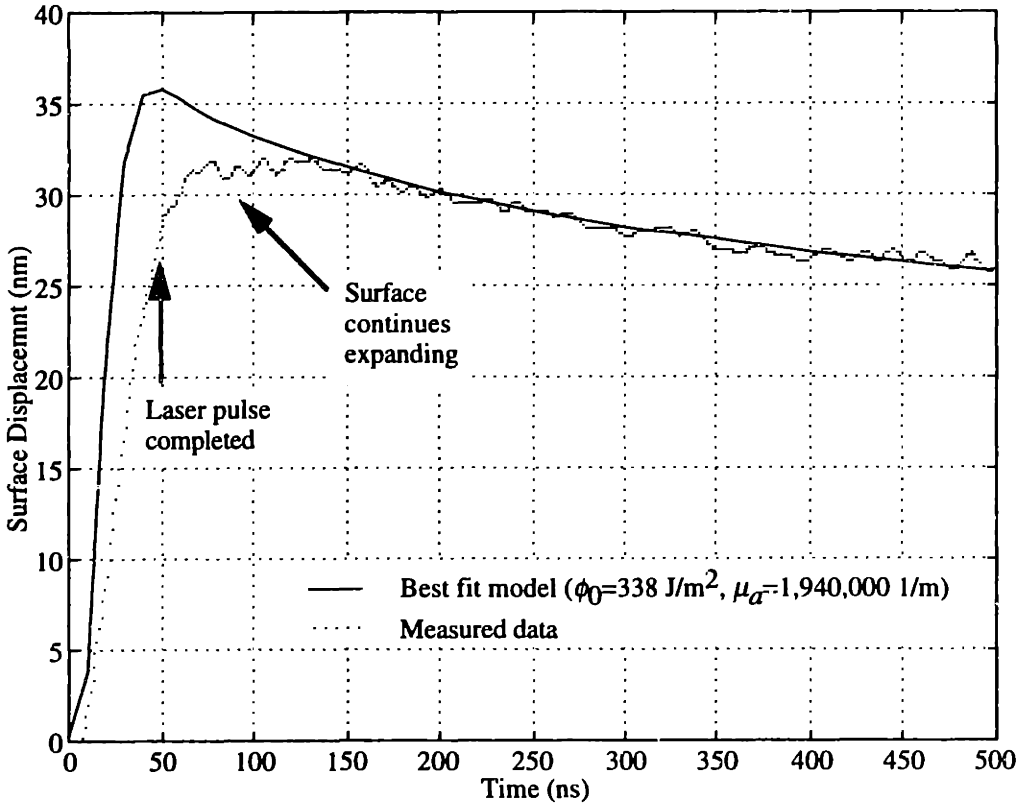

Figure 3.16: Comparison between FEM solution and data for best fit value of μ_a and ϕ

For comparison purposes, the temporal profile of the ArF excimer laser pulse is presented in Figure 3.17. Note that the weak tail of energy following the laser pulse is not sufficient to account for the discrepancy. Moreover, the discrepancy cannot be resolved by invoking non-linear absorption behavior that would lead to a non-exponential spatial energy deposition profile. Aside from the possibility that the corneal stroma has unusual non-linear thermal expansion characteristics, the only other explanation for the discrepancy at early times is that some of the laser pulse energy is not fully thermalized until 100 ns after the laser pulse ends.

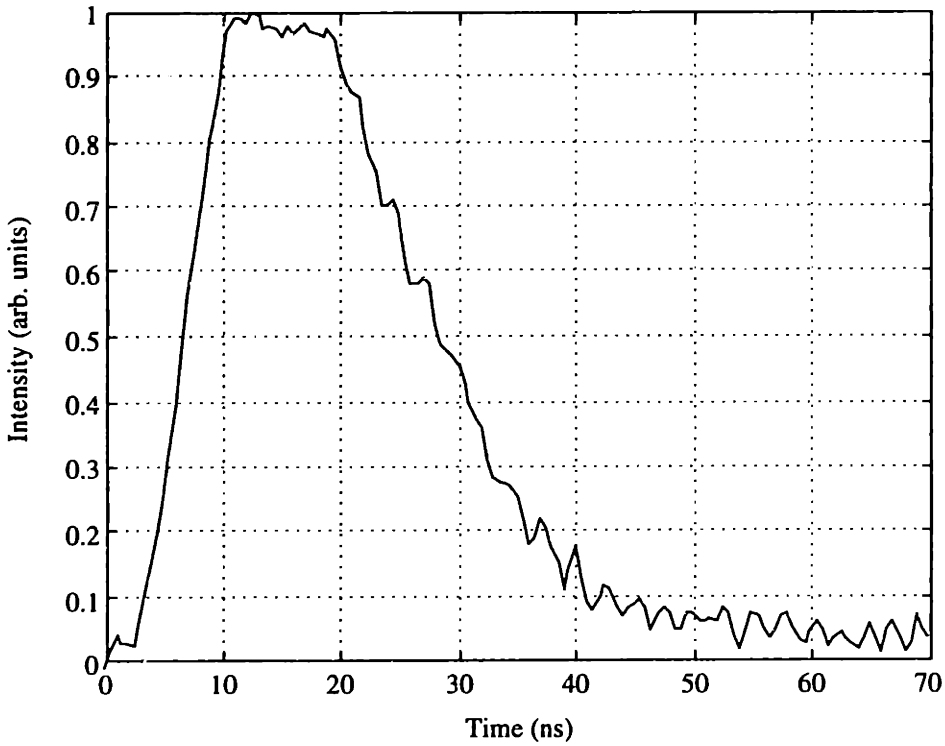

Figure 3.17: ArF excimer laser temporal profile

3.4.4 Discussion

At the outset, it must be noted that several potentially important effects were ignored in this study. Firstly, as mentioned earlier, the thermo-physical properties of corneal stroma are not known, and moreover, are likely to vary with temperature. Due to the high water content of the corneal stroma, the thermo-physical properties were assumed to equivalent to those of water. The corneal stroma was treated as a liquid with a Poisson's ratio of 0.5 in Eq. (3.3) since the temperature driven volume expansion properties of water were expected to dominate over any volume restraining effects resulting from the collagen matrix [6]. Secondly, the structure of the cornea suggests that there may be heterogenaeities on the same spatial scale as the measured effective absorption depth since the individual collagen lamellae are said to be about 2 μm thick [46]. However, if the structure of the lamellae is such that the relative concentration of collagen and water does not vary on this scale, the influence of this heterogenaeity would be negligible.

The hydration state of the cornea has been shown to play a critical role in determining its spectroscopic properties [19, 20]. In this study care was taken to ensure that the hydration state of the cornea was maintained at its proper physiological level. Indeed, it was evident that the glass membrane inhibited desiccation of the cornea surface on the timescale that it took to perform a set of measurements on a single eye (~20 minutes). After a set of measurements were completed the areas covered by the glass membrane were about 200 μm higher than the other areas where the was no glass coverage.

In [62] the authors provide evidence that the value for μ_a cited in [68] is likely to have been corrupted by problems with the sample preparation. These authors also document that the existence of a thin water layer between the prism and the cornea in their own experimental apparatus may have led them to overestimate μ_a (and underestimate D) [62]. The authors state that the water layer might result from pressure applied on the cornea by the prism. In unpublished experiments, we have observed that pressure applied to the corneal stroma does indeed causes it to "sweat" significant amounts of moisture, perhaps in the same manner that a sponge surrenders moisture when compressed. Consequently, we believe that the primary reason for the discrepancy between the value for μ_a measured here and that cited in [62] is the formation of a pressure induced water layer in their experimental apparatus. On this basis, we believe the value measured here to be the most accurate measured to date.

The IPTS measurement of μ_a was done near ablation threshold radiant exposures as compared to the measurement in [62] which was done at very low fluences. It is possible that the μ_a depends on the local energy density as has been demonstrated for Er:YAG laser irradiation of water [12, 99]. If so, then in order to reconcile the measurements here with those in [62], μ_a would need to decrease with increasing local energy density. However, in [89] the authors show that μ_a is expected to increase with increasing local energy density.

The value of the absorption coefficient, μ_a, is critical to understanding the dynamics of ArF excimer laser ablation of corneal tissue since this parameter determines how the laser energy is deposited. At this point in time, there is some debate in the literature as to whether the

ablation process is driven by purely thermal or partially photochemical processes. Srinivasan and co-workers have proposed that corneal ablation proceeds via "ablative photodecomposition" as has been demonstrated for ArF excimer laser ablation of organic polymers [26, 87, 88]. Their hypothesis is that the collagen matrix in the cornea is photochemically decomposed into smaller molecular fragments by the high energy (6.4 eV) 193 nm photons. The higher specific volume and high kinetic energy of these fragments is said to drive the material removal process.

This theory cannot however, explain the absence of an incubation effect, that is repeated subablative irradiation of corneal tissue by 193 nm laser radiation does not seem to alter the chemistry of the collagen matrix and result in a lowered ablation threshold as is the case for 193 nm laser irradiation of organic polymers [63]. Other authors have proposed a purely thermal mechanism for material removal. Venugopalan and co-workers used a stress transducer to obtain data consistent with a rapid surface vaporization of porcine dermis exposed to ablative ArF excimer laser pulses [94, 95]. Like cornea, porcine dermis is also primarily collagen and water, although the mass ratio is slightly different from that in the cornea, and the collagen in dermis is not organized in a regular laminar structure. Staveteig and Walsh have proposed that ArF excimer laser ablation of collagen based tissue is primarily thermal in nature and that the water becomes an active chromophore once heated by an initial amount of collagen absorption [89].

One model describing ArF excimer laser ablation of corneal tissue is the blowoff model, whereby a threshold level of energy per unit volume must be absorbed by the corneal tissue in order for ablation to commence in that volume. This model assumes that the laser pulse energy is fully deposited before material removal commences. This ablation commences from the surface of the corneal tissue, rather than via a subsurface explosion as is the case for Er:YSGG or CO_2 ablation of tissue [96].

The surface displacement model presented in this thesis assumes that all of the energy imparted by the laser pulse is thermalized. The comparison between the FEM solution and the measured data (Figure 3.16) seems to indicate that for times less than 150 ns after the laser

pulse, the energy may not be thermalized since the cornea continues to expand even after the laser pulse has ceased. However, for times more than 150 ns after the start of the laser pulse, the excellent fit between model and data suggests that the pulse energy is fully thermalized. One possible explanation is that the laser pulse energy requires many nanoseconds to be transferred from the proteins and bound water to the free water which comprises most of the mass of corneal tissue. Another explanation is that some of the pulse energy manifests itself chemically rather than thermally at times less than 150 ns after the laser pulse. Other workers have noted that ablation characteristics at the fifth harmonic of the Nd:YAG laser (213 nm) are similar to those at 193 nm [71-74, 89]. It would be interesting to repeat the measurements here with a Nd:YAG pump laser beam to see how much time is required for the thermalization of 213 nm laser radiation.

3.5 Conclusions and Future Directions for IPTS

In this chapter, we have developed the IPTS technique, derived the relevant analytical model, and demonstrated that the technique can be used for estimating the effective absorption coefficient through measurements performed during Q-sw Er:YSGG laser irradiation of water. Significantly, we have successfully used the IPTS technique to estimate the effective absorption coefficient of ArF excimer laser radiation in bovine cornea.

Comparisons between the full FEM solution and the simpler analytical model for IPTS have shown that after the laser pulse has ceased, the surface motion is not particularly sensitive to the shape of the initial energy distribution profile. Thus, the IPTS technique is not a good way to assess unusual energy deposition profiles due to dynamic optical properties such as saturation of the chromophore. Rather, the IPTS technique is better suited to estimating the overall characteristic absorption depth incorporating any dynamic optical properties. This is not surprising since the diffusive nature of heat conduction rapidly smoothes sharp gradients in a temperature field and thus causes the thermal fields resulting from different initial temperature

distributions to resemble each other. However, even an estimate of the effective absorption depth is often very useful information as is the case for 193 nm laser irradiation of cornea.

The results presented here strongly suggest that many nanoseconds are required for the full thermalization of the ArF excimer laser pulse in bovine cornea. This may be explained by either a delay in the transfer of energy from the corneal proteins to the free water or by photochemical activity of the proteins. Future work should be directed towards exploring this energy thermalization and the implications for ablation of corneal tissue. One initial experiment should be an investigation of 213 nm (fifth harmonic) Q-sw Nd:YAG irradiation of cornea.

As of yet, IPTS has not been employed *in vivo*, however, it is clear from the results presented here that there are no obstacles to such experiments. The feasibility of IPTS as an *in vivo* spectroscopic technique should be demonstrated in future experiments. An example would be the IPTS measurement of corneal tissue absorption in an anaesthetized animal model. In other work, the interferometer described in Chapter 2 should be implemented in optical fibers and employed to perform IPTS internally on an animal model.

The IPTS technique is now a new minimally-invasive alternative to estimating the effective absorption depth of a particular wavelength. Future work in this field could employ this IPTS technique as a minimally-invasive diagnostic. IPTS could be employed to estimate the concentration of an absorbing chemical species such as oxy-hemoglobin or a photosensitizer. IPTS can serve as an alternative to PPTR and fluorescence spectroscopy for "optical biopsy." IPTS may also be useful for NDE of engineering materials, particularly thin surface structures like these encountered in micro-electrical mechanical systems (MEMS) and integrated circuit (VLSI) technology.

Chapter 4
Pulsed Laser Driven Interphase Heat and Mass Transfer

4.1 Introduction

For our purposes, *interphase heat and mass transfer* is defined as heat or mass transfer that occurs as a result of a change of phase between a condensed substance (such as water or tissue) and a vapor substance (such as water vapor). Pulsed laser driven interphase heat and mass transfer is important since it may play a critical role during photothermal laser ablation of biological tissue. In such a situation the tissue may emit vapor upon rapid heating by a short pulsed laser and this emission may profoundly influence the temperature field in the irradiated tissue. Understanding this phenomenon may permit the derivation of models which accurately predict the threshold and dynamics of photothermal ablation as a function of the laser irradiation parameters and the tissue properties. Such predictive models for laser-tissue ablation could be used to develop new clinical applications for laser ablation as well as to optimize existing ones.

Interphase heat and mass transfer may occur in both *equilibrium* and *non-equilibrium* situations. During equilibrium interphase heat transfer, the amount of heat transferred from the condensed material to the vapor is equal to the amount of heat transferred from the vapor to the condensed material so that no net heat transfer occurs. During equilibrium mass transfer, an analogous balance for mass flux exists. By contrast, during non-equilibrium heat or mass transfer there is a net flow of heat or mass respectively between the two phases.

Non-equilibrium interphase heat and mass transfer may be subdivided into high rate and

low rate processes. Parabolic (diffusive) differential equations describe low rate interphase heat and mass transfer [47]. During high rate processes, heat and mass diffusion equations no longer apply due to discontinuities in thermodynamic properties. In general, it is very difficult to model high rate non-equilibrium interphase heat and mass transfer and so approximations and empirical correlations are often employed. In some cases, it is useful to derive theoretical upper limits on the maximum rates of heat and mass transfer which may then be used as approximate values for the true rates [25, 80].

Just as it is difficult to model high rate non-equilibrium interphase heat and mass fluxes, it is also difficult to measure them. Non-equilibrium thermal fields and mass concentrations tend to equilibrate over short time periods and thus high bandwidth and sensitivity are necessary for instruments designed to detect high rate non-equilibrium interphase heat and mass transfer.

Under some conditions, the interphase heat and mass transfer occurring at the exposed surface of a pulsed laser irradiated tissue may have a significant impact on the subsurface temperature field. In this way, the surface interphase heat and mass transfer may play a role in determining the threshold of laser ablation. Since soft biological tissue is primarily composed of water, results obtained for pure water systems may be applicable at least in part to soft biological tissue. The surface temperature of continuous wave (cw) laser irradiated tissue measured by a pyrometer has been shown to be affected by interphase heat and mass transfer [93].

In this chapter, we first present a theoretical discussion of high rate non-equilibrium heat and mass transfer. Following this we present and discuss some experimental results obtained for Q-sw Er:YSGG laser irradiation of pure water. The implications of high rate interphase heat and mass transfer for photothermal laser-tissue ablation are then discussed.

4.2 High Rate Interphase Heat and Mass Transfer

We begin our discussion by defining our system to be a pure substance (e.g. water)

present in two phases: a condensed phase (liquid or solid) occupying a half space in contact with a vapor phase occupying the other half space (see Figure 4.1). If we are concerned with net changes occurring as a result of interphase heat and mass transfer, then we are concerned with non-equilibrium heat and mass transfer. If the rates of heat and mass transfer are sufficiently low, there is a global non-equilibrium of the system but locally, on the molecular level, there is equilibrium. This state of affairs may be termed low-rate interphase heat and mass transfer. For this situation, diffusion and convection will control the rate of interphase heat and mass transfer and so both phases may be modeled as continuous materials, i.e. the discrete molecules comprising the phases need not be considered in the model. In the general case, the heat and mass transfer problems are coupled and the solution requires a numerical implementation of the governing parabolic partial differential equations.

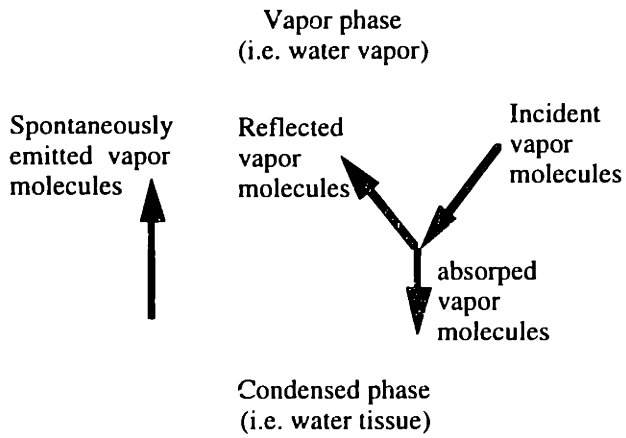

Figure 4.1: Illustration of two phase system

When the rates of interphase heat and mass transfer between the two phases are sufficiently large, there is a non-equilibrium on the molecular scale and a discontinuity in the thermodynamic properties (such as pressure and temperature) occurs at the interface. The region of the discontinuity is often termed a Knudsen layer in the literature and the discrete

molecules which comprise the phases must be explicitly modeled to successfully model the global system. This situation may also be termed free molecular flow since the rate of collisions between the molecules is insufficient to maintain equilibrium on the molecular scale. The kinetic theory of molecules, first developed in the nineteenth century by luminaries such as Maxwell and Boltzmann, is a useful model for high rate interphase heat and mass transfer. In kinetic theory, the individual molecules are modeled as ballistic particles obeying Newton's laws of motion. The rules governing individual molecular motions may be used to derive descriptions of the particle ensembles via the use of statistical mechanics [70, 97].

It is interesting and useful to ask the question (i) "what is the maximum rate at which mass may be transferred from the condensed phase to the vapor phase, or *vice versa*." This question has been posed and dealt with in a detailed monograph by R. W. Schrage [80]. A related question is (ii) "what is the maximum rate at which heat may be transferred from the condensed phase to the vapor phase, or *vice versa*." [25]. Question (i) may be of particular importance when using an interferometer to measure nanometer scale surface displacements resulting from pulsed laser irradiation of biological tissue since rapid heating of the tissue may result in detectable tissue vaporization. Question (ii) may be of particular importance since high rates of interphase heat transfer may influence the evolution of the thermal field in the tissue.

We can use kinetic theory to answer question (i). Consider a condensed phase in equilibrium with its vapor phase as depicted in Figure 4.1. To satisfy thermal equilibrium, the entire system is at a uniform temperature, T. The pressure of the vapor above the water will be P_{sat}, the saturation pressure of the substance at temperature T. Kinetic theory predicts the rate at which vapor phase molecules will collide with the surface of the condensed phase. Assuming ideal gas behavior of the vapor phase, this rate, $j_{v\to c}$, is given by [25, 80]:

$$j_{v\to c} = n_v \sqrt{\frac{RT}{2\pi}} \tag{4.1}$$

where n_v is the number density of vapor molecules, R is the ideal gas constant for the vapor, and T is the temperature of the vapor in Kelvins. Some fraction of the impinging vapor molecules may be absorbed by the condensed surface and the balance will be reflected. We

define σ to be the condensation coefficient and this is the fraction of impinging molecules which stick to the condensed phase, so consequently 1-σ molecules are reflected. While $\sigma \approx 1$ for water, surface contaminants can reduce this parameter [48, 49]. To preserve equilibrium

$$j_{c\to v} = \sigma j_{v\to c} \tag{4.2}$$

where $j_{c\to v}$ represents the rate at which condensed molecules are spontaneously emitted as vapor molecules.

If we consider a situation where all of the vapor molecules are instantaneously removed from the system of Figure 4.1 (thus creating a pure vacuum above the condensed material) then the condensed phase will vaporize at the spontaneous rate

$$j_{c\to v} = \sigma n_v \sqrt{\frac{RT}{2\pi}} \tag{4.3}$$

Thus, Eq. (4.3) represents the maximum rate at which the condensed phase can vaporize and is the rate at which the condensed substance will spontaneously evaporate into a pure vacuum. Of course, the vacuum will quickly become contaminated by the molecules emitted by the surface and so the evaporation rate predicted by Eq. (4.3) can only be maintained for very short periods of time. After a short time interval, enough vapor will accumulate above the condensed phase that some vapor molecules will be redirected back towards the surface of the condensed phase. Several efforts have been made to consider the situation where vaporized molecules are permitted to return to the surface [41, 80]. We shall not consider this case here since it is quite involved mathematically and because we are only interested in an upper limit for the mass flux from the condensed surface.

It is worth noting that Eq. (4.3) is also equal to the maximum rate of vapor condensation. This result illustrates the interesting symmetry between high rate vaporization and high rate condensation discussed in [25].

Eq. (4.3) represents the rate at which molecules are spontaneously emitted by the condensed phase into the vapor phase even in the case where another pure substance is present, i.e. a near ideal gas mixed with the vapor but insoluble in the condensed material. This second

gas will raise the total pressure exerted on the condensed material by virtue of Dalton's law for partial pressures, but it will not alter the spontaneous emission rate. This result comes about since the vapor pressure of most substances is not particularly dependent on the ambient pressure, and so the presence of other gaseous molecules does not interfere with the ongoing exchange between the vapor and condensed phases [80].

Armed with an upper limit for the rate at which mass may be vaporized from the condensed phase, we may now consider the maximum rate at which heat may be transferred from the condensed material. The latent enthalpy of vaporization h_{fg} is the energy required to convert a mass of condensed molecules to vapor molecules at a constant temperature. As such, it can be used to obtain the maximum interphase heat flux, q_{max}, between the condensed phase and the vapor phase.

$$q_{max} = \sigma m n_v h_{fg} \sqrt{\frac{RT}{2\pi}} \tag{4.4}$$

where m is the mass per molecule. This is the heat flux experienced at the surface of the condensed phase when it is permitted to vaporize into a vacuum. Providing the condensed phase molecules obey a velocity distribution identical to that under normal conditions, it is a rather rigorous upper limit on interphase heat transfer. Note that just as Eq. (4.3) represents the spontaneous rate at which molecules will be emitted by the condensed phase, even during equilibrium, Eq. (4.4) represents the spontaneous interphase heat flux that will occur, even during equilibrium. This heat flux is plotted against temperature for pure water in Figure 4.2. For water, $\sigma \approx 1$ and mn_v (which is equivalent to ρ_v, the saturated vapor density) was obtained from steam tables [48]. Note the extreme dependence on temperature, even over a limited temperature range.

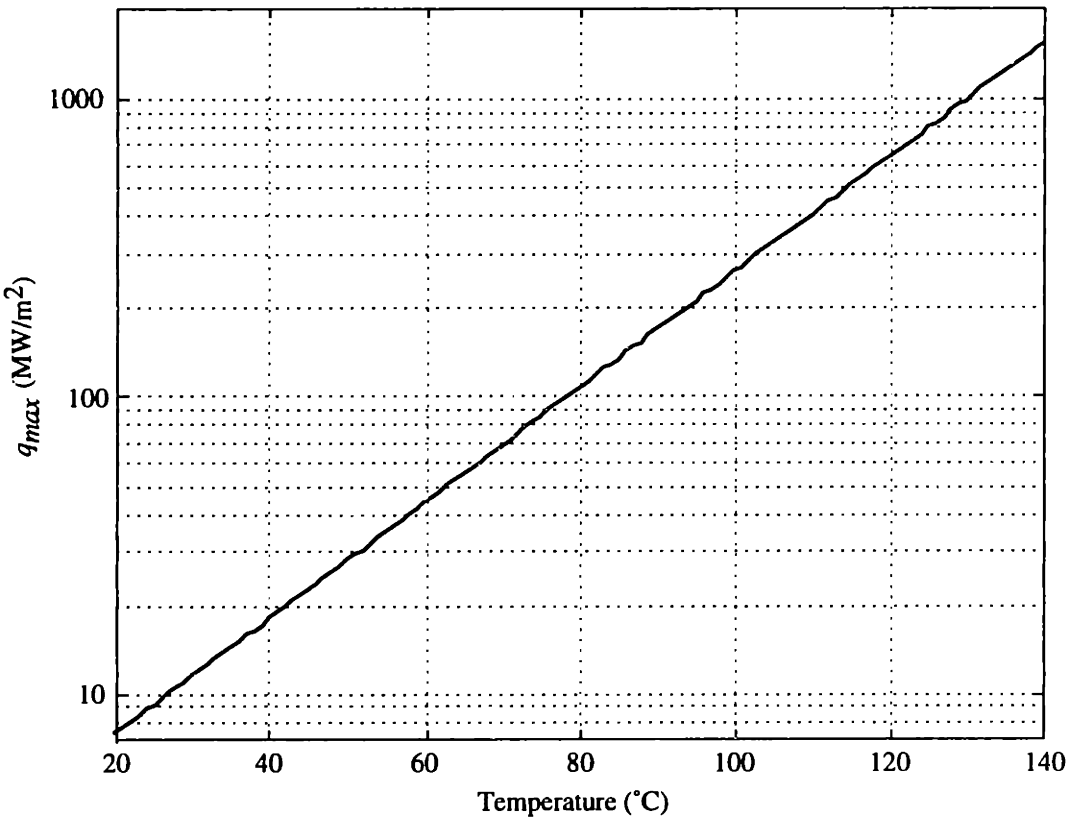

Figure 4.2: q_{max} for water (given by Eq. (4.4)) plotted against temperature

To illustrate the physical implications of the preceding discussion, consider the following situation where a high energy short duration laser pulse irradiates a pure water sample. Suppose that before the laser pulse occurs, the water is in equilibrium with vapor above it, the entire system is at ambient temperature (20° C), and that there is no air present - only water vapor above the condensed water. If so, then the ambient pressure must be only 2315 Pa (0.023 atm) since that is the saturation pressure of water at 20° C. If the laser pulse is sufficiently short and energetic, it will heat the condensed water and raise the surface temperature so that the spontaneous rate of molecular emission from the condensed water will greatly exceed the rate at which the ambient water vapor is colliding with and sticking to the surface. Thus, in addition to the global non-equilibrium in the temperature field there is local non-equilibrium at the interface so high-rate non-equilibrium interphase heat and mass transfer results.

For a sufficiently large temperature rise, Eq. (4.3) will be a rough approximation to the

net interphase mass flux (condensed phase to vapor) and Eq. (4.4) will be a rough approximation to the net interphase heat flux at the surface. After a short time the water vapor molecules will begin to accumulate above the tissue and they will be redirected towards the interface at a rate approaching the rate at which they are spontaneously emitted by the surface. Locally at the interface, equilibrium will be re-established (although there will still be non-equilibrium in the global temperature field) and once this occurs, the system will transition to a low-rate interphase heat and mass transfer where diffusion and convection adequately describe the evolution of the system. Eventually the entire system will come to a global thermal equilibrium.

Now imagine the same state of affairs except we include the standard atmosphere in the vapor space above the condensed water. When the condensed water is suddenly heated by the laser pulse, the surface temperature will suddenly increase as before and the spontaneous rate of molecular vaporization will be much higher than the rate at which water vapor molecules are colliding with and sticking to the surface. However, the standard atmosphere above the condensed surface will tend to redirect the spontaneously emitted water molecules back towards the surface, thus reestablishing local equilibrium at the interface much faster than in the preceding case. Consequently, the net rate of interphase heat and mass transfer will be much lower in this case than in the preceding case and Eq. (4.4) will not be a good description.

On the other hand, consider what would happen if the laser pulse contains enough energy to heat the surface of the condensed water to well over 100° C. The vapor pressure of the water will exceed the ambient pressure and a shock wave will result. The water vapor will be spontaneously emitted by the condensed water surface at a rate and a velocity that will overwhelm the standard atmosphere above it which will be pushed out of the way (P_{sat} at 130° C is 2.7 atm > 1 atm ambient pressure). Consequently, Eq. (4.3) will be an approximate description of the interphase mass transfer and Eq. (4.4) will be an approximate description of the interphase heat transfer.

The temperature field in the irradiated condensed material may be profoundly affected by

high rate interphase heat and mass transfer. As discussed above, in some cases the laser pulse may contain enough energy to create a heat flux at the surface that is approximated by Eq. (4.4). We will now formally pose the problem subject to those assumptions. The temperature field in the condensed material will be determined by

$$\rho_c c_{p,c} \frac{\partial T}{\partial t} = k_c \frac{\partial^2 T}{\partial z^2} + q'''_{laser} \tag{4.5}$$

where k_c is the thermal conductivity of the condensed material, t is time, T is the temperature of the condensed phase, z is the depth below the surface, ρ_c is the density of the condensed phase, $c_{p,c}$ is the heat capacity of the condensed phase, and q'''_{laser} is the volumetric heating of the laser pulse (a function of z and t). This formulation assumes that the penetration depth of the irradiating laser is much smaller than the transverse width of the laser beam so that the resulting temperature field is one dimensional (a function of z only). The initial condition for the system is that the condensed phase is entirely at ambient temperature. The surface boundary condition is given by Eq. (4.4), in other words

$$k_c \frac{\partial T}{\partial z}\bigg|_{z=0} = \rho_v h_{fg} \sqrt{\frac{RT(z=0,t)}{2\pi}} \tag{4.6}$$

If the surface vaporization rate is sufficiently high, we must consider the effect of the moving boundary on the temperature field. For the moving boundary to be negligible, we require that the heat conduction velocity in the condensed phase, v_{cond}, be much greater than the velocity of the boundary due to vaporization, v_{vap}. The heat conduction velocity in the condensed phase may be expressed as

$$v_{cond} = \sqrt{\frac{\alpha_c}{t}} \tag{4.7}$$

where α_c is the thermal diffusivity of the condensed phase. The velocity of the boundary due to vaporization may be expressed as

$$v_{vap} = \frac{m j_{c \to v}}{\rho_c} = \frac{q_{max}}{\rho_c h_{fg}} \tag{4.8}$$

v_{cond} clearly decreases as time increases so if we assume that v_{vap} takes on a large constant value

then we expect that v_{cond} will exceed v_{vap} for only a short time interval. We equate v_{cond} and v_{vap} to find t for which $v_{cond}>>v_{vap}$:

$$t << \frac{\alpha_c \rho_c^2 h_{fs}^2}{q_{max}^2} = \alpha_c \left(\frac{\rho_c}{\rho_v}\right)^2 \frac{2\pi}{RT} \tag{4.9}$$

From Figure 4.2 we see that the maximum value for q_{max} for water is about 1000 MW/m^2 if the surface temperature is limited to 140° C. Consequently we conclude that the moving boundary will not affect the temperature field for t<<800 ns. This assumes that we are maintaining q_{max} at 1000 MW/m^2. In reality, the numerical solution indicates that high values of q_{max} are only realized for short periods of time so that the solution is valid for much larger values of t.

Due to the non-linear nature of the boundary condition in Eq. (4.6), there is no analytical solution available and so numerical methods of solution are required. Thus Eq. (4.5) was solved subject to the boundary condition of Eq. (4.6) by using the finite element method in z and the Runge-Kutta numerical technique in t. Sample temperature fields for pure water at various points in time exposed to a laser pulse with a FWHM duration (τ_p) of 50 ns, a fluence (ϕ_0) of 1000 J/m^2, and a penetration depth (D) of 1.94 μm are depicted in Figure 4.3. These parameters roughly correspond to a Q-sw Er:YSGG laser pulse near the ablation threshold of water. Note that the exponential deposition profile of the laser pulse energy is rapidly distorted by the surface flux and that a subsurface temperature peak is created. At approximately 300 ns after the start of the laser pulse, the surface temperature has decayed to be well below 100° C while there is more than 10° of superheat at a depth 200 nm below the surface. Thus, high rate interphase heat and mass transfer may provide a mechanism for generating subsurface temperature maxima. This issue and its implications for laser ablation of biological tissue are discussed in Section 4.4.

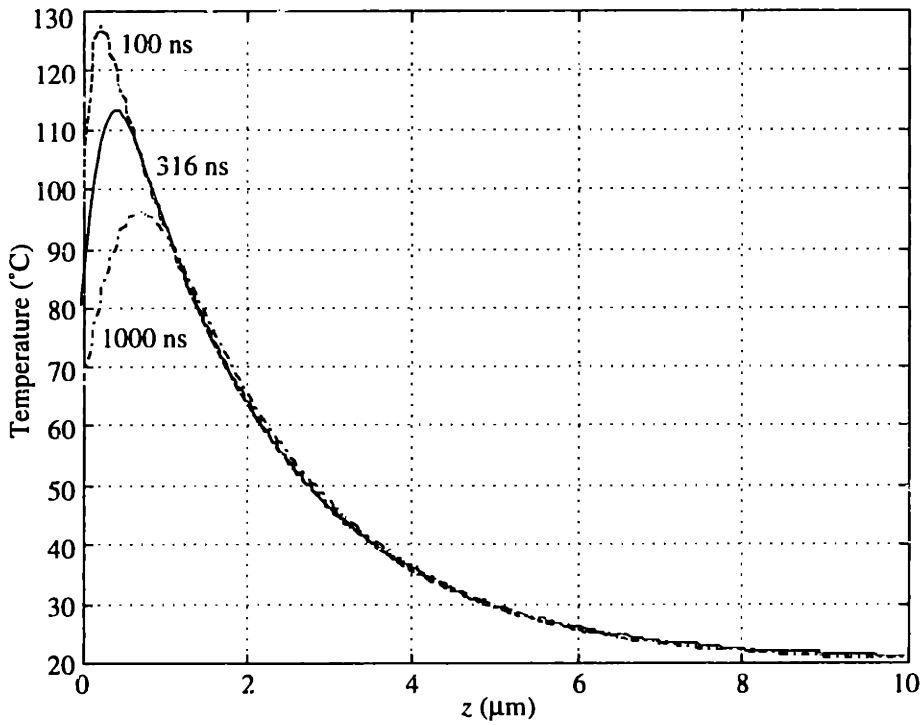

Figure 4.3: Predicted temperature fields at various times for pure water assuming a surface flux obeying Eq. (4.4) exposed to a laser pulse with a τ_p=50 ns, ϕ_0=1000 J/m^2, D=1.94 μm (μ_a=515,000 1/m). (The wrinkles in the 100 ns trace are artifacts of the printing process.)

Temperature time histories at various depths for the same conditions as Figure 4.3 are presented in Figure 4.4. Once again, the evolution of a high degree of superheat approximately 200 nm below the surface is apparent. Note that the surface heat flux boundary condition ensures that the surface temperature of the condensed material is always slightly cooler than the temperature at points just below the surface.

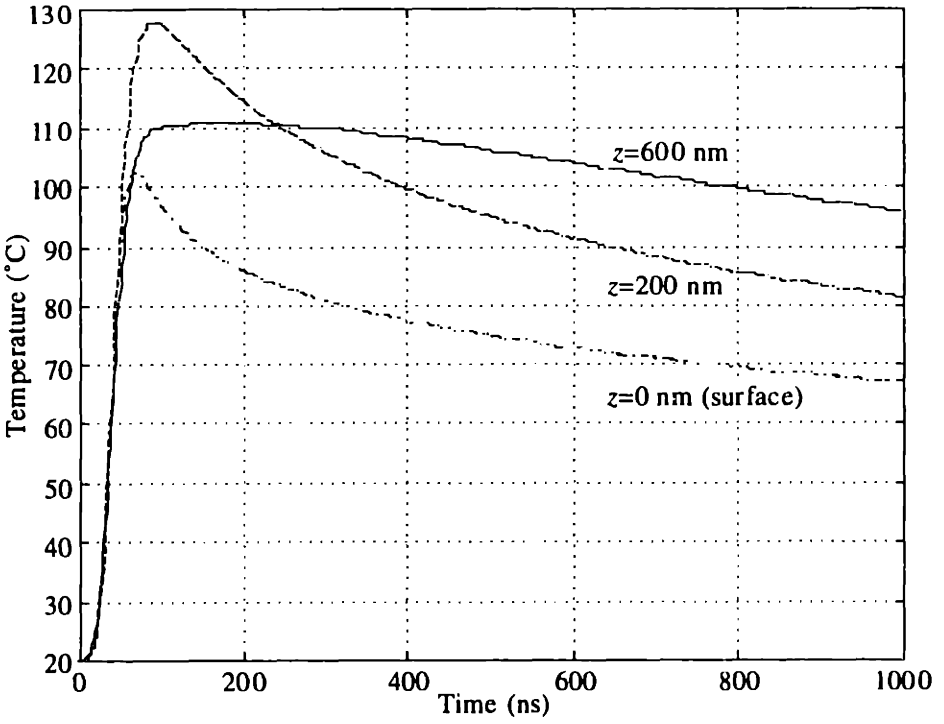

Figure 4.4: Predicted temperature histories at various z for pure water assuming a surface flux obeying Eq. (4.4) exposed to a laser pulse with a τ_p=50 ns, ϕ=1000 J/m^2, D=1.94 μm (μ_a=515,000 1/m)

The numerical solution for the temperature field can be used to predict the surface displacement of a liquid sample experiencing high rate interphase heat and mass transfer. The surface displacement in this case is quite different from that occurring for the conditions discussed in Chapter 3 and detailed in Eq. (3.3). The surface displacement is not only a function of the amount of thermal expansion below the surface, but is also a function of the amount of material vaporized off the surface of the condensed liquid. Additionally, the vaporizing material exerts a recoil force on the condensed liquid which compresses it and causes further downward surface motion. Consequently, the surface displacement, Δz, may be expressed as (see Appendix A):

$$\Delta z(t) = \int_0^\infty \left(\frac{\rho_{c,0}}{\rho_c(T(z,t))} - 1 \right) dz - \int_0^t \frac{q_{max}}{\rho_c h_{fg}} dt + \int_0^\infty \varepsilon_{recoil} dz \tag{4.10}$$

where ρ_c is the density of the condensed liquid (denoted by $\rho_{c,0}$ at ambient temperature) and ε_{recoil} is the strain resulting from material vaporizing off the interface. Note that according to our convention, compressive strain is negative so that recoil compression of the liquid will result in

a downward surface displacement as expected. The first term in Eq. (4.10) is identical to Eq. (3.3), the second term refers to surface displacement resulting from mass removal at the interface, and the final term refers to surface displacement resulting from the compression of the condensed liquid by the recoil force.

Assuming linear elastic behavior in the liquid and a hydrostatic state of stress, the recoil strain in the z direction will be proportional to the recoil stress, σ_{recoil}, via the bulk modulus, K_b (see Appendix A):

$$\varepsilon_{recoil}(z,t) = \frac{\sigma_{recoil}(z,t)}{K_b} \tag{4.11}$$

The recoil stress created at the surface is assumed to propagate into the liquid at the sonic velocity:

$$\sigma_{recoil}(z,t) = \sigma_{recoil}\left(z=0, t-\frac{z}{c_a}\right) \tag{4.12}$$

The recoil stress at the surface, $\sigma_{recoil}(z=0,t)$ is equal to the vaporization rate (by mass) multiplied by the average velocity of the vaporized molecules normal to the surface (a minus sign is included to preserve our convention that compressive stresses and strains are negative):

$$\sigma_{recoil}(z=0,t) = -mj_{c\to v}\frac{\bar{c}}{4} = -\frac{q_{max}}{h_{fg}}\frac{\bar{c}}{4} \tag{4.13}$$

where $\frac{\bar{c}}{4}$ is the average velocity of the vaporized molecules away from the surface and is given by [80]:

$$\frac{\bar{c}}{4} = \sqrt{\frac{RT_s}{2\pi}} \tag{4.14}$$

where T_s is the temperature of the surface (in Kelvins) and is a function of time only. Eqs. (4.11-14) can be combined to yield:

$$\varepsilon_{recoil}(z,t) = -\frac{\rho_v R}{2\pi K_b} T_s\left(t-\frac{z}{c_a}\right) \tag{4.15}$$

The bulk modulus for water is large ($K_{b,water}$=2.2×10^9 N/m^2 [109]) so compression due to vapor recoil momentum causes at most 5 nm of surface motion.

Providing the dependence of ρ_c on temperature is explicitly available and Eq. (4.9) is

satisfied, we can use the numerically calculated temperature fields in conjunction with Eq. (4.10) to predict the surface displacement Δz. The predicted surface displacement obtained in this manner for the same conditions as Figures 4.3 and 4.4 is depicted in Figure 4.5. The calculation revealed that about 10 nm of material was vaporized during the first 100 ns (i.e. during the laser pulse). Thus the effect of the high rate interphase mass transfer is significant even during the laser pulse. Most of the downward surface motion after 100 ns is due to material removal (second term of Eq. (4.10)) rather than thermal contraction (first term of Eq. (4.10)) or material compression (third term of Eq. (4.10)).

Note that water vapor emitted during the laser pulse will not block the incident laser radiation since the absorption properties of water vapor in the IR are much weaker than they are in the condensed state [104]. Moreover, even if water vapor absorbed the laser energy as strongly as condensed water does on a mass basis, the 10 nm of condensed water blown off during the pulse would have a negligible effect on the incident fluence since the effective penetration depth (~2.1 μm) is so much larger.

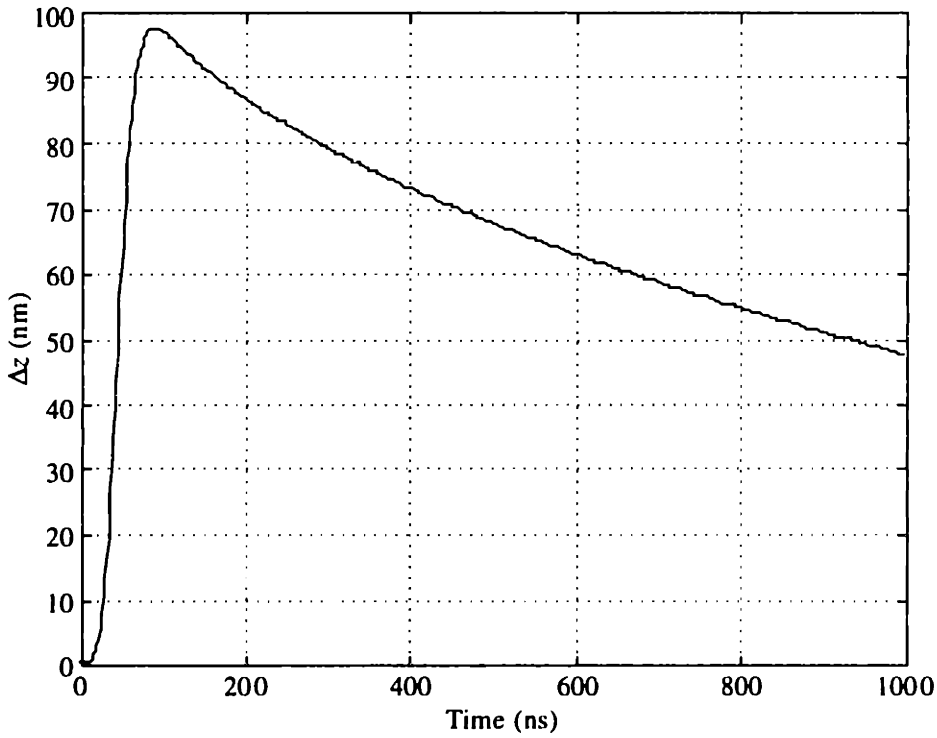

Figure 4.5: Δz predicted for Q-sw Er:YSGG irradiation of water assuming a surface flux obeying Eq. (4.4) with ϕ_0=1000 J/m^2 and μ_a=515,000 1/m

4.3 Interphase Heat and Mass Transfer During Q-sw Er:YSGG Irradiation of Water

To assess the significance of interphase heat and mass transfer during laser irradiation of biological tissue, the surface displacement of pure water samples exposed to Q-sw Er:YSGG laser radiation was measured with the interferometer system described in Chapter 2. The experiments were performed on pure water since it is a pure substance with well tabulated thermodynamic properties. Since soft tissue is primarily water, the results obtained for water may be applicable to tissue.

The experimental setup was similar to that employed for the IPTS technique in the preceding chapter, only there was no physical barrier impeding the interphase heat and mass transfer. Two different experimental configurations were employed: interferometric

measurement from the top (air) side of the air-water interface (Figure 4.6) and interferometric measurement of from the bottom (water) side of the air-water interface (Figure 4.7). When performing top side interferometric measurements of the interface displacement the Q-sw Er:YSGG pump beam was inclined at 14° to permit both the pump and HeNe interferometer probe to access the target. This results in a small difference (factor of ~0.98) in the effective Er:YSGG absorption depth between the two configurations.

The data obtained for the two experimental configurations were nearly identical thus indicating that the HeNe interferometer probe beam was not significantly perturbed when traversing vaporized water or stress waves inside the condensed water. This fact is not surprising since with the aid of tabulated water and air properties, one can show that the optical path of the HeNe probe is not much affected by bipolar density variations in condensed materials (due to a bipolar stress wave) or by small amounts of water vapor in the air above.

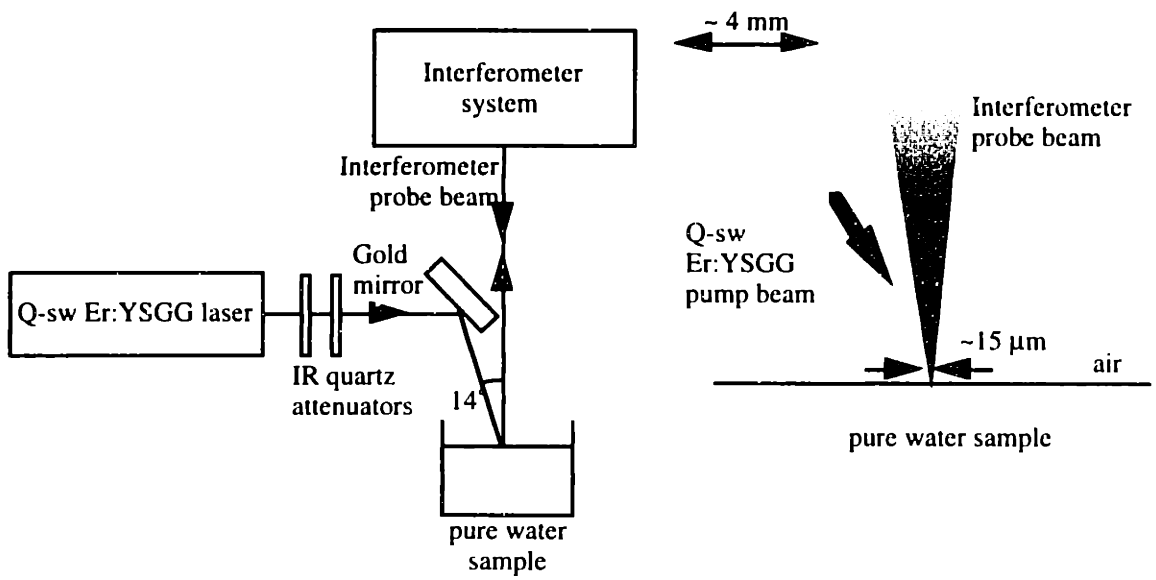

General schematic Closeup view (not to scale)

Figure 4.6: Diagram of experimental apparatus used for top-side interferometric displacement measurement of water exposed to Q-sw Er:YSGG laser radiation

The water used for the experiments was triple distilled deionized water. The Er:YSGG

laser was identical to the one used for the experiments in the preceding chapter; it produced 50 ns FWHM laser pulses about 4 mm in diameter with about 25 mJ of energy at about 1 Hz. IR quartz attenuators were used to approximately control the energy in the laser pulse. The mechanical Q-switching element caused the mode shape and the pulse energy of the laser to vary on a shot to shot basis and so measurement of the local radiant exposure was impossible.

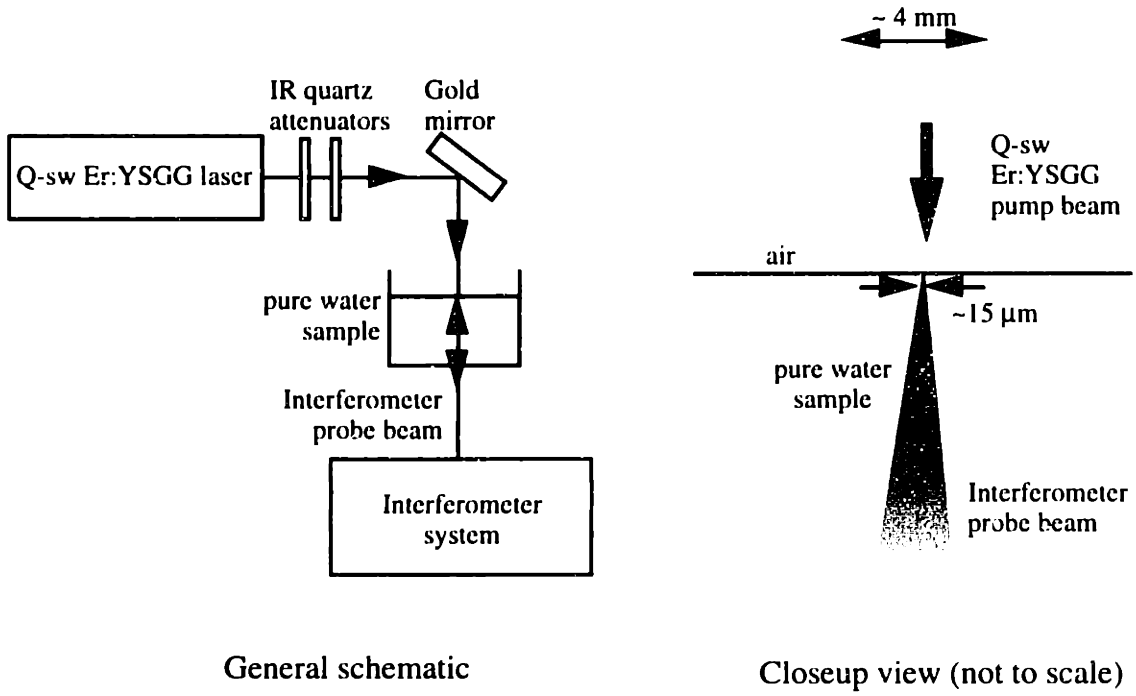

Figure 4.7: Diagram of experimental apparatus used for top-side interferometric displacement measurement of water exposed to Q-sw Er:YSGG laser radiation

The Q-sw Er:YSGG laser pulse was thermally confined but not mechanically confined, which were the same conditions occurring during the IPTS experiments detailed in Chapter 3. The acoustic impedance of air (~393 kg/m^2s) is much lower than that of pure water (~1.5×10^6 kg/m^2s) so that the air did not impede the thermal expansion of the water.

Typical data traces obtained for both experimental configurations are presented in Figure 4.8 (compare to Figure 3.10). The timescale of the initial upward displacement corresponds to the timescale of energy deposition which is to be expected. The mid-IR pump laser energy is completely thermalized as soon as it is introduced into the target water. The degree of

downward surface motion depends on the amount of initial surface expansion. Almost no downward surface motion occurs after an initial expansion of less than 40 nm, however, the downward surface motion occurring after an initial upward surface motion greater than 100 nm is quite pronounced. The transition between the two cases apparently occurs for an initial surface expansion of 60 nm which corresponds to an approximate initial surface temperature of 100° C. This agrees with the ideas put forth in the previous section, where it was argued that high rate interphase heat and mass transfer can only occur when the surface temperature is raised above 100° C, and the resulting vapor is capable of pushing the atmosphere out of the way.

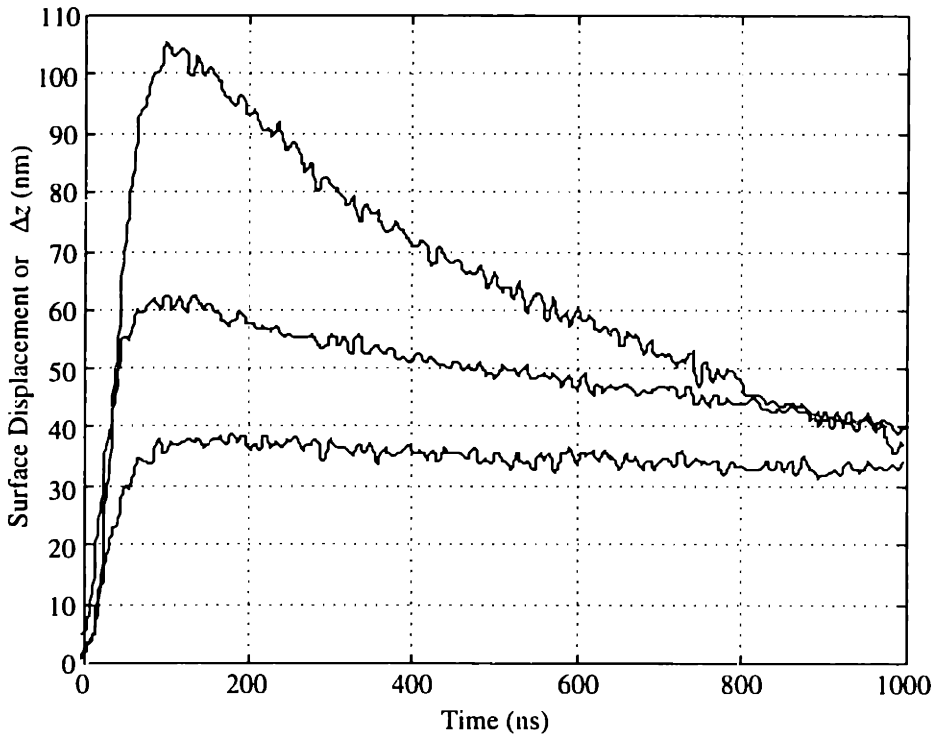

Figure 4.8: Typical data traces obtained by the interferometer during Q-sw Er:YSGG laser irradiation of pure water (compare to Figure 3.10)

In Figure 4.9 a typical surface displacement from Figure 4.8 is compared with the surface displacement of a saran covered water sample (obtained from the IPTS experiments in Chapter 3). The initial motions of the two traces (from 0 to 100 ns) are nearly identical. At about 100 ns, the uncovered sample begins a rapid downward motion indicative of intense

surface vaporization and cooling. The difference between the covered and uncovered data traces is striking.

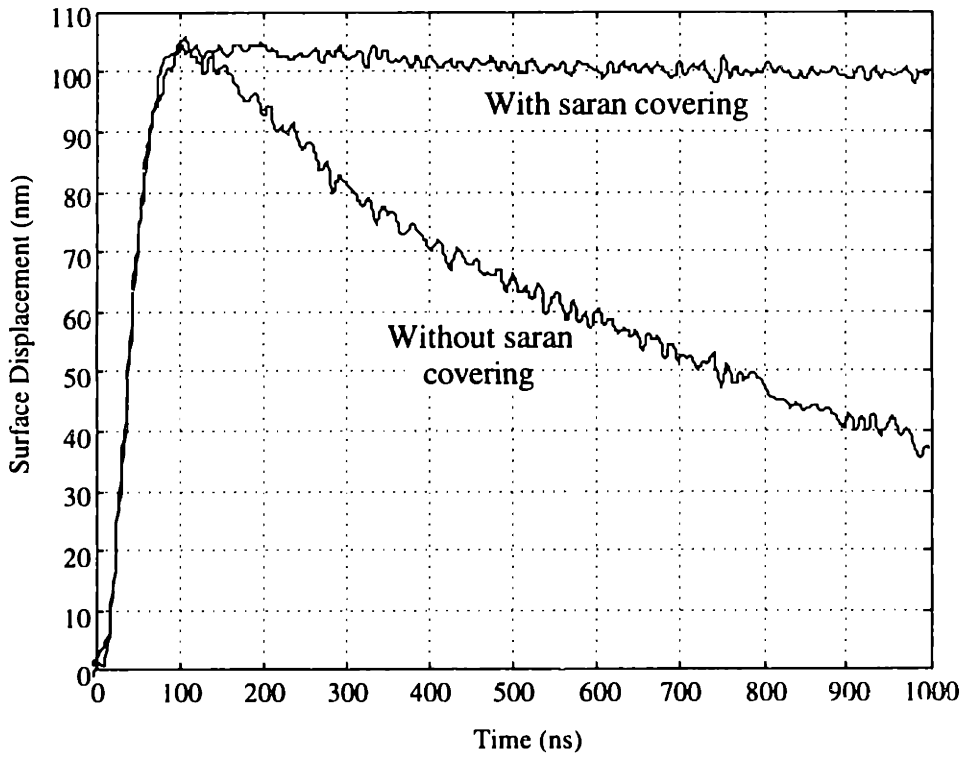

Figure 4.9: Comparison of surface displacement of uncovered and saran covered water exposed to Q-sw Er:YSGG laser pulse

The data traces were compared to the model presented in the previous section by fitting the initial surface expansion. A comparison between typical data and the corresponding fitted models is depicted in Figure 4.10. The fluences indicated in the plot are the fluences used in the model to fit the initial surface expansion of the data. As the figure clearly shows, for smaller initial surface displacements (<~60 nm), the model tends to overpredict the downward surface motion of the data. For larger initial surface displacements (>~100 nm) the model tends to underpredict the downward surface motion. For intermediate initial surface displacements (~80 nm), there is good agreement between the model and the data. For comparison purposes, the maximum surface temperatures predicted by the model are 105° C, 97° C, and 70° C for the 1060 J/m^2, 890 J/m^2, and 500 J/m^2 traces respectively. One can use these surface temperatures

in Eq. (4.4) to determine the maximum predicted surface heat flux.

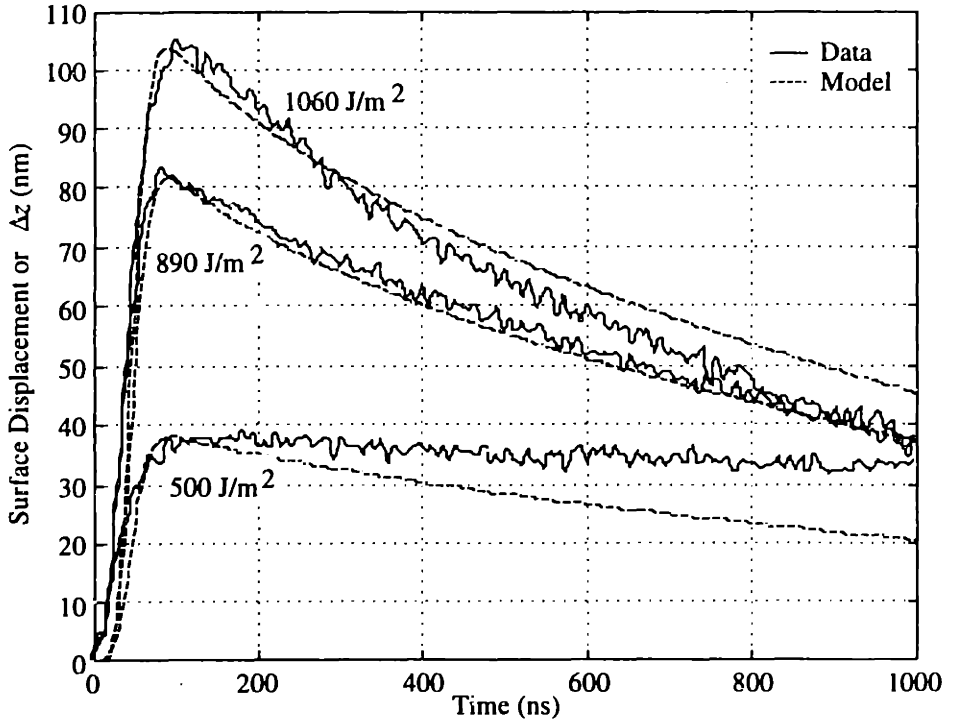

Figure 4.10: Comparison between data and model based on Eq. (4.10) for Q-sw Er:YSGG laser irradiation of pure water

The fact that the high rate interphase heat and mass transfer model overpredicts the downward surface motion for small initial surface displacements is not surprising. Smaller initial surface displacements correspond to lower initial surface temperatures which do not yield sufficiently high spontaneous vapor emission to push the atmosphere out of the way. What is most surprising is that at very high initial surface displacements (<100 nm) which correspond to maximum surface temperatures of approximately 105° C the high rate interphase heat and mass transfer model *underpredicts* the downward surface motion. The implication is that material is blown off the surface at a rate which exceeds the theoretical upper limit predicted by kinetic theory!

It is highly unlikely that the interferometer is producing this effect as an instrument artifact since consistent results were obtained for measurements made from the top (air) and bottom (water) side of the interface. Moreover, the downward surface motion behavior was quite consistent given the initial surface displacement so shot to shot laser mode shape

anomalies are not implicated as the cause. Bulk flow cannot be responsible since during the first microsecond following irradiation, stress waves traveling at the sonic velocity (1500 m/s) can only travel 1.5 mm. This is less than both the radius of the irradiated region (~ 2 mm) and the depth of the water sample (~5 mm), consequently the inertia of water below and surrounding the irradiated region precludes significant motion during the first microsecond.

One possible explanation for the discrepancy is that the vapor was modeled as an ideal monatomic gas. In reality water molecules have significant rotational and vibrational energy storage modes. These extra modes may result in higher non-equilibrium interphase heat or mass fluxes. Perhaps surface contamination of the water samples is somehow responsible, although there does not seem to be mechanism how surface contaminants can produce *enhanced* levels of pulsed interphase heat and mass transfer. We do not expect that dissolved atmospheric gasses in the water will affect the surface displacement since their concentrations are low. It may be that during high rate interphase heat and mass transfer, h_{fg} is not a good measure of the specific vaporization energy.

Considering that no researchers have ever experimentally verified the limiting rates for interphase heat and mass transfer predicted by the theory, it is possible that the theory is not a good description of the underlying physical phenomena. For example, the theory assumes that the velocity distributions of the molecules obey the canonical Maxwell-Boltzmann distribution, but in fact this may not be the case. The findings presented here must be independently corroborated and the associated theory may need to be reassessed.

4.4 Implications for Pulsed Laser Ablation Thresholds

The results of the preceding section may have significant implications for laser ablation of biological tissue. Soft biological tissue is primarily water and its behavior in response to pulsed laser irradiation can often be modeled by that of water. High rate interphase heat and mass transfer may provide a heat sink at the tissue surface that contributes to the formation of a

subsurface temperature maximum. Many researchers have pointed out that the ablation dynamics for certain combinations of wavelength, pulse duration, and tissue type are consistent with explosive boiling [13, 94, 96, 102, 104] which could result from such a subsurface temperature maximum. Moreover, many researchers have found that the ablation threshold for certain combinations of wavelength, pulse duration, and tissue type corresponds to surface temperatures well above 100° C, if the tissue surface is assumed to be adiabatic [94, 96]. These calculations suggest that boiling of the tissue water should commence at the surface of the tissue rather than in the bulk, since that is where the maximum superheat is expected to occur. It is clear that interphase heat and mass transfer will serve to quench the surface temperature maximum, thus producing a subsurface temperature maximum.

Figures 4.3-5 were created assuming conditions similar to those existing during Q-sw Er:YSGG laser irradiation of water. In response to a 1000 J/m^2 laser pulse incident on water, over 20° of superheat could be produced about 200 nm below the surface at about 300 ns after the laser pulse. The threshold for ablation during Q-sw Er:YSGG laser ablation of tissue may occur when the laser pulse energy produces enough subsurface superheat to nucleate a bubble that intercepts the tissue surface and spews out it contents. The time delay between the start of the laser pulse and the onset of ablation has been estimated to be several hundred nanoseconds [94, 96], which would correspond to the time required for heat and mass transfer at the surface to establish a significant subsurface temperature peak. At this time, such a mechanism for Q-sw Er:YSGG laser ablation of water based tissue is purely speculative, and until better measurements of the interphase heat and mass transfer are performed, no conclusions can be drawn as to the mechanism controlling the ablation threshold.

Previous researchers have advanced thermal models for ablation which predict the existence of a subsurface temperature maximum that implies subsurface vapor nucleation and explosive boiling. Dabby and Paek developed a simple model for the temperature field of a target exposed to an intense laser which assumed that the target surface temperature could not exceed the target substance vaporization temperature [14]. This boundary condition is

equivalent to forcing the interphase heat and mass flux to be zero for surface temperatures below the vaporization temperature and infinite when the surface temperature attempts to exceed the vaporization temperature. However, this model was criticized for its simplistic treatment of interphase heat and mass transfer [37, 51]. Miotello and Kelly have advanced a model for the temperature field in a laser irradiated target which includes a kinetic theory treatment of the interphase heat and mass transfer similar to that presented here [37, 51]. They found that the subsurface temperature maximum resulting from surface cooling was not significant and hence probably did not influence laser ablation of aluminum. The difference between their result and that presented here is due to the difference between the material properties of water and aluminum. Furthermore, in contrast to aluminum, only 10° of subsurface superheat in a water target near 100° C might be sufficient to incite subsurface bubble nucleation and hence ablation.

Recent work has advanced the notion that a subsurface temperature maximum is not necessary for the production of subsurface bubble nucleation and explosive material removal [37, 51, 96]. If the timescale of the laser pulse is fast enough, and if the laser pulse contains enough energy, the water in the tissue target may be driven close to the spinodal temperature (~305° C at 1 atm) which is the temperature at which a liquid will homogeneously nucleate and thermally explode. The threshold for Q-sw Er:YSGG ablation of water based tissues may not correspond to the production of such high temperatures however.

The thermal modeling presented in this thesis suggests that the influence of interphase heat and mass transfer increases when the penetration depth is reduced. Thus, if interphase heat and mass transfer play a role in determining the threshold for Q-sw Er:YSGG laser ablation of tissue, then it is likely that the same can be said for ArF excimer laser irradiation of cornea whose penetration depth was measured to be about one quarter the value of that for Q-sw Er:YSGG laser irradiation of water. Moreover, recent work has demonstrated that the stress transients produced during ArF excimer laser ablation of dermis are consistent with a gas dynamic model for rapid surface vaporization [94, 95]. It may be that high rate interphase mass transfer *is* the actual ablation event producing the stress transients published in [88, 94, 95].

To further investigate these issues, the interferometer system described in Chapter 2 was employed to measure the surface motion of bovine corneal stroma in response to ArF excimer laser irradiation. The experimental setup and laser parameters were identical to that depicted in Figures 3.12-3 except that a glass membrane was not employed to suppress interphase heat and mass transfer. As in the previous chapter, the laser pulse energy was thermally confined but not mechanically confined. Typical traces are presented in Figure 4.11. The fluence values listed in the figures are only approximate values since it is hard to obtain an exact representation of the beam transverse profile. Note that at low fluences, there is very little downward surface motion following the initial expansion as compared to higher fluences where the downward surface motion following the initial surface expansion was pronounced. Note also that all of the traces require on the order of 100 ns to reach their peak level of displacement but the ArF excimer laser pulse required only 50 ns to deposit all of its energy. This result is identical to that discussed in the preceding chapter for ArF excimer laser irradiation of glass covered bovine cornea. The delayed expansion may be due to the time required for thermal energy to be transferred from the corneal proteins to the free water or a photochemical pathway for energy deposition.

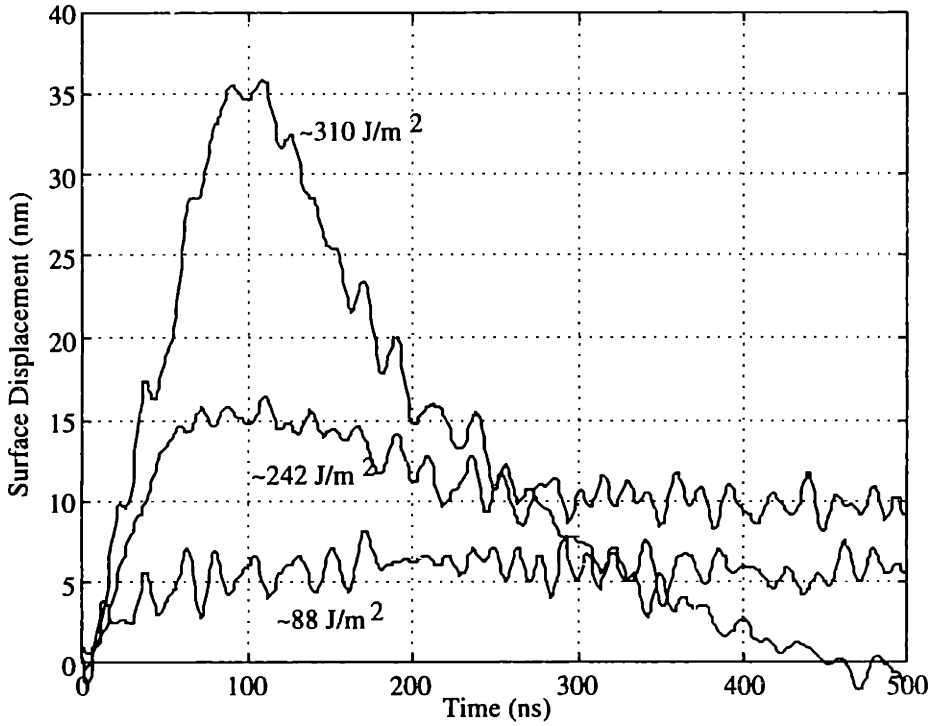

Figure 4.11: Typical displacement traces obtained for ArF excimer laser irradiation of bovine corneal stroma in air

In Figure 4.12 a typical data trace obtained for ArF excimer laser irradiation of bovine corneal stroma in air is compared to the predictions of the theoretical model incorporating the high rate interphase heat transfer boundary condition (Eq. (4.4)). The effective absorption depth used in the model was the value experimentally measured by the IPTS technique in the previous chapter (D=515 nm). The most significant discrepancy between the model and the data is the different timescales required for the initial expansion. The model fully expands once the laser pulse has ceased since it assumes instantaneous thermalization of the pulse energy solely in the tissue water. The model does not account for the possibility that there is a delay in the transfer of thermal energy from the absorbing proteins to the free water. Photochemical activity of the proteins may also account for why there is a delay in the thermalization of the energy. In addition to its delayed rate of expansion, the maximum expansion of the experimental trace is about midway between that predicted by the model for ϕ_0=350 J/m^2 and ϕ_0=450 J/m^2 but its fluence was measured to be ~310 J/m^2. This particular discrepancy may be due entirely to inaccuracies in measurements of the transverse beam width or it may be

indicative of a more fundamental difference between the model and the data.

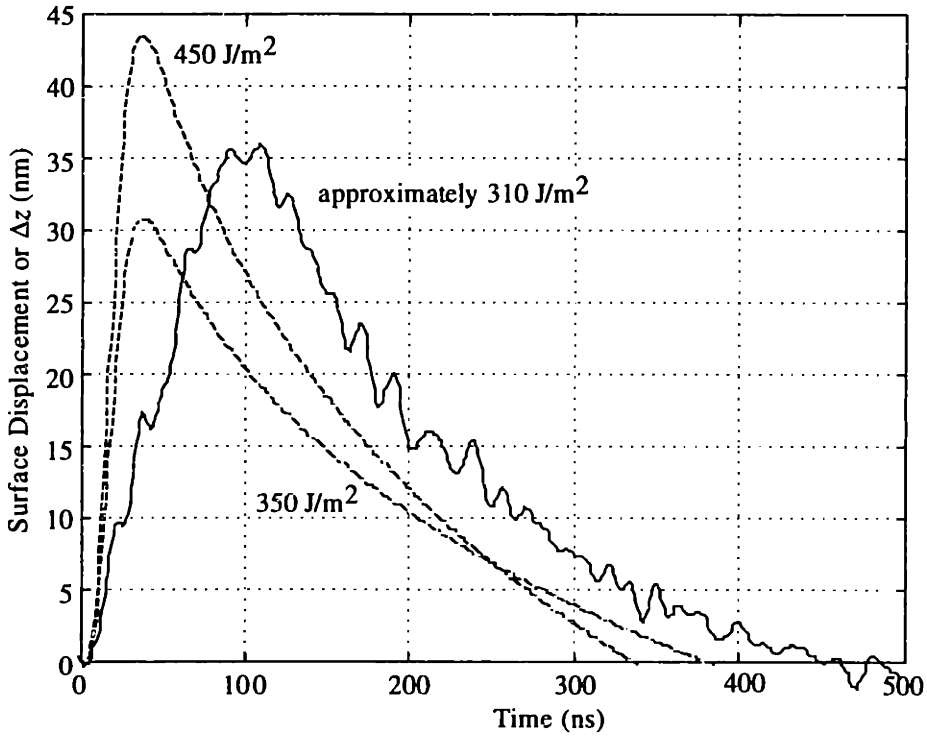

Figure 4.12: Comparison between data obtained from ArF excimer laser irradiation of cornea and theoretical model incorporating high rate interphase heat and mass transfer

Despite the discrepancy in the timescale for the initial expansion, the rate of downward surface motion is roughly consistent with the model. This result supports the notion that high rate interphase heat and mass transfer occurs during ArF excimer laser irradiation of corneal tissue at high radiant exposures. Whether or not the model for interphase heat and mass transfer presented here is correct, the rate of downward surface motion approaches 0.2 m/s in Figure 4.12 which corresponds to a vaporization rate of 200 kg/m^{2}s!

It must also be pointed out that the simulation was performed for a pure water sample while the data was obtained on bovine corneal stroma exposed to air. Cornea is about 80% water by mass and most researchers use the thermophysical properties of water to describe corneal tissue [21, 82]. Nevertheless, proteins such as collagen and other substances in the cornea may cause the thermophysical properties of corneal tissue to differ substantially from

those of water, especially for corneal tissue that is exposed to air and may undergo a degree of desiccation. The collagen in the cornea is the primary absorber of the 193 nm ArF excimer laser radiation and so it may be heated to temperatures at which it experiences significant structural changes.

4.5 Conclusions

Interphase heat and mass transfer may have an impact on the dynamics of laser ablation of biological tissue. For very intense, short duration laser pulses, a local non-equilibrium in both the thermal field and the water vapor concentration field may lead to high rate interphase heat and mass transfer where the net vaporization rate approaches the theoretical maximum predicted by kinetic theory. The choice of chromophore, whether it is the tissue water or the structural proteins, may determine the kinetics and transport phenomena.

Numerical simulations of the surface displacement were computed for pulsed laser irradiation of pure water assuming that vaporization proceeds at the maximum rate allowed by kinetic theory. When compared to these simulations, the data suggests that at high fluences, interphase heat and mass transfer occurs at rates matching and exceeding the limits predicted by kinetic theory during Q-sw Er:YSGG laser irradiation of water and ArF excimer laser irradiation of corneal stroma. Independent confirmation of such high rates of interphase heat and mass transfer is clearly necessary. The roles played by surface contaminants on the water samples and proteins present in the corneal tissue must be investigated as they may contribute to the unusual surface displacement of the interface when irradiated by high energy short duration laser pulses.

The simple kinetic theory model described here may not capture the full complexity of the physics governing pulsed laser driven heat and mass transfer. More sophisticated models and numerical simulations are necessary. As the computational power available for numerical simulations increases due to technological advances, simulations of molecular dynamics could

provide insight into how interphase heat and mass transfer proceeds for a system experiencing extreme local non-equilibrium. Such simulations could account for internal degrees of freedom as well as molecular systems whose velocity profiles undergo severe departures from the Maxwell-Boltzmann velocity distributions, as may be the case during intense pulsed laser irradiation.

Chapter 5
Conclusions and Future Work

5.1 Achievements of This Thesis

Photothermal effects resulting from pulsed laser irradiation of biological tissue remains an important and fertile field for research. It requires an interdisciplinary approach since it lies at the nexus of medicine, biology, physics, and engineering. The results of this and other research efforts may lead to new clinical procedures, a better understanding and optimization of existing ones, and often a better understanding of the basic underlying physics.

In this thesis we have employed novel instrumentation and modeling to investigate the photothermal effects of pulsed laser irradiation of biological tissue. The results presented here are relevant to both laser diagnostics (IPTS) and laser therapeutics (ablation). The particular achievements of this thesis are organized into the three sub-sections to follow: improved instrumentation, the development of the IPTS technique, and progress in pulsed laser driven interphase heat and mass transfer.

5.1.1 Improved Instrumentation

We have developed an improved interferometer for monitoring the surface displacement of tissue exposed to pulsed laser irradiation. This interferometer builds on previous efforts to employ interferometry for the analysis of laser-tissue interactions [2, 4, 33]. Our interferometer can achieve a 4 nanosecond rise time with single nanometer spatial resolution and can be used to track the displacement of both specular and diffuse surfaces. The high bandwidth and sensitivity of this device make it an ideal tool to study photothermal laser effects in a time-

resolved manner.

Since the interferometer is an optical instrument and epitaxial in configuration, it holds great promise as a minimally-invasive instrument for precise measurements of living tissue. The interferometer may be partly or wholly implemented in fiber form, and thus it could be passed through an endoscope or laparoscope to probe deep inside a living organism.

5.1.2 Development of Interferometric Photothermal Spectroscopy (IPTS)

We have developed and demonstrated a new technique for estimating the effective absorption coefficient of a laser pulse in a tissue target, termed Interferometric Photothermal Spectroscopy (IPTS). IPTS is not intended to replace traditional spectroscopic techniques but rather to complement them and perform measurements of effective absorption coefficients that would be otherwise impossible. IPTS is significant new tool for spectoscopic measurements since it requires minimal disturbance of the tissue specimen and is epitaxial so that it may be employed *in vivo*. IPTS is one among many recently developed minimally-invasive optical diagnostic techniques such as Pulsed Photothermal Radiometry (PPTR), Optical Coherence Tomography (OCT), and Fluorescence Diagnostics.

Experiments conducted with a Q-sw Er:YSGG laser on pure water samples confirmed that IPTS is an accurate and reliable technique under the proper experimental conditions. Subsequently, IPTS was used to measure the effective absorption coefficient of ArF excimer laser radiation of corneal stroma since previous efforts to measure this parameter were thwarted by the difficulty in producing a proper sample. The ability of IPTS to overcome these problems and measure an effective absorption coefficient with minimal disturbance to the sample was demonstrated with these experiments. The effective absorption coefficient was found to be $19{,}000 \pm 4{,}000\ cm^{-1}$ *in vitro*. We believe this measurement to be the most accurate one to date. This measurement is important since it indicates how the laser energy is localized during ArF excimer laser ablation of corneal tissue which occurs during the clinical photorefractive keratectomy (PRK) procedure and thus influences how the corneal ablation process is modeled.

The thermal modeling and interferometer detailed in this thesis represent a new way to measure the thermalization of a laser pulse energy. Surface displacement measurements of cornea exposed to 193 nm laser radiation reported here suggest that many dozens of nanoseconds are required to completely thermalize the laser pulse energy. This may be due the time required to transfer thermal energy from the corneal collagen to the free water or photochemistry in the collagen.

5.1.3 Progress in Interphase Heat and Mass Transfer and Implications for Tissue Ablation

In this thesis we have presented experimental data and a theoretical model indicating that pulsed laser driven interphase heat and mass transfer is an important phenomena for certain laser-tissue interactions. Previous workers have all but ignored to the role played by interphase heat and mass transfer during tissue ablation, mainly due to a lack of experimental data. The novel experimental data presented here was made possible by the extreme sensitivity of the interferometer. For the first time, the mass vaporized into a Knudsen layer was quantifiable in a time-resolved manner. Interferometric surface measurement opens up a whole new approach for exploration of high rate interphase mass transfer.

The results suggest that at high laser irradiances, the heat and mass flux occurring at the surface of a pure water target can approach and even exceed the upper limits predicted by a simple kinetic theory model. We offered several possible explanations for this discrepancy. The model assumed a monatomic ideal gas behavior and did not account for the vibrational and rotational states available to water molecules. Furthermore, surface contaminants on the water sample may have somehow led to unusual molecular dynamics. Finally, the molecules in the system may not adhere to the assumed Maxwell-Boltzmann velocity distribution. In any case, pulsed laser driven interphase heat and mass transfer remains poorly explained.

We have postulated that when the laser pulse is thermally confined but not mechanically confined and the effective absorption depth is very shallow (<~3 μm) the ablation threshold and ablation dynamics may be controlled by high rate interphase heat and mass transfer at the tissue surface. Thus we have highlighted the fact that pulsed laser driven interphase heat and mass

transfer must be considered when modeling photothermal laser ablation. During ArF excimer laser ablation of cornea, high rate interphase heat and mass transfer may itself be the ablation mechanism. This conclusion is not surprising since previous workers have shown that the dynamics of ArF excimer laser corneal ablation is consistent with rapid surface vaporization [94, 95].

5.2 Future Research Directions

The research findings detailed in this thesis suggest several new important topics for future investigations. These may be organized according to the categories of instrumentation, minimally-invasive diagnostics, interphase heat and mass transfer, and laser ablation modeling.

5.2.1 Instrumentation

Photothermal laser-tissue interactions are often fast processes (<1 ms) that usually occur on small scales (<100 μm) and consequently it has often been difficult to obtain precise time-resolved experimental data. There is a strong need for advanced instrumentation that can provide this information. Interferometry has only recently been applied to study such photothermal phenomena and we contend that further improvements in the instrument can be made to increase it's sensitivity and bandwidth. There is no technical impediment to a single nanosecond rise time, sub-nanometer resolution interferometer.

In this thesis we point out that an interferometer could in theory exploit confocal microscope technology and monitor the displacement of an optical scatterer below the tissue surface. This development would be particularly significant since one of the greatest disadvantages to surface interferometry is that it is difficult to infer the entire sub-surface displacement field of the tissue based solely on the displacement of a surface point. Measurements of the subsurface displacement field would permit the development of more sophisticated models for photothermal laser-tissue interactions and permit more precise measurements of the effective absorption coefficient using IPTS. These measurements could

open up the possibility of three dimensional photothermal displacement imaging of the tissue specimen.

Spatial arrays of photodiodes could be employed in a multibeam interferometer to simultaneously track the motion of several points on the tissue surface. This information could be used to create a surface displacement map with nanometer resolution and nanosecond rise time. Such measurements would make it much easier to monitor laser-tissue interactions which do not conform to the one dimensional irradiation geometry assumed throughout this thesis.

Finally, important data could be obtained through the simultaneous use of two or more time-resolved measurement techniques. Interferometry and stress transducer measurements complement each other well (Table 2.1) and the combination of the two may be capable of providing otherwise unavailable information. Precise measurements of the time delay between laser irradiation and ablation onset near threshold radiant exposures could be of critical importance to laser ablation modeling. A sensitive stress transducer may be capable of detecting the recoil momentum associated with high rate interphase mass transfer.

5.2.2 Minimally-Invasive Diagnostics

The IPTS technique developed in this thesis has thus far only been applied to make a single *in vitro* laser absorption measurement. IPTS has the potential to serve as a minimally-invasive clinical diagnostic and this potential should be explored in future work. Future experiments should be conducted *in vivo* to illustrate the full potential of IPTS with an eye towards developing new IPTS applications. IPTS measurements of corneal absorption at 193 nm should be conducted *in vivo* on an animal model to see if the *in vitro* results described in this thesis are indeed valid in a clinical setting.

Potential diagnostic applications for IPTS would most probably be based on the determination of the concentration of a chemical species from the effective absorption coefficient. With the proper pump laser pulse, perhaps obtained from a dye laser, a preliminary research effort to estimate blood oxygenation could be conducted. Measuring the concentration

of an exogenous drug or photosensitizer might also ultimately become an important IPTS application. IPTS could serve as an optical biopsy technique by detecting an exogenous chemical marker or an endogenous chemical species associated with cancer cells.

Aside from the effective absorption depth of radiation, the instrumentation and thermal models developed in this thesis could also be used to estimate the thermophysical properties of a target tissue specimen. In some cases, the thermal properties of the tissue may be a good indicator of tissue pathology. This possibility should be explored and if possible exploited in future work.

To fully realize the potential for IPTS as a minimally-invasive diagnostic, future interferometers would need to be built from fiber optic components to enable it to pass through an endoscope or laparoscope. This does not appear to be a serious technological hurdle given current optical fiber technology.

5.2.3 Detailed Study of Interphase Heat and Mass Transfer

The results presented here concerning pulsed laser driven interphase heat and mass transfer are intriguing and merit further investigation. To our knowledge, no other researchers have employed interferometry for the study of interphase heat and mass transfer. From the work presented here it appears that interferometry is an attractive technique for time-resolved measurements of high flux rates over short timescales. Future efforts might be made to optimize the instrumentation for the detection of interphase heat and mass transfer. Optical reflectance measurements of the sample surface could provide additional time-resolved thermodynamic information which would greatly improve our understanding of this process.

At this time it is unclear why under certain conditions the interphase heat and mass transfer reported here appears to exceed the upper limits predicted by kinetic theory. This discrepancy is disturbing and demands a complete inquiry. The simple kinetic model presented here may not capture the full physics of the phenomenon and so more sophisticated models are desired. Computer simulations of the molecular dynamics should be conducted as they may

provide insight into the sort of heat and mass fluxes encountered here.

5.2.4 Development of New Laser Ablation Models

Novel predictive models of laser-tissue ablation should be derived in order to develop new clinical laser ablation applications as well as to optimize existing applications. The results of this thesis suggest that interphase heat and mass transfer is an important phenomenon during pulsed laser-tissue ablation when the effective absorption depth is relatively shallow. This phenomenon must be fully explored with the goal of developing predictive models for laser-tissue ablation. Predictive models are preferred to empirical ones as they can be employed to suggest optimal laser ablation characteristics for laser parameters that are currently unavailable. If the modeling suggests that a desirable therapeutic outcome may result from tissue ablation with a set of currently unavailable laser parameters, research efforts can be focused on building such a laser system.

The thermalization of laser pulse energy is during ArF excimer laser ablation of cornea should be clarified in future studies. Measurements from this thesis strongly suggest that ArF excimer laser pulse energy requires on the order of 20 ns or more to fully thermalize. This result may be explainable by the time required to transfer energy from the collagen to the free water or by photochemical activity of the cornea. Further experiments should be done to determine which interpretation is correct. Results obtained at 193 nm should be compared with those obtained at 213 nm where similar ablation characteristics have been noted.

Appendix A:
One Dimensional Thermal Expansion

In this appendix, we shall derive equations governing one dimensional thermal expansion for isotropic linear elastic materials. Note that although the elastic properties (E, K_b, etc.) are treated as constants, the density of the material is permitted to be a non-linear function of temperature (i.e. the thermal expansion coefficient α_T may vary with temperature). The linear elastic treatment presented in this appendix can serve as an approximation to the true non-linear behavior of biological tissue. Should the approximations made in this derivaation be inadequate, the thermoelastic behavior of the tissue may be treated numerically.

In our orthogonal coordinate system, a thermally expanding body occupies the half space with $z>0$. The net thermal expansion of this body is given by Δz:

$$\Delta z = \int_0^\infty \varepsilon_{zz} dz \tag{A.1}$$

where ε_{zz} is the strain in the z direction (negative for compressive strain). In general, ε_{zz} may be a function of time t consequently Δz may be a function of time. The temperature field is assumed to be only a function of z and t consequently symmetry demands that there can be no displacements in the x or y direction:

$$u_x = 0 \quad u_y = 0 \quad u_z = u_z(z) \tag{A.2}$$

The strain tensor, ε_{ij} may be expressed as [92]:

$$\varepsilon_{ij} = \frac{1}{2}\left(u_{i,j} + u_{j,i}\right) \tag{A. 3}$$

which in our case reduces to:

$$\varepsilon_{zz} = \frac{\partial u_z}{\partial z} \tag{A.4}$$

with all other ε_{ij}=0 (no shear strains).

In a linear elastic isotropic body, the relationship between stress and strain may be written as:

$$\varepsilon_{ij} = \frac{1+\nu}{E}\sigma_{ij} - \frac{\nu}{E}\sigma_{kk}\delta_{ij} + \frac{\Delta V}{3V}\delta_{ij} \tag{A.5}$$

where σ_{ij} is the stress tensor (negative for compression), δ_{ij} is Kronecker's delta, ν is Poisson's ratio, E is the elastic modulus. This expression differs from that presented in [92] in that $\Delta V/3V$ is used in place of $\alpha_T \Delta T$. $\Delta V/V$ is the fractional volume change (pure dilatation) that would result from a temperature change in the absence of any stress. Note that for a material with a constant thermal expansion coefficient α_T, $\Delta V/3V=\alpha_T \Delta T$ where ΔT is the local temperature rise.

Due to symmetry, the normal strain in the x direction, σ_{xx}, is equal to the normal strain in the y direction, σ_{yy}, and consequently we denote both of them by $\sigma_\perp$. Since there are no shear strains there can be no shear stresses. Eq. (A.5) reduces to:

$$\left\{ \begin{array}{c} \varepsilon_{zz} = \dfrac{\sigma_{zz}}{E} - \dfrac{2\nu\sigma_\perp}{E} + \dfrac{\Delta V}{3V} \\ 0 = \dfrac{(1-\nu)\sigma_\perp}{E} - \dfrac{\nu\sigma_{zz}}{E} + \dfrac{\Delta V}{3V} \end{array} \right\} \tag{A.6}$$

Upon algebraic elimination of $\sigma_\perp$ one obtains:

$$\varepsilon_{zz} = \left(\frac{1+\nu}{1-\nu}\right)\frac{\Delta V}{3V} + \left(\frac{1+\nu}{1-\nu}\right)\frac{\sigma_{zz}}{3K_b} \tag{A.7}$$

where K_b is the bulk modulus and is given by [92]:

$$K_b = \frac{E}{3(1-2\nu)} \tag{A.8}$$

Eq. (A.7) expresses the strain in the z direction as a function of the stress in the z direction and the local free thermal expansion. This general expression can be used in Eq. (A.1) to find the net thermal expansion in the z direction.

One can express $\Delta V/V$ as a function of temperature providing the temperature dependence of density is well characterized. In Figure A.1 an isotropic cube with edge length L, is depicted before and after a dilatation resulting from a uniform temperature change. The net volume change ΔV is given by:

$$\Delta V = \left(L + \Delta L\right)^3 - L^3 \tag{A.9}$$

where ΔL is the change in length of the cube edge. If ΔL is small compared to L the higher order terms can be neglected and the fractional volume change may be written as:

$$\frac{\Delta V}{V} = 3\,\frac{\Delta L}{L} \tag{A.10}$$

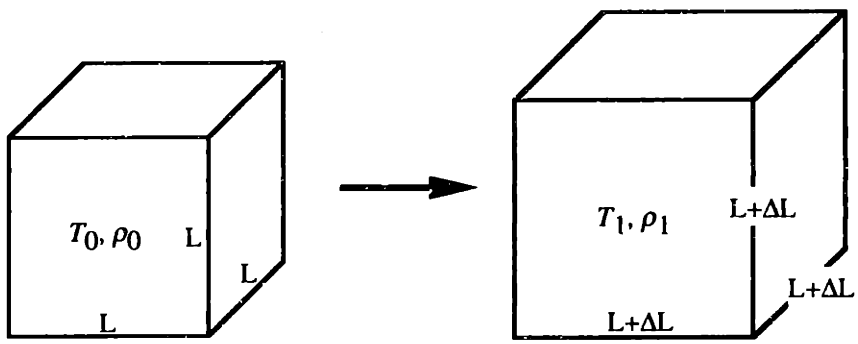

Figure A.1: Illustration of a pure dilatation due to a temperature change in an isotropic body

The mass of the cube does not change with the dilatation and is given by its density times its volume. Consequently:

$$\rho_0 L^3 = \rho_1\left(L + \Delta L\right)^3 \approx \rho_1\left(L^3 + 3L^2\Delta L\right) \tag{A.11}$$

where $\approx$ is employed to indicate that higher order terms have been neglected. Eq. (A.11) can be manipulated to yield:

$$3\frac{\Delta L}{L} = \left(\frac{\rho_0}{\rho_1} - 1\right) \tag{A.12}$$

In the special case that all of the stresses in the z direction are permitted to relax and σ_{zz} is zero everywhere, Eqs. (A.10) and (A.12) may be substituted into Eq. (A.7) to yield the strain in the z direction:

$$\varepsilon_{zz} = \frac{1}{3}\left(\frac{1+\nu}{1-\nu}\right)\left(\frac{\rho_0}{\rho\left[T(z,t)\right]} - 1\right) \tag{A.13}$$

This is the general expression for the strain encountered during IPTS and it may be used as the integrand in Eq. (A.1) for any linear elastic isotropic material. Samples of pure water are assumed to be nearly incompressible so that ν is taken to be 0.5 and Eq. (A.1) may be written as:

$$\Delta z(t) = \int_0^{\infty} \left(\frac{\rho_0}{\rho\left[T(z,t)\right]} - 1\right) dz \tag{A.14}$$

This is identical to Eq. (3.3) when the coordinate z is replaced with z_0. This is the same equation employed in Chapter 3 for IPTS measurements of corneal tissue since cornea has been measured to be nearly incompressible (ν~0.48) as it is about 80% water [6].

As discussed in Chapter 4, surface vaporization results in a recoil stress σ_{recoil} in the z direction. If the sample is pure water with ν approximately equal to 0.5 the strain in the z direction described by Eq. (A.7) may be written as:

$$\varepsilon_{zz} = \left(\frac{\rho_0}{\rho\left[T(z,t)\right]} - 1\right) + \frac{\sigma_{recoil}}{K_b} \tag{A.15}$$

σ_{recoil}/K_b may be termed ε_{recoil} as in Eq. (4.11). This expression may be substituted into Eq. (A.1) to yield:

$$\Delta z(t) = \int_0^{\infty} \left(\frac{\rho_0}{\rho\left[T(z,t)\right]} - 1\right) dz + \int_0^{\infty} \varepsilon_{recoil} dz \tag{A.16}$$

The first integral is the same as the first term on the right hand side of Eq. (4.10) while the second integral is the same as the third term on the right hand side of Eq. (4.10).

References

[1] R. K. Al-Dhahir, P. E. Dyer, and Z. Zhu, "Photoacoustic Studies and Selective Ablation of Vascular Tissue Using a Pulsed Dye Laser," *Applied Physics B: Photophysics and Laser Chemistry*, vol. 51, pp. 81-85, 1990.

[2] D. Albagli, *Fundamental Mechanisms of Pulsed Laser Ablation of Biological Tissue*. Cambridge, MA: Massachusetts Institute of Technology, 1994.

[3] D. Albagli, B. J. Banish, M. L. Dark, G. S. Janes, C. von Rosenberg, L. T. Perelman, I. Itzkan, and M. S. Feld, "Interferometric Surface Monitoring of Biological Tissue to Study Inertially Confined Ablation," *Lasers in Surgery and Medicine*, vol. 14, pp. 374-385, 1994.

[4] D. Albagli, M. L. Dark, L. T. Perelman, C. von Rosenberg, I. Itzkan, and M. S. Feld, "Photomechanical basis of laser ablation of biological tissue," *Optics Letters*, vol. 19, pp. 1684-1686, 1994.

[5] R. R. Anderson and J. A. Parrish, "Microvasculature Can Be Selectively Damaged Using Dye Lasers: A Basic Theory and Experimental Evidence in Human Skin," *Lasers in Surgery and Medicine*, vol. 1, pp. 263-276, 1981.

[6] J. L. Battaglioli and R. D. Kamm, "Measurements of the Compressive Properties of Scleral Tissue," *Investigative Ophthalmology and Visual Science*, vol. 25, pp. 59-65, 1984.

[7] J. V. Beck, B. Blackwell, and C. R. St. Clair, Jr., *Inverse Heat Conduction*. New York: John Wiley & Sons, 1985.

[8] S. E. Bialkowski, *Photothermal Spectroscopy Methods for Chemical Analysis*, vol. 134, 1st ed. New York: John Wiley & Sons, 1996.

[9] M. Born and E. Wolf, *Priciples of Optics*, 6th ed. New York: Oxford University Press, 1980.

[10] W.-F. Cheong, S. A. Prahl, and A. J. Welch, "A Review of the Optical Properties of Biological Tissue," *IEEE Journal of Quantum Electronics*, vol. 26, pp. 2166-2185, 1990.

[11] F. W. Cross, R. K. Al-Dhahir, and P. E. Dyer, "Ablative and acoustic response of pulsed UV laser-irradiated vascular tissue in a liquid environment," *Journal of Applied Physics*, vol. 64, pp. 2194-2201, 1988.

[12] J. P. Cummings and J. T. Walsh, Jr., "Erbium Laser Ablation: The effect of Dynamic Optical Properties," *Applied Physics Letters*, vol. 62, pp. 1988-1990, 1993.

[13] J. P. Cummings and J. T. Walsh, Jr., "Tissue tearing caused by pulsed laser-induced ablation pressure," *Applied Optics*, vol. 32, pp. 494-503, 1993.

[14] F. W. Dabby and U.-C. Paek, "High-Intensity Laser-Induced Vaporization and explosion of Solid Material," *IEEE Journal of Quantum Electronics*, vol. QE-8, pp. 106-111, 1972.

[15] A. G. Doukas and T. J. Flotte, "Physical characteristics and biological effects of laser-induced stress waves," *Ultrasound in Medicine and Biology*, vol. 22, pp. 151-164, 1996.

[16] Dow Chemical Corporation, "Typical properties for saran wrap 19," Dow Chemical Company, Midland, MI 190-00456-496RJD, 1997.

[17] H. D. Downing and D. Williams, "Optical Constants of Water in the Infrared," *Journal of Geophysical Research*, vol. 80, pp. 1656-1661, 1975.

[18] P. E. Dyer and R. K. Al-Dhahir, "Transient photoacoustic studies of laser tissue ablation," Proc. of the SPIE Vol. 1427 Laser-Tissue Interaction II, 1990.

[19] M. N. Ediger, G. H. Pettit, and D. W. Hahn, "Enhanced ArF Laser Absorption in a Collagen Target Under Ablative Conditions," *Lasers in Surgery and Medicine*, vol. 15, pp. 107-111, 1994.

[20] M. N. Ediger, G. H. Pettit, R. P. Weiblinger, and C. H. Chen, "Transmission of Corneal Collagen During ArF Excimer Laser Ablation," *Lasers in Surgery and Medicine*, vol. 13, pp. 204-210, 1993.

[21] A. F. Emery, P. Kramar, A. W. Guy, and J. C. Lin, "Microwave induced Temperature Rises in Rabbit Eyes in Cataract Research," *ASME Journal of Heat Transfer*, vol. 97, pp. 123-128, 1975.

[22] A. M. R. Fisher, A. L. Murphree, and C. J. Gomer, "Clinical and Preclinical Photodynamic Therapy," *Lasers in Surgery and Medicine*, vol. 17, pp. 2-31, 1995.

[23] M. Forrer, M. Frenz, V. Romano, and H. P. Weber, "Channel propagation in water and gelatin by a free-running erbium laser," *Journal of Applied Physics*, vol. 74, pp. 720-727, 1993.

[24] G. R. Fowles, *Introduction to Modern Optics*, 2nd ed. New York: Dover, 1975.

[25] W. R. Gambill and J. H. Lienhard, "An Upper Bound for the Critical Boiling Heat Flux," *ASME Journal of Heat Transfer*, vol. 111, pp. 815-818, 1989.

[26] B. J. Garrison and R. Srinivasan, "Laser ablation of organic polymers: Microscopic models for photochemical and thermal processes," *Journal of Applied Physics*, vol. 57, pp. 2909-2914, 1985.

[27] D. W. Hahn, M. N. Ediger, and G. H. Pettit, "Dynamics of Ablation Plume Particles Generated During Excimer Laser Corneal Ablation," *Lasers in Surgery and Medicine*,

vol. 16, pp. 384-389, 1995.

[28] P. Hariharan, *Basics of Interferometry*. Boston: Academic Press, 1992.

[29] H. A. Haus, *Waves and Fields in Optoelectronics*, 1st ed. Englewood Cliffs, NJ: Prentice-Hall, 1984.

[30] C. K. Hsieh, "Heat Transfer 1986," 8th International Heat Transfer Conference, San Francisco, 1986.

[31] D. Huang, E. A. Swanson, C. P. Lin, J. S. Schuman, W. G. Stinson, W. Chang, M. R. Hee, T. J. Flotte, K. Gregory, C. A. Puliafito, and J. G. Fujimoto, "Optical Coherence Tomography," *Science*, vol. 254, pp. 1178-1181, 1991.

[32] I. Itzkan, D. Albagli, B. J. Banish, M. L. Dark, C. von Rosenberg, L. T. Perelman, G. S. Janes, and M. S. Feld, "Pressure generation during inertially confined laser ablation of biological tissue," in *Laser Ablation: Mechanisms and Applications II*, vol. 288, J. C. Miller and D. B. Geohagen, Eds. New York: AIP, 1994, pp. 491-506.

[33] I. Itzkan, D. Albagli, M. L. Dark, L. T. Perelman, C. von Rosenberg, and M. S. Feld, "The thermoelastic basis of short pulsed laser ablation of biological tissue," *Proceedings of the National Academy of Sciences*, vol. 92, pp. 1960-1964, 1995.

[34] J. A. Izatt, D. Albagli, I. Itzkan, and M. S. Feld, "Pulsed laser ablation of calcified tissue: physical mechanisms and fundamental parameters," Proc. of the SPIE Vol. 1202 Laser-Tissue Interaction, 1990.

[35] S. L. Jacques, J. S. Nelson, W. H. Wright, and T. E. Milner, "Pulsed photothermal radiometry of port-wine-stain lesions," *Applied Optics*, vol. 32, pp. 2439-2445, 1993.

[36] A. A. Karabutov, N. B. Podymova, and V. S. Letokhov, "Time-resolved laser optoacoustic tomography of inhomogeneous media," *Applied Physics B: Photophysics and Laser Chemistry*, vol. 63, pp. 545-563, 1996.

[37] R. Kelly and A. Miotello, "Comments on explosive mechanisms of laser sputtering," *Applied Surface Science*, vol. 96-98, pp. 205-215, 1996.

[38] Kimble Glass Corporation, "Properties of Kimble Glasses," Kimble Glass Company 1997.

[39] G. S. Kino, *Acoustic Waves: Devices, Imaging, and Analog Signal Processing*. Englewood Cliffs, NJ: Prentice Hall, 1987.

[40] W. T. Knoefel, N. Kollias, D. W. Rattner, and A. L. Warshaw, "Reflectance spectroscopy of pancreatic microcirculation," *Journal of Applied Physiology*, pp. 116-123, 1996.

[41] D. A. Labuntsoz and A. P. Kryukov, "Analysis of intensive evaporation and condensation," *International Journal of Heat and Mass Transfer*, vol. 22, pp. 989-1002, 1979.

[42] F. H. Long, R. R. Anderson, and T. F. Deutsch, "Pulsed photothermal radiometry for depth profiling of layered media," *Applied Physics Letters*, vol. 51, pp. 2076-2078,

1987.

[43] F. H. Long, N. S. Nishioka, and T. F. Deutsch, "Measurement of the Optical and Thermal Properties of Biliary Calculi Using Pulsed Photothermal Radiometry," *Lasers in Surgery and Medicine*, vol. 7, pp. 461-466, 1987.

[44] D. R. Marble, D. H. Burns, and P. W. Cheung, "Diffusion-based model of pulse oximetry: *in vitro* and *in vivo* comparisons," *Applied Optics*, vol. 33, pp. 1279, 1994.

[45] G. T. Martin and H. F. Bowman, "Model and solution for the thermal response of blood perfused tissue during laser hyperthermia," Proc. of the SPIE Vol. 1202 Laser-Tissue Interaction, 1990.

[46] D. M. Maurice, "The Cornea and Sclera," in *The Eye*, vol. 1b, H. Davson, Ed., 3rd ed. New York: Academic Press, 1984, pp. 1-158.

[47] A. Mills, F, *Heat and Mass Transfer*, 1st ed. Boston: Irwin, 1995.

[48] A. F. Mills, *Heat Transfer*, 1st ed. Boston: Irwin, 1992.

[49] A. F. Mills and R. A. Seban, "The condensation coefficient of water," *International Journal of Heat and Mass Transfer*, vol. 10, pp. 1815-1827, 1967.

[50] T. A. Milner, D. J. Smithies, D. M. Goodman, A. Lau, and J. S. Nelson, "Depth determination of chromophore in human skin by pulsed photothermal radiometry," *Applied Optics*, vol. 35, pp. 3379-3385, 1996.

[51] A. Miotello and R. Kelly, "Critical assessment of thermal models for laser sputtering at high fluences," *Applied Physics Letters*, vol. 67, pp. 3535-3537, 1995.

[52] M. Munidasa and A. Mandelis, "Photothermal imaging and detection," in *Progress in Photothermal and Photoacoustic Science and Technology*, vol. 1, *Principles and Perspectives of Photothermal and Photoacoustic Phenomena*, A. Mandelis, Ed. New York: Elsvier, 1992, pp. 299-367.

[53] N. S. Nishioka, "Laser-induced fluorescence spectroscopy," *Gastrointestinal Endoscopy Clinics of North America*, vol. 4, pp. 313-326, 1994.

[54] M. A. Olmstead, N. M. Amer, and S. Kohn, "Photothermal Displacement Spectroscopy: An Optical probe for Solids and Surfaces," *Applied Physics A: Solids and Surfaces*, vol. A32, pp. 141-154, 1983.

[55] A. A. Oraevsky, R. O. Esenaliev, and V. S. Letokhov, *Pulsed Laser Ablation of Biological Tissue: Review of the Mechanisms*. New York: Springer Verlag, 1991.

[56] A. A. Oraevsky, S. L. Jacques, and F. K. Tittel, "Mechanism of laser ablation for aqueous media irradiated under confined stress conditions," *Journal of Applied Physics*, vol. 78, pp. 1281-1289, 1995.

[57] G. Paltauf and H. Schmidt-Kloiber, "Model Study to Investigate the Contribution of Spallation to Pulsed Laser Ablation of Tissue," *Lasers in Surgery and Medicine*, vol. 16, pp. 277-287, 1995.

[58] G. Paltauf and H. Schmidt-Kloiber, "Modeling and experimental observation of photomechanical effects in tissue-like media," Proc. of the SPIE Vol. 2391 Laser Tissue Interaction VI, 1995.

[59] G. Paltauf and H. Schmidt-Kloiber, "Microcavity dynamics during laser-induced spallation of liquids and gels," *Applied Physics A: Solids and Surfaces*, vol. 62, pp. 303-311, 1996.

[60] A. Patera, personal communication, 9/3/96.

[61] B. Payne, N. S. Nishioka, B. B. Mikic, and V. Venugopalan, "Comparison of Pulsed CO_2 laser ablation at 10.6 μm and 9.5 μm," *Submitted to Lasers in Surgery and Medicine.*

[62] G. H. Pettit and M. N. Ediger, "Corneal-tissue absorption coefficients for 193- and 213-nm ultraviolet radiation," *Applied Optics*, vol. 35, pp. 3386-3391, 1996.

[63] G. H. Pettit, M. N. Ediger, and R. P. Weiblinger, "Excimer laser corneal ablation: absence of a significant 'incubation' effect," *Lasers in Surgery and Medicine*, vol. 11, pp. 411-418, 1991.

[64] G. H. Pettit, M. N. Ediger, and R. P. Weiblinger, "Dynamic optical properties of collagen-based tissue during ArF excimer laser ablation," *Applied Optics*, vol. 32, pp. 488-492, 1993.

[65] G. H. Pettit and R. Sauerbrey, "Fluence-dependent transmission of polyimide at 248 nm under laser ablation conditions," *Applied Physics Letters*, vol. 58, pp. 793-795, 1991.

[66] G. H. Pettit and R. Sauerbrey, "Pulsed Ultraviolet Laser Ablation," *Applied Physics A: Solids and Surfaces*, vol. 56, pp. 51-63, 1993.

[67] W. H. Press, B. P. Flannery, S. A. Teukolsky, and W. T. Vetterling, *Numerical Recipes in C*. New York: Cambridge University Press, 1988.

[68] C. A. Puliafito, R. F. Steinert, T. F. Deutsch, F. Hillenkamp, E. J. Dehm, and C. M. Adler, "Excimer Laser Ablation of the Cornea and Lens," *Ophthalmology*, vol. 92, pp. 741-748, 1985.

[69] I. J. Rampil, L. Litt, and A. Mayevsky, "Correlated, simultaneous, multiple wavelength optical monitoring in vivo of localized cerebrocortical NADH and brain microvessel hemoglobin oxygen saturation," *Journal of Clinical Monitoring*, vol. 8, pp. 216-225, 1992.

[70] F. Reif, *Fundamentals of statistical and thermal physics*, 1st ed. New York: McGraw-Hill, 1965.

[71] Q. Ren, R. P. Gailitis, K. P. Thompson, and J. T. Lin, "Ablation of the Cornea and Synthetic Polymers Using a UV (213 nm) Solid-State Laser," *IEEE Journal of Quantum Electronics*, vol. 26, pp. 2284-2288, 1990.

[72] Q. Ren, R. H. Keates, R. A. Hill, and M. W. Berns, "Laser refractive surgery: a

review and current status," *Optical Engineering*, vol. 34, pp. 642-658, 1995.

[73] Q. Ren, G. Simon, J.-M. Legeais, J.-M. Parel, W. Culbertson, J. Shen, Y. Takesue, and M. Savoldelli, "Ultraviolet Solid-state Laser (213-nm) Photorefractive Keratectomy," *Ophthalmology*, vol. 101, pp. 883-889, 1994.

[74] Q. Ren, G. Simon, and J.-M. Parel, "Ultraviolet Solid-state Laser (213-nm) Photorefractive Keratectomy," *Ophthalmology*, vol. 100, pp. 1828-1834, 1993.

[75] K. Rink, G. Delacretaz, and R. P. Salathe, "Fragmentation process induced by microsecond laser pulses during lithotripsy," *Applied Physics Letters*, vol. 61, pp. 258-260, 1992.

[76] K. Rink, G. Delacretaz, and R. P. Salathe, "Fragmentation process induced by nanosecond laser pulses," *Applied Physics Letters*, vol. 61, pp. 2644-2646, 1992.

[77] A. Rosencwaig, *Photoacoustics and Photoacoustic Spectroscopy*, vol. 57. New York: John Wiley & Sons, 1980.

[78] G. Rousset and L. Bertrand, "A pulsed thermoelastic analysis of photothermal surface displacements in layered materials," *Journal of Applied Physics*, vol. 57, pp. 4396-4405, 1985.

[79] J. Schaffer, M. L. Dark, I. Itzkan, D. Albagli, L. T. Perelman, C. von Rosenberg, and M. S. Feld, "Mechanisms of Meniscal Tissue Ablation by Short Pulse Laser Irradiation," *Clinical Orthopaedics and Related Research*, vol. 310, pp. 30-36, 1995.

[80] R. W. Schrage, *A Theoretical Study of Interphase Mass Transfer*, 1st ed. New York: Columbia University Press, 1953.

[81] J. J. Schuitmaker, P. Baas, H. L. L. M. van Leengoed, F. W. van der Meulen, W. M. Star, and N. van Zandwijk, "Photodynamic therapy: a promising new modality for the treatment of cancer," *Journal of Photochemistry and Photobiology B:Biology*, vol. 34, pp. 3-12, 1996.

[82] J. A. Scott, "A finite element model of heat transport in the human eye," *Physics in Medicine and Biology*, vol. 33, pp. 227-241, 1988.

[83] M. W. Sigrist, "Laser generation of acoustic waves in liquids and gases," *Journal of Applied Physics*, vol. 60, pp. R83-R121, 1986.

[84] D. Singleton, "Applications of photoacoustic and photothermal techniques in studies of laser-tissue interactions and biomedical analysis," in *Progress in Photothermal and Photoacoustic Science and Technology*, vol. 1, *Principles and Perspectives of Photothermal and Photoacoustic Phenomena*, A. Mandelis, Ed. New York: Elsevier, 1992, pp. 542.

[85] D. L. Singleton, G. Paraskevopoulos, G. S. Jolly, R. S. Irwin, and D. J. McKenney, "Excimer lasers in cardiovascular surgery: Ablation products and photo-acoustic spectrum of arterial wall," *Applied Physics Letters*, vol. 48, pp. 878-890, 1986.

[86] E. M. Sparrow and R. D. Cess, *Radiation Heat Transfer*, 1st ed. Belmont, CA:

Brooks/Cole, 1966.

[87] R. Srinivasan and B. Braren, "Ultraviolet Laser Ablation of Organic Polymers," *Chemical Review*, vol. 89, pp. 1303-1316, 1989.

[88] R. Srinivasan, P. E. Dyer, and B. Braren, "Far-Ultraviolet Laser Ablation of the Cornea: Photoacoustic Studies," *Lasers in Surgery and Medicine*, vol. 6, pp. 514-519, 1987.

[89] P. T. Staveteig and J. T. Walsh, Jr., "Dynamic 193-nm optical properties of water," *Applied Optics*, vol. 35, pp. 3392-3403, 1996.

[90] A. C. Tam and B. Sullivan, "Remote sensing applications of pulsed photothermal radiometry," *Applied Physics Letters*, vol. 43, pp. 333-335, 1983.

[91] M. Terzic and M. W. Sigrist, "Pulsed photoacoustic measurements of large optical absorption coefficients," *Journal of Applied Physics*, vol. 67, pp. 3593-3596, 1990.

[92] S. P. Timoshenko and J. N. Goodier, *Theory of Elasticity*, 3rd ed. New York: McGraw-Hill, 1970.

[93] J. H. Torres, M. Motamedi, J. A. Pearce, and A. J. Welch, "Experimental evaluation of mathematical models for predicting the thermal response of tissue to laser irradiation," *Applied Optics*, vol. 32, pp. 597-606, 1993.

[94] V. Venugopalan, *The Thermodynamic Response of Polymers and Biological Tissue to Pulsed Laser Irradiation.* Cambridge, MA: Massachusetts Institute of Technology, 1994.

[95] V. Venugopalan, N. S. Nishioka, and B. B. Mikic, "The Thermodynamic Response of Soft Biological Tissue to Pulsed Ultraviolet Laser Irradiation," *Biophysical Journal*, vol. 69, pp. 1259-1271, 1995.

[96] V. Venugopalan, N. S. Nishioka, and B. B. Mikic, "Thermodynamic Response of Soft Biological Tissues to Pulsed Infrared-Laser Irradiation," *Biophysical Journal*, vol. 70, pp. 2981-2993, 1996.

[97] W. G. Vincenti and C. H. Kruger, Jr., *Introduction to Physical Gas Dynamics*, 1 ed. New York: John Wiley and Sons, 1965.

[98] I. A. Vitkin, B. C. Wilson, and R. R. Anderson, "Pulsed Photothermal Radiometry Studies in Tissue Optics," in *Optical-Thermal Response of Laser-Irradiated Tissue, Lasers, Photonics, and Electro-Optics*, A. J. Welch and M. J. C. van Gemert, Eds. New York: Plenum Press, 1995, pp. 535-560.

[99] K. L. Vodopyanov, "Saturation studies of H_2O and HDO near 3400 cm^{-1} using intense picosecond laser pulses," *Journal of Chemical Physics*, vol. 94, pp. 5389-5393, 1991.

[100] A. Vogel, S. Busch, Jungnickel, and R. Birngruber, "Mechanisms of Intraocular Photodisruption with Picosecond and Nanosecond Laser Pulses," *Lasers in Surgery and Medicine*, vol. 15, pp. 32-43, 1994.

[101] J. T. Walsh, Jr. and J. P. Cummings, "Effect of the Dynamic Optical Properties of

Water on MidInfrared Laser Ablation," *Lasers in Surgery and Medicine*, vol. 15, pp. 295-305, 1994.

[102] J. T. Walsh, Jr. and T. F. Deutsch, "Pulsed CO_2 Laser Tissue Ablation: Measurement of the Ablation Rate," *Lasers in Surgery and Medicine*, vol. 8, pp. 264-275, 1988.

[103] J. T. Walsh, Jr. and T. F. Deutsch, "Er:YAG Laser Ablation of Tissue: Effect of Pulse Duration and Tissue Type on Thermal Damage," *Lasers in Surgery and Medicine*, vol. 9, pp. 314-326, 1989.

[104] J. T. Walsh, Jr. and T. F. Deutsch, "Er:YAG Laser Ablation of Tissue: Measurement of Tissue Ablation Rates," *Lasers in Surgery and Medicine*, vol. 9, pp. 327-337, 1989.

[105] J. T. Walsh, Jr. and T. F. Deutsch, "Pulsed CO_2 Laser Ablation of Tissue: Effect of Tissue Mechanical Properties," *IEEE Transactions on Biomedical Engineering*, vol. 36, pp. 1195-1201, 1989.

[106] J. T. Walsh, Jr. and T. F. Deutsch, "Measurement of Er:YAG laser Ablation Plume Dynamics," *Applied Physics B: Photophysics and Laser Chemistry*, vol. 52, pp. 217-224, 1991.

[107] J. T. Walsh, Jr., T. J. Flotte, R. R. Anderson, and T. F. Deutsch, "Pulsed CO_2 Laser Tissue Ablation: Effect of Tissue Type and Pulse Duration on Thermal Damage," *Lasers in Surgery and Medicine*, vol. 8, pp. 108-118, 1988.

[108] S. Watanabe, T. J. Flotte, D. J. McAuliffe, and S. L. Jacques, "Putative Photoscousitc Damage in Skin Induced by Pulsed ArF Excimer Laser," *Journal of Investigative Dermatology*, vol. 90, pp. 761-766, 1988.

[109] R. C. Weast, *CRC Handbook of Chemistry and Physics*, 68 ed. Boca Raton: CRC Press, 1987.

[110] A. J. Welch, M. Motamedi, S. Rastegar, G. LeCarpentier, and D. Jansen, "Laser Thermal Ablation," *Photochemistry and Photobiology*, vol. 53, pp. 815-823, 1991.

[111] A. J. Welch and M. J. C. van Gemert, *Optical-Thermal Response of Laser-Irradiated Tissue*, 1st ed. New York: Plenum Press, 1995.

[112] B. C. Wilson, E. M. Sevick, M. S. Patterson, and B. Chance, "Time-Dependent Optical Spectoscopy and Imaging for Biomedical Applications," *Proceedings of the IEEE*, vol. 80, pp. 918-930, 1992.

[113] Y. Yashima, D. J. McAuliffe, S. L. Jacques, and T. J. Flotte, "Laser-Induced Photoacoustic Injury of Skin: Effect of Inertial Confinement," *Lasers in Surgery and Medicine*, vol. 11, pp. 62-68, 1991.

[114] A. Yodh and B. Chance, "Spectroscopy and imaging with diffusing light," *Physics Today*, vol. 48, pp. 34-40, 1995.